Design and Quantification of Highly Corrosion-Resistant Magnetorheological Finishing Powder

by

Luccas J. Giannechini

Submitted in partial Fulfillment of the

Requirements for the Degree

Master of Science

Supervised by

Professor Stephen D. Jacobs,

Professor John C. Lambropoulos

and

Mr. Kenneth L. Marshall

Materials Science Program

Arts, Sciences and Engineering

Edmund A. Hajim School of Engineering and Applied Sciences

University of Rochester

2015

Dedication

I dedicate this work to my family and my advisors, I could not have completed this work without their support and assistance. I would first like to dedicate this work to the memory of my mother, who was always there for me and always believed in me. Secondly, I would like to thank my father, who has always been supportive of my interests and confident that I could accomplish whatever I set my mind to. I also dedicate this work to the memory of Dr. Stephen Jacobs, who was a remarkable boss and advisor, and was a motivational and inspiring leader.

Biographical Sketch

Lucca Giannechini was born in Fairbanks, Alaska. He enrolled at the University of Rochester in 2008, and in 2013 graduated with a Bachelor of Science degree in Mechanical Engineering. He began his graduate studies at the University of Rochester in the Materials Science Program under the direction of Professor Stephen D. Jacobs. His Master's research focused on the development and quantification of a highly corrosion-resistant zirconia-coated magnetorheological finishing powder.

Acknowledgements

Many people aided me in the completion of this work and I would like to take a moment to show my gratitude for all of their assistance. I sincerely appreciate all of the help and guidance provided by my advisor, Professor Stephen Jacobs. His passion and dedication to research was both inspiring and highly motivational. I would also like to thank Mr. Kenneth Marshall, who helped guide me through the writing and editing of my thesis; I couldn't have done it without him. I owe thanks to Professor Paul Funkenbusch for the help he gave me in the design and analysis of the corrosion testing experiment, as his extensive knowledge of practical experimental design was invaluable for this work. I am also appreciative of Professor John Lambropoulos, who always made time to see me and answer my questions throughout this process.

I would like to show my gratitude toward Sivan Salzman, who was extremely helpful and generous with her time. She was always willing to take time out of her schedule to educate me on the finer points of the research project. I would also like to thank Henry Romanosfky, who showed me the ropes in the Magnetorheological Finishing Lab and always made time to help when I asked for his assistance. I am grateful for all of the ideas and support that Brittany Taylor provided throughout this process, especially concerning my X-ray photoelectron spectroscopy measurements and analysis. My appreciation to Brian McIntyre for imparting a fraction of his immense knowledge and expertise of

scanning electron microscopy to me. I would like to thank Chris Pratt for her advice and assistance with the Phillips MPD X-ray diffractometer. I owe appreciation to Alex Maltsev and Mike Kaplun of the LLE Optical Fabrication Laboratory for the aid they provided me in sample preparation and fabrication. I would like to extend my gratitude toward Nicholas Golini, who was invaluable in helping collect and analyze data for this research. My sincere gratitude to Jill Morris and Sarah Ansini for their administrative assistance and motivation throughout my time at the University of Rochester. Finally, I would like to thank my girlfriend, Sandra Golberg. I could not have accomplished this without her unwaivering encouragement and support.

Abstract

The purpose of this work is to increase the corrosion resistance of micron-sized zirconia coated iron powders, and to develop a reliable and precise method of quantifying a variety of the material's parameters. The powders that were tested are used as the base of the magnetorheological finishing slurries in the Magnetorehological Finishing (MRF) lab at the Laboratory for Laser Energetics. Development of the following methods enables quantitative comparisons between various batches of MRF powder, and serves as a metric for variations in performance. In this work, methods for the quantification of: corrosion time, mass fraction of the elements in the bulk powder, powder density, particle size distribution, concentration of free zirconia, and coating thickness were developed. This research was performed as a result of recent MRF work combining the effects of acid etching and mechanical removal of material into a single process, which made it necessary to both increase the corrosion resistance of the material, as well as to defining differences between the two iterations of the product. Several techniques were used to obtain the data necessary for analysis of the powders. A full factorial experiment was employed to determine what factors to alter in the powder production. Techniques including XRD, XPS, EDS, and XRF were all utilized in determining the relative mass fraction of the components present in the powder. Gas pycnometry and colloidal analysis were used to determine densities and particle size distributions. Magnetic separation and centrifugation were used to isolate and condense the nonmagnetic free zirconia

present in the samples. Scanning electron microscopy (SEM) micrographs of particle cross sections enabled analysis of coating thicknesses. Alterations to the zirconia sol-gel synthesis and increased concentration of zirconia sol-gel during the coating procedure resulted in a ∼3.25x improvement to the corrosion resistance of the zirconia coated MR powder, when compared to powder produced using the old manufacturing process. Of the methods used to analyze mass fraction of MR powder compoents, XRF proved to be the fastest and most reliable. If further improvements in corrosion resistance are required, it is recommended to increase the thickness of the zirconia coating, or develop a dual coating of an acid resistant polymer and zirconia (although this may have adverse effects on the powder's magnetic potential).

Contributors and Funding Sources

This material is based upon work supported by the Department of Energy National Nuclear Security Administration under Award Number DE-NA0001944, the University of Rochester, and the New York State Energy Research and Development Authority. The support of DOE does not constitute an endorsement by DOE of the views expressed in this abstract. This research was made possible in part through Bruker's Tracer Research Grant Program directed by Dr. Bruce Kaiser, Chief Scientist. The Grant Program includes loan of a Tracer Portable XRF Analyzer and applications support in the pursuit of advancing elemental analysis research by established and aspiring scientists. This work made use of the Cornell Center for Materials Research Shared Facilities which are supported through the NSF MRSEC program (DMR-1120296).

Contents

List of Figures

List of Tables

Abbreviations

Abbriviation	Description	page
CVD	**C**hemical **V**apor **D**eposited	1
FLIR	**F**orward **L**ooking **I**nfra**R**ed	1
MRF	**M**agneto**R**heological **F**inishing	1
MR	**M**agneto**R**heological	1
LLE	**L**aboratory for **L**aser **E**nergetics	1
PV	**P**eak to **V**ally	2
RMS	**R**oot **M**ean **S**quare	2
STM	**S**pot **T**aking **M**achine	2
16TC-FF	**16 T**reatment **C**ondition **F**ull-**F**actorial experiment	3
ANOM	**AN**alysis **O**f **M**eans	3
ANOVA	**AN**alysis **O**f **VA**riance	3
NCP	**N**ew **C**oating **P**rocedure	3
OCP	**O**ld **C**oating **P**rocedure	3
XRF	**X**-**R**ay **F**luorescence	4

XPS	**X**-Ray **P**hotoelectron **S**pectroscopy	4
SEM	**S**canning **E**lectron **M**icroscopy	4
EDS	**E**nergy **D**ispersive **S**pectroscopy	4
ESA	**E**lectrokinetic **S**onic **A**mplitude	4
IR	**I**nfra**R**ed	5
HIP	**H**ot **I**sostatic **P**ressing	5
LANTIRN	**L**ow **A**ltitude **N**avigation and **T**argeting **I**nfra**R**ed for **N**ight	6
LWIR	**L**ong-**W**ave **I**nfra**R**ed	6
DOF	**D**egree **O**f **F**reedom	7
CNC	**C**omputer **N**umerical **C**ontrol	7
CI	**C**arbonyl **I**ron	8
XRD	**X**-**R**ay **D**iffraction	9
Hv	**V**ickers **H**ardness	9
IEP	**I**so**e**lectric **P**oint	11
PEI	**P**oly**e**thylene **I**mine	11
CCMR	**C**ornell **C**enter for **M**aterials **R**esearch	76
ΔMC	**C**hange in **M**ass **C**alculation	117

Chapter 1

Introduction and Motivation

Chemical vapor deposited zinc sulfide (CVD ZnS) is an infrared-transparent material with high hardness and fracture toughness, which makes this compound suitable for a wide variety of industrial and military applications. Common applications of CVD ZnS include missile domes and windows, and forward looking infrared (FLIR) cameras. Recent growth in the fields of freeform optic design and fabrication has increased the potential for CVD ZnS applications.

Magnetorheological finishing (MRF), a deterministic finishing technique developed in the 1980's, is currently an indispensable part of the manufacturing process of precision freeform optics. Research on MRF and magnetorheological (MR) fluids at the Laboratory for Laser Energetics (LLE) started in 1992, and by 2005 MRF was applied to the surface finishing of CVD ZnS. A byproduct of ZnS manufactured via the CVD process is the production of large grains on the surface, which grow conically outward from specks

of dust or imperfections on the substrate. When CVD ZnS is polished with MRF slurries of neutral or basic pH, the surface exhibits a texture resembling 'pebbles' or 'hillocks' [2]. This surface 'decoration' coincides with the grain structure and is caused by the anisotropic hardness of CVD ZnS.

In 2005 Kozhinova et al. [3] employed a new approach to minimize the surface texture of MR polished CVD ZnS by combining the effects of both mechanical removal and acid etching. The introduction of an acidic MR fluid required the development of a corrosion-resistant MRF powder. The micron-sized carbonyl iron (CI) particles that function as the MRF powder base corroded rapidly when exposed to a pH 4.4 solution. To address this problem, a zirconium butoxide solution gel (sol-gel) was developed and used to coat the CI particles. This newly-developed zirconium coated carbonyl iron (HQ-Zr) polishing powder could be exposed to a pH 4.4 solution for 150 h at 60°C without exhibiting corrosion [4]. When CVD ZnS was polished with HQ-Zr based MR fluid, the surface exhibited an increased peak to valley (PV) and root mean squared (RMS) surface roughness[5] when compared to results obtained with uncoated CI powder in an acidic MR slurry [3]. However, the HQ-Zr MR slurry showed no deterioration after 22 days of circulation in the MRF spot taking machine (STM), whereas the uncoated CI MR slurry exhibited limited pH and viscosity stability.

Chapter 2 reviews available literature on the production and applications of CVD ZnS, development of commercializable MRF technology, and the application of MRF to CVD ZnS. In Chapter 3, the process that lead to the development of highly corrosion-resistant zirconia-coated MR powder is described. Preliminary work focused on refinements to the

corrosion testing of MRF powder, and the effects that variations in MRF powder preparation had on corrosion resistance. Results of the early corrosion experiments initiated the design of a 16 treatment condition full factorial (16TC-FF) experiment intended to produce an improved HQ-Zr MR powder. Targeted areas of improvement consisted of an HQ-Zr MR powder that possessed an increased concentration of free zirconia nanoabrasives, improved corrosion resistance, and an increased period of stability in a pH 4.0 slurry.

The corrosion resistance of the 16 unique MRF powders created for the 4F 16TC FF are reported in Chapter 4. Results of the corrosion tests were processed with the analysis of means (ANOM) and analysis of variance (ANOVA) statistical tools, which were used to provide information on the significance of experimental factor settings. The experimental parameter set used to produce the powder with the highest corrosion resistance was defined as the new coating procedure (NCP) and was used in the manufacturing process of further powder batches. The set of parameters used to produce coated powder from 2009 [5, pg. 6808] – 2013 [6] was defined as the old coating procedure (OCP).

The measurement techniques used to characterize the OCP and NCP MR powders are discussed in Chapter 5. It was important to determine differences between MR powders that were produced using different procedures. There was also interest in determining the amount of free zirconia nanoparticles in the bulk powder. The characterization process was separated into two categories: (1) physical characteristics, and (2) quantification of elemental mass fraction. Density, corrosion resistance, particle size distribution, zirconia

coating thickness, and free zirconia were all measured. A variety of analytical X-ray techniques were used to quantify the elemental composition of many powder samples.

The results from powder characterization techniques are presented in Chapter 6. X-ray fluorescence (XRF) was used in conjunction with gas pycnometry to quantify the mass fraction of elements present in the powder samples. The phase and crystal structure of the MR powders was determined using X-ray diffraction, while X-ray photoelectron spectroscopy (XPS) was used to quantify the composition of the powder surfaces. Scanning electron microscopy (SEM) was used both to investigate surface characteristics of MR powders and to obtain semi-quantitative mass fraction information using energy dispersive spectroscopy (EDS). Particle size distribution was measured using an application of a dynamic colloidal technique known as electrokinetic sonic amplitude (ESA).

Merits and drawbacks of the analytical techniques used to characterize the MRF powders are discussed in Chapter 7. Long scan times and tedious sample preparation were two significant drawbacks seen in many of the analysis techniques. The presence of the zirconia coating on the micron-sized particles invalidated many assumptions commonly used in X-ray analysis. A generalized approach for the quantification of zirconia coated MRF powders was developed. Short analysis times with minimal sample preparation were emphasized, which enabled the measurement of powders to keep pace with the production of new MRF batches. The analysis procedure outlined in this chapter allowed us to perform quality control measurements on the stock of MR powder. The procedure can also be used for quantifying significant differences between powders if further alterations to the production method are introduced. Conclusions and suggestions for future work are presented in Chapter 8.

Chapter 2

Background and Literature Review

2.1 CVD ZnS

Early research on CVD ZnS and its applications to reconnaissance and weapon delivery systems was performed at Raytheon in 1970 [7, 8]. Chemical vapor deposited ZnS is an exceptional ceramic, with broad band transmission in the infrared (IR) spectrum, good mechanical strength, and high thermal stability [8–11]. Polycrystalline CVD ZnS is typically produced at 450°- 800°C under a 50 mbar vacuum, and exhibits an average transmittance of $\sim 75\%$ at wavelengths (λ) between $8 - 10$ µm [8, 9, 11, 12]. When exposed to hot isostatic pressing (HIP) at 990°C and 200 MPa for three hours the range

of transmission increases to $\sim 70\%$ for 0.8 µm $\leqslant \lambda \leqslant$ 11 µm [12, 13], which represents a significant increase in transmission in the visible spectrum.

Some of the most demanding uses for IR transparent materials include FLIR cameras mounted on F-18 fighters, domes on I^2R Maverick missiles, and windows for the F-15's low altitude navigation and targeting infrared for night vision (LANTIRN) systems [8]. Robust mechanical and thermal properties are extremely important in the aforementioned applications, as mechanical failure of the window or dome can result from supersonic collisions with dirt, insects, rain and aerothermal heating[10, 14, 15]. Although many other long-wave infrared (LWIR) transparent materials such as $CaLa_2S_4$, ZnSe, Ge, GaAs, GaP, and Si have been investigated [16, 17], each of these materials has flaws more significant than ZnS. These flaws include unsatisfactory thermal properties ($CaLa_2S_4$, Ge, GaAs), inferior mechanical durability (ZnSe), and significant absorption in the $8 - 14$ µm region (GaP, Si) [16]. While there are LWIR transparent materials with thermomechanical properties superior to CVD ZnS and HIP CVD ZnS (particularly glass-ceramics made from GeS_2 and Ga_2S_3), these materials are still in development [16, 18]. As such, CVD ZnS continues its more than 40-year leadership as an industry standard in field of broad band transparent materials.

2.2 MRF

The MRF technique was first investigated by William Kordanski and Leonid Gleb in 1987 [19]. Early iterations of MRF machines were very different from those used today.

These early machines used an optic adhered to a spindle rotating in a trough containing MR fluid (Fig. 2.1a) [20]. By 1995 a prototype of the vertical wheel MRF machine had been constructed; Fig. 2.1b [21] shows a schematic of the design. The ribbon of MR fluid becomes stiff as it passes through the magnetic field and travels over the carrier wheel. As the optic is pressed into the MR ribbon, significant shear stresses develop, resulting in the removal of material from the part [22]. The principal elements of the vertical wheel MRF are still used in state of the art MRF machines, such as QED Technologie's Q-Flex 300, which entered the market in 2014 [23, 24]. The Q-Fflex 300 has six degrees of freedom (DOF), and is capable of polishing spherical, plano, aspheric, and freeform optics to RMS roughness values of 3 nm, 7 nm, 6 nm, and 4 nm respectively [23, 25, 26].

Advances in optical design and manufacturing have seen a marked increase in the demand for production of freeform, aspheric, and conformal optics [22, 24, 27–31]. In order to manufacture finely polished freeform optics, the substrate material will typically undergo a four or five step process: (1) generation; (2) surface correction; (3) polishing; (4) sub-aperture polishing; and (5) final surface finishing [26, 28]. Computer numerical control (CNC) machining is used for generation and surface correction. A full aperture polishing technique, such as the VIBE technique developed by OPTIMAX [32], is used to reduce the MRF time [28]. Once the part has been polished, MRF is used to eliminate sub-aperture errors in form and produce the finished surface [26, 33]. In recent years, MRF has become an industry standard for deterministic, sub-aperature, conformal finishing of freeform optics [19, 24, 26, 27, 30].

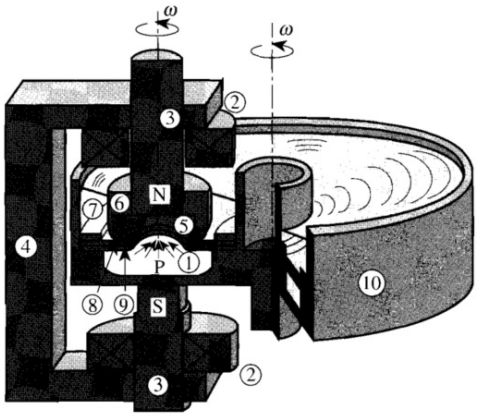

(a) Diagram of the trough MRF machine, an early design, used from 1990 – 1995. This Figure was taken from reference [20].

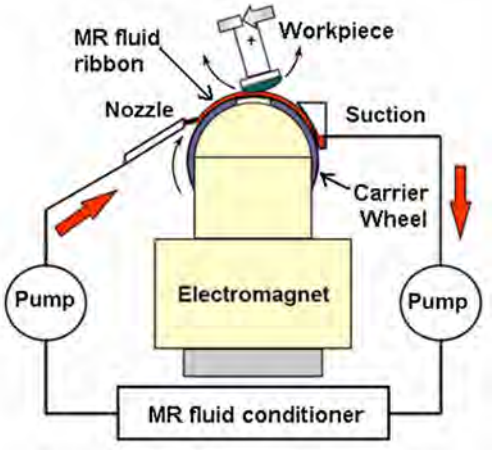

(b) Diagram of a vertical wheel MRF machine, used since 1995. Figure 2.1b was taken from reference [21].

Figure 2.1: Two MRF machine schematics. The diagram in Figure 2.1b remains the basis for state of the art MRF machines.

2.2.1 MRF of CVD ZnS

There has been significant interest in applying MRF to CVD ZnS for production of high-precision aspheric optics for IR windows and domes [3, 34–37]. Early polishing experiments were performed with 'standard' MR fluid, composed of: 36 vol% micron-sized carbonyl iron (CI) powder, 55 vol% water, 3 vol% surfactant or dispersant, and 6 vol% nonmagnetic ceria abrasives [35, pg. 258]. These experiments produced significant increases in surface roughness of the CVD ZnS when ~ 2 µm of material was removed, resulting in surface roughness < 22 nm RMS [3, 38].

Surface decoration, or 'pebbles', were more pronounced on the side of the CVD ZnS optic furthest from the substrate [3, 39]. The asymmetry between the two sides of the

CVD ZnS parts can be explained by the CVD growth mechanism. During deposition, ZnS will nucleate on dust-like particles on the mandrel surface, causing conical grain growth normal to the mandrel[6, 40]. X-ray diffraction (XRD) was used to identify the tree lattice orientations in the polycrystalline ceramic (100, 110, 111, and 311) [7]. Different lattice orientations exhibit a significant range in Vickers hardness (H_v) values [6, pg. 6]. Microindentation of the (111) cubic phase with 100 g resulted in a measured H_v of $\sim$ 2.9 GPa, while the (100) orientation of the hexagonal phase had a H_v of $\sim$ 1.9 GPa [7]. The disparity in cubic / hexagonal phase concentration [7, 41], coupled with a $\sim$ 1 GPa range in grain hardness provides an explanation for the CVD ZnS surface texture.

Further attempts to produce optically smooth CVD ZnS surfaces with uncoated CIP MR fluids were made. A set of experiments was performed to quantify bot the removal rate of the MR fluid and the PV and RMS roughness of the CVD ZnS surface [3, 34]. Four MR fluids were prepared to finish pre-polished CVD ZnS flats; each slurry contained a different nonmagnetic abrasive (ceria, diamond, silica, and alumina). The RMS roughness of the polished CVD ZnS flat increased from the initial 2.7 nm to 22 nm (ceria), 25 nm (diamond), 12 nm (silica), and 11 nm (alumina) after MRF. The increase in RMS roughness as material is removed is shown in Figure 2.2 [3]. Additionally, 'pebble' formations were still observable when more than 0.5 µm of material was removed [34, pg. 2]. The MR fluid containing with alumina abrasives yielded a high removal rate of $\sim$ 3.5 µm/min [34, pg. 2], and has been used as an added abrasive in several other MR fluids [2, 42].

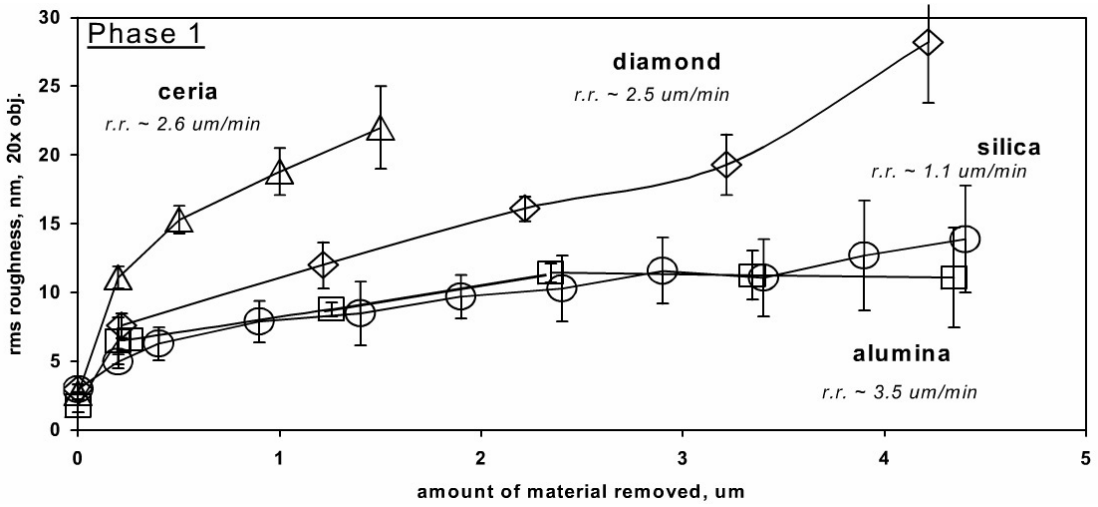

Figure 2.2: Development of increased RMS surface roughness of pre-polished CVD ZnS flat during MRF with MR fluids containing four different abrasives.

2.2.2 MRF of CVD ZnS with zirconia-coated CIP based MR fluid

In continued efforts to improve the surface quality of CVD ZnS polished with MR fluids, chemo-mechanical polishing was investigated by Kozhinova et al.[3]. The chemically-modified MRF fluid produced parts with surface roughness values of 25 nm PV and 2.5 nm rms. However, the CI powder in the low pH MR fluid was not stable and corroded too quickly for practical use [38]. Significant improvements to the corrosion resistance of CI powder based MR fluids were developed by Shafrir et al. in 2009, through the development and production of zirconia-coated CIP [5]. The zirconia coating on the CI particles was deposited using a sol-gel coating technique. Scanning electron microscopy was used for characterization of the zirconia-coated MR powder by Shen et al. [4] which confirmed both that the zirconia coating on the CI powder was continuous, and that its thickness could be adjusted by altering the sol-gel precursor concentrations. Although pH 8 MRF slurries with zirconia-coated CI powder base are known to be stable for over

two weeks, when these fluids were used to polish CVD ZnS the areal RMS roughness of the polished substrate was 4.50 ± 0.38 nm [5, pg. 6807], which is insufficient for commercial applications.

Production of a stable acidic zirconia-coated MRF slurry has proven to be a non-trivial task, as the zirconia coating creates a hydrophilic surface that significantly alters the surface chemistry of the powder [5, 38, 43]. Flocculation of the coated powder in a ≈ 7.0 pH slurry was caused in part by the slurry's proximity to the isoelectric point (IEP) [43]. The IEP is defined as the pH at which molecules in a slurry carry no surface charge [44] and will exhibit maximum viscosity [45]. The pH of MRF slurries must be > 4.0 pH units away from the IEP to perform well. The IEP for the zirconia-coated particles in an aqueous solution was determined at pH 7.2 ± 0.5 by Skarlinski et al. [43]. To produce an acidic MRF slurry, the IEP must be moved to the alkaline region.

Rheological properties of the MR fluid were further improved by Salzman et al. through the addition of polyethylene-imine (PEI) as a dispersing agent [6]. Addition of PEI altered the IEP of the slurry to the alkaline region, which improved acidic slurry characteristics. Zirconia abrasives (50 nm) were added to the chemically-modified MRF slurry, which was used to polish four pre-polished single crystal ZnS samples at crystallographic orientations of (100), (110), (111), and (311) to investigate variations in removal rate and surface finish [6]. Magnetorheological finishing spots were created with the STM, a single axis MRF machine [46],using slurry pH values of 4, 5, and 6. The slurry pH was altered by the addition of nitric acid; this action produced large variations in slurry viscosity (47 cP at pH 4, 108 cP at pH 5, and 194 cP at pH 6). All samples polished

with these slurries displayed high areal RMS roughness values ($\approx$ 8.7 nm at pH 4, $\approx$ 12.7 nm at pH 5, and $\approx$ 19.1 nm at pH 6) [6, pg. 10]. It is unclear why the roughness values produced from this experiment were so much higher than those produced by Kozhinova et al. [3]. Salzman et al. speculate that high roughness may be partially attributed to an insufficient quantity of zirconia abrasives in the slurry [6]. Research efforts to produce finely finished CVD ZnS surfaces using chemically modified MR slurries with a zirconia-coated CIP base are ongoing.

Chapter 3

MR Powder Production

3.1 Introduction

This chapter begins with a description of two production techniques for MRF powder and alterations that were implemented to improve its corrosion resistance. The second portion of this chapter provides an overview of the of techniques and instrumentation used to characterize a variety of MRF powders.

3.2 Production of MRF Powder

A three step process was used to make zirconia-coated MR powder. This process consists of: (1) preparing a zirconia solution gel (sol-gel), (2) dispersing the carbonyl iron in a sol-gel and DI water solution, and (3) washing and drying of the final product. The

procedure described below was used from 02/14/2010 until 07/10/2013 and is referred to as the original coating procedure (OCP).

3.2.1 Zirconia Sol-Gel

The production of zirconia sol-gelis a six-step process requiring: DI water, zirconia butoxide, and fuming nitric acid. All work was done in a fume hood, and proper personal protection equipment must be worn including: a lab coat, safety glasses, nitrile gloves, and closed-toe shoes. One liter of DI water was added to an Erlenmeyer flask with a magnetic stir-bar, which was placed on an electric stir-plate and set to stir at 400 RPM. Seventy-three mL of zirconium butoxide and 30 mL of nitric acid are added to 100 mL graduated cylinders. The zirconium butoxide was slowly added to the mixing DI water. Nitric acid was slowly added to the zirconium butoxide DI water solution. The top of the Erlenmeyer flask is covered with parafilm and left to stir overnight. Figure 3.1a shows the resulting sol-gel shortly after mixing, which changes from cloudy-white to transparent over-night. Figure 3.1b displays the transparent zirconium butoxide. The Erlenmeyer flask was labeled with the start-date of the process. A flow diagram of this process is provided in Appendix A.

3.2.2 Coating of Carbonyl Iron with Zirconia Solution Gel

First, 600 g of DI water was added to a 3-neck round-bottom flask, followed by 200 g of HQ carbonyl iron from BASF. The flask is shaken before placing it into an ultrasonic

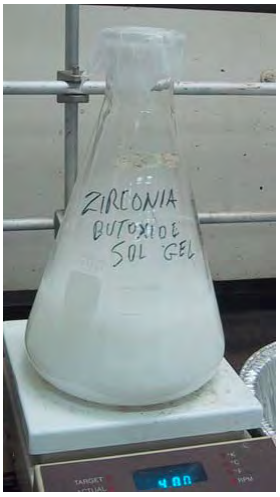

(a) Zirconium sol-gel immediately after all components have been added.

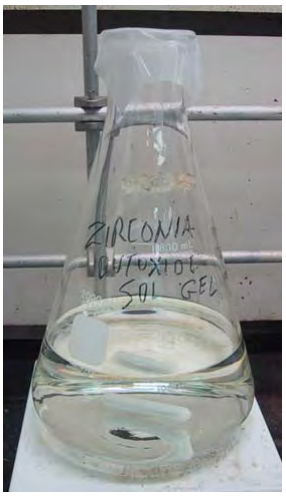

(b) Zirconium sol-gel after ≈ 15 hours of mixing.

Figure 3.1: Zirconium sol-gel synthesis.

bath, set to power level #9 for 30 minutes (Figure 3.2a). The flask was transfered to the fume hood, which contains an electric motor suspended from a fume hood lab-frame. Below the electric motor is a metal bucket resting on a hot plate. A Teflon stirring rod bearing is inserted into the center neck of the flask. A two inch glass stir-rod with a Teflon stirrer at its base was inserted into the Teflon bearing (Figure 3.2b). The flask was placed into the metal bucket. The top end of the glass stir-rod was inserted into rubber tubing protruding from the drive shaft of the electric motor. The metal bucket was filled with warm water. The electric motor was turned on and set to a speed such that there was a sizable vortex in the flask. Figure 3.2c displays the full system; two batches were made at a time. Four-hundred mL of zirconia sol-gel was added to the flask. The hot-plate was turned on and set to 70°C. After the flask has been held at 70°C for four hours, the hot plate was turned off and left to stir over-night.

(a) The triple-neck round-bottom flask with DI water and CI-HQ in the ultrasonic bath.

(b) Triple-neck round-bottom flask with teflon bearing and glass stirring rod inserted into the flask.

(c) Two batches being mixed. Electric motors shown at top, water baths holding the round-bottom flasks resting on hot-plates shown below.

Figure 3.2: Several images of the carbonyl iron coating procedure.

3.2.3 Zirconia-Coated CI Particle Drying Procedure

The electric motor shown in Figure 3.2 was turned off. The flask was taken out of the fume hood, rested on a cork stand and left to settle for approximately 0.5 hrs. The supernatant was carefully decanted into a 2 L beaker, while ensuring that the minimal amount of particles were wasted. The coated particles were poured into a 2 L crystallization dish (Figure 3.3a), and DI water was added to the flask to rinse the remaining particles into the crystallization dish. More DI water was added to the crystallization dish until it was three quarters full. The solution was agitated with a plastic policeman/spatula. The crystallization dish was rested on a large magnet, to increase the rate which the particles settle (Figure 3.3b). The supernatant was transfered

from the 2.0 L beaker to a hazardous waste container for disposal. After ≈ 15 min, the particles were almost completely settled. The DI rinse water was carefully decanted from the crystallization dish, and the wash process was repeated. The waste water from the wash process was neutralized with sodium bicarbonate.

The crystallization dish was transferred to the counter. A plastic Erlenmeyer flask was connected to the central vacuum system, the ceramic funnel was placed into the top of the Erlenmeyer flask, and a piece of filter paper was placed in the top of the funnel. The vacuum was turned on and the filter paper was moistened to create a good seal. The coated particles were poured into the ceramic funnel (Figure 3.3c) and DI water was sprayed into the crystallization dish to rinse the remaining particles into the funnel. When most of the water had been pulled through the powder into the funnel, 200 mL of ethanol was added to the powder to aid in removal of residual moisture. As cracks began to form in the powder cake (shown in the right half of Fig. 3.3d) a spatula and Scoopula were used to smooth them out, aiding in a quicker and more uniform drying process.

After approximately 30 minutes the vacuum was turned off and the particles were transfered to a petri dish lined with aluminum foil. A Scoopula was used to break up the clumps of powder. The petri dish was moved into the vacuum oven (Figure 3.3e), and the particles were baked at 60°C under a mild vacuum (1 ∼ 18 in. of Hg). The vacuum was broken after 30 minutes to wipe condensation from the interior of the oven. The level of condensation is similar to that shown in Figure 3.3f. This process was repeated as needed. The particles were baked overnight. In the morning, the powder was

transfered to a mortar and milled for approximately seven minutes with a pestle until no agglomerations remained (Figure 3.3g). The final zirconia-coated MR powder was transfered to a plastic cup, which was labeled with: the date of completion, name of the batch, final mass, and moisture content at the time of completion. The powder moisture content was analyzed with the Arizona Instruments Computrac Max-1000 (Figure 3.3h). The average mass of 71 NCP MR powder batches is 229.7 g $\pm$ 5.1 g, which represents a $\sim$ 30 g increase from the initial 200 g of CI powder. The average mass of five OCP MR powder batches is 213.5 g $\pm$3.7 g.

(a) The zirconium butoxide and CI-HQ slurry being poured into a crystallization dish after over-night mixing.

(b) A side view of the crystallization dish resting on a magnet to increase the rate of particle settling.

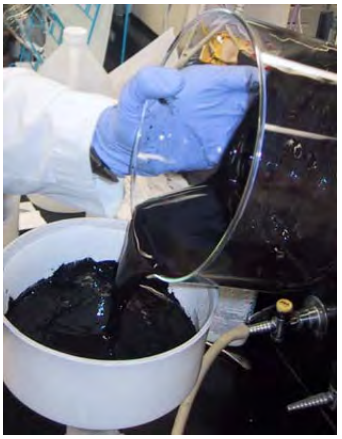

(c) Coated iron powder being poured into a ceramic funnel, preparing for preliminary vacuum drying.

(d) Top view of the powder being vacuum dried prior to being placed into petri dishes and loaded into the oven.

(e) A VWR model 1410D vacuum oven used for a variety of laboratory heating and drying applications.

(f) Condensation accumulating on the interior of the vacuum oven after approximately one half hour of drying.

(g) Dried MRF powder that has been freshly milled, prepared to be transfered to a plastic cup for storage.

(h) An Arizona Instruments Computrac Max-1000 moisture content analyzer used to determine moisture content of various laboratory samples.

Figure 3.3: Highlights of significant steps in the carbonyl iron drying procedure.

3.2.4 Production of 325 Mesh MRF powders

It was determined that using the coating techniques described above on a powder of larger particle size could provide some useful insights. It was thought that the zirconia coating thickness may be more easily seen on SEM micrographs of larger coated particles. Coating larger particles also provides another mass fraction calibration point when attempting to develop a mass fraction calibration curve for a variety of powders. This type of calibration is necessary for determining the coating thickness of powders when using a technique like XRF. It also provides a "sanity check" reference point, as the mass fraction of iron in these coated powders should be larger than the standard smaller particle size batches. There should also be measurable differences in density.

The volume fraction of components was maintained when making the MR powder batches with the larger iron powder. There was some initial concern that the change in particle size and surface area might affect the coating procedure. An attempt was made to maintain a consistent ratio between total powder surface area and volume of solution, but the variation in particle size made this impractical. Dimensional analysis showed the small volume fraction of powder in the sol-gel for both the OCP and NCP procedures (Table 3.1).

Table 3.1: The volume fraction of components used to make MRF powder batches for both the old and new coating procedure.

(a) Volume fraction of components used in the old coating procedure.

Component	Volume Fraction (%)
Carbonyl iron	2.5
Deionized water	58.5
Zirconia sol-gel	39.0

(b) Volume fraction of components used in the new coating procedure.

Component	Volume Fraction (%)
Carbonyl iron	1.6
Deionized water	38.4
Zirconia sol-gel	60.0

3.3 Improving Corrosion Resistance of MRF Powder

Variability between MRF batches was investigated. One of the most important characteristics of the powder is its corrosion resistance. Determining the corrosion resistance of the powder is important, as many $\sim$ 130 g batches are needed to produce a slurry used to polish parts on the STM, and one 'bad' batch could lead to the early failure of an entire slurry.

Previous corrosion experiments of zirconia-coated MR powder had been conducted by Shen et al. using the discoloration of the slurry supernatant to indicate corrosion of the coated powder [4]. A new corrosion experiment was designed to investigate variability between MR powder batches; this experiment included testing corrosion resistance of older batches produced in 2009. The development of a new corrosion experiment underwent four iterations, and initiated the 16TC-FF experiment designed to identify alterations in the manufacturing process to increase the corrosion resistance of the MR powder.

3.3.1 Screening Experiments

This experiment began with the production of five MR powder batches, following the procedures outlined in Section 3.2 and Appendix A. Alterations to the drying procedure were introduced for these five batches. Preliminary corrosion tests were performed on these batches to develop a standard for corrosion testing; acid type and concentration were adjusted, along with sample size and mixing method.

Batches are labeled "HJR-#X", where '#' signifies the batch number and 'X' represents the drying procedure for that portion of the batch. Procedure 'A' signifies the sample was dried overnight in a vacuum oven at vacuum between 18–30 in. Hg at 60°C (Fig. 3.3e). Procedure 'B' was dried at 60°C overnight in a convection oven (Fig. 3.4) in an attempt to reduce drying time. Procedure 'C' involved a combination of ambient air drying, placement in a desiccator, or drying in the convection oven at 37°C. All batches were dried until the moisture content was below 1.0%, as determined by the Arizona Instruments Computrac Max-1000 (Fig. 3.3h).

Figure 3.4: A VWR model 1350FD vacuum oven used for a variety of laboratory heating and drying applications.

Batches labeled HJR 6[A,B] & 7[A,B] included single independent alterations to the

manufacturing process. The CI-HQ powder in HJR batch 6 was milled for 10 minutes prior to addition of DI water and ultra-sonication. It was thought that sonication may not completely remove all agglomeration in the CI-HQ powder. Agglomerations may break apart, exposing easily corroded CI-HQ particles that greatly increase the rate of corrosion. The order of components added to create the sol-gel for HJR-7 was altered by adding the nitric acid to DI water before zirconium butoixde to investigate the effects that alterations to sol-gel synthesis have on the coating. Half of each batch was dried at the standard 60°C and the other half at 100°C at vacuum between 18–30 inHg overnight, followed by a two nights in the desiccator.

3.3.1.1 First Corrosion Screening Experiment

The first screening experiment was designed to introduce the MR powder into an acidic pH 4.0 environment, similar to that of the slurry loaded into the STM. Samples HJR-3[A,B,C] were tested. For these samples, the drying procedure was derived from Subsection 3.2.3. This experiment was performed to determine what effect drying environment had on the corrosion resistance of the powder.

Solutions of dilute acetic and nitric acid were prepared by adding one drop of acid to 200 mL of DI water followed by further dilution to pH 4.2 with DI water to an acid concentration of $\sim$ 0.25%. These very dilute acid solutions were created so that the corrosion process would take long enough for different stages of corrosion to be easily characterized. Eight vials were prepared, each containing 0.2 g of coated particles from the three sub-batches of HJR-3. Two additional vials containing uncoated CI powder.

(a) Corrosion testing samples at the start of the experiment, shortly after agitation. Four samples in dilute acetic acid on the left, and four samples in dilutenitric acid on the right.

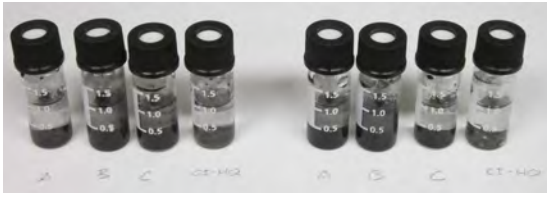

(b) Corrosion testing samples after ≈120 hours, showing no signs of corrosion.

Figure 3.5: The first iteration of corrosion experiments, using 1.5 mL vials and dilute pH 4.2 nitric and acetic acids. The four samples on the left of each sub-figure are in dilute ($\sim$ .25%) acetic acid, while the four samples on the right are in dilute ($\sim$ .25%) nitric acid.

Four vials were filled with 1.5 mL of dilute acetic acid solution, four additional vials were filled with 1.0 mL of dilute nitric acid solution. The samples were labeled and placed in a fume hood and observed qualitatively over the course of the next 120 hours for changes to supernatant color or powder appearance. No signs of corrosion were observed after this time period (Fig. 3.5).

3.3.1.2 Second Corrosion Screening Experiment.

The concentration of the acid was increased in this experiment to speed up the reaction time. In this experiment four concentrated acids (glacial acetic, fuming nitric, hydrochloric, and phosphoric) were observed to determine how quickly they would corrode MR powders. This experiment compared a recently made batch (HJR-5[A,B,C]) and a batch of OCP MR powder manufactured in 2009 (HQ-Zr 18). Five vials of powder were prepared for each acid: (HJR-5A) 60°C vacuum dried, (HJR-5B) 60°C convection

oven dried, (HJR-5C) 37°C convection oven dried, HQ-Zr 18 from 2009 (vacuum dried at 60°C), and uncoated CI-HQ was used as a baseline for corrosion susceptibility.

Figure 3.6d and 3.6e on page 26 show that phosphoric and hydrochloric acids both react immediately and violently with the particles; these acids were not used in further testing. The remaining samples were only exposed to concentrated acetic and nitric acids. There was evidence of some particle corrosion in nitric acid after 2.5 hours, shown by supernatant discoloration (Fig. 3.6b). The supernatant of the CI-powder samples had darkened in both acids. There was no visible corrosion of zirconia-coated samples in the acetic acid solution. The supernatant of all nitric acid-containing solutions continued to darken over the next 1.75 days. The supernatant of zirconia-coated powder in acetic acid samples showed limited discoloration. By the end of the experiment, the CI-powder sample had completely corroded. The HQ-Zr 18 sample exhibited the least supernatant discoloration, followed by HJR 5(A-B) vacuum dried batches, with the convection dried, air dried and uncoated particles showing the most supernatant discoloration (Fig. 3.6c).

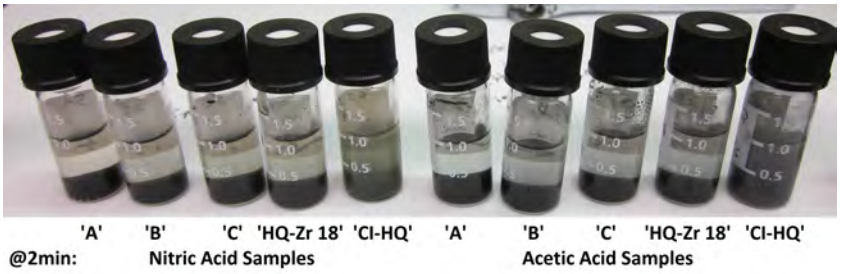

(a) Beginning of nitric and acetic acid corrosion test. Samples in nitric acid are on the left, samples in acetic are on the right.

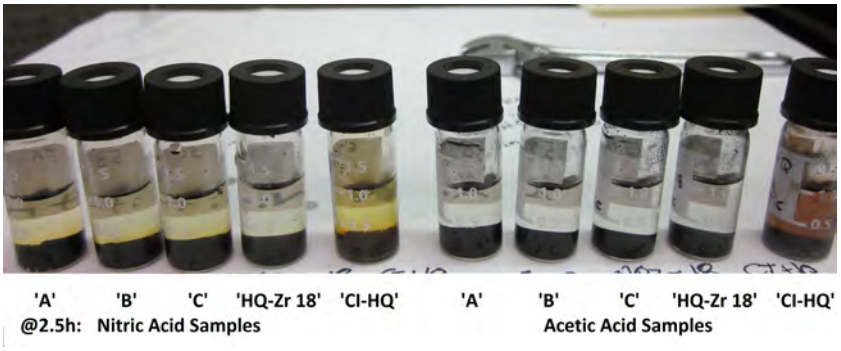

(b) 2.5 hours into the nitric and acetic corrosion test. The supernatant of the nitric samples exhibit a yellow hue, samples in acetic remain clear except for the CI, which has developed an orange-red hue.

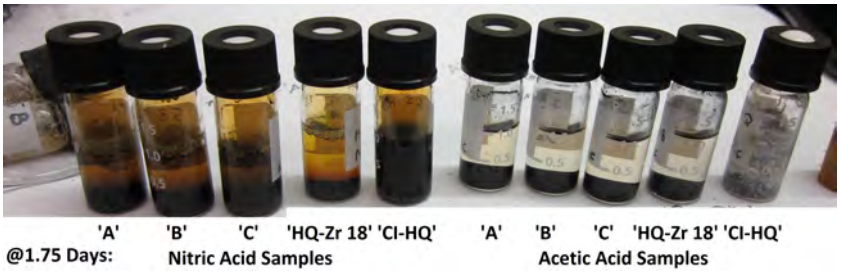

(c) 1.75 days into the nitric and acetic acid corrosion test. The supernatant of the nitric acid samples has turned an orange rust color, the supernatant of the samples in acetic acid remain mostly clear, and the CI has bubbled and foamed.

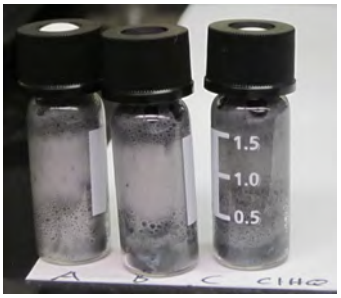

(d) Phosphoric acid immediately corroded HJR 5(A-C) samples, no others were tested.

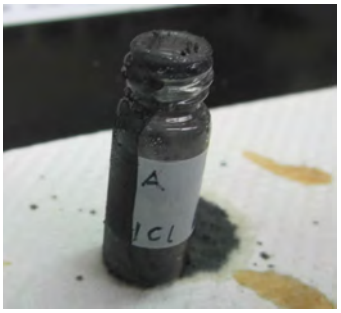

(e) Hydrochloric acid immediately corroded the HJR 5A sample, no others were tested.

Figure 3.6: Response of HJR 5(A-C), HQ-Zr 18, and CI-HQ powders to concentrated: acetic, nitric, phosphoric, and hydrochloric acids.

3.3.1.3 Third Corrosion Screening Experiment

In these experiments, the sample pH as a function of exposure to the acids was determined to provide a more accurate picture of corrosion resistance for the MR particles, rather than relying on visually observable alterations to the supernatant color of the samples. The violent reactions observed with hydrochloric and phosphoric acids lead to discontinuation of corrosion testing with these acids. Several concentrations of nitric and acetic acid were tested with the intent of finding a concentration of acid where corrosion could be observed in under eight hours. It was also desirable to have the volume percent of zirconia-coated powder be as close to 40% as possible, which is the volume percent used to produce MRF slurries used for STM experiments in the MRF lab. Due to the 6 g MR powder sample mass, a 10 vol.% zirconia-coated MR powder was used to prepare a dispersion in 8 mL of acid solution. Higher concentrations of MR powder would have made pH measurements of the supernatant impossible. Ten volume percent of zirconia-coated MR powder was tested in solution with the following solution compositions: 100% glacial acetic acid; 50% acetic acid / 50% DI water; 75% acetic acid / 25% DI water; and 68% nitric acid / 32% DI water. The pH of all samples was measured after preparation at regular intervals using litmus paper. The results of these experiments can be seen in Figure 3.7 on page 28.

All of the experiments with glacial acetic acid confirmed the hypothesis that both the zirconia-coated MR batches made in 2009 (HQ-Zr 6 & 18) and the recently made

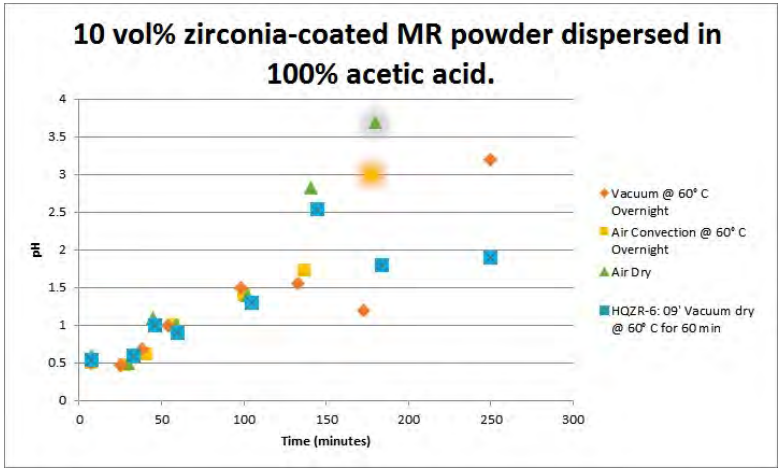

(a) 10 vol% zirconia-coated MR dispersed in 100% acetic acid. HJR-1(A-C) and HQ-Zr 6 from 2009 were tested.

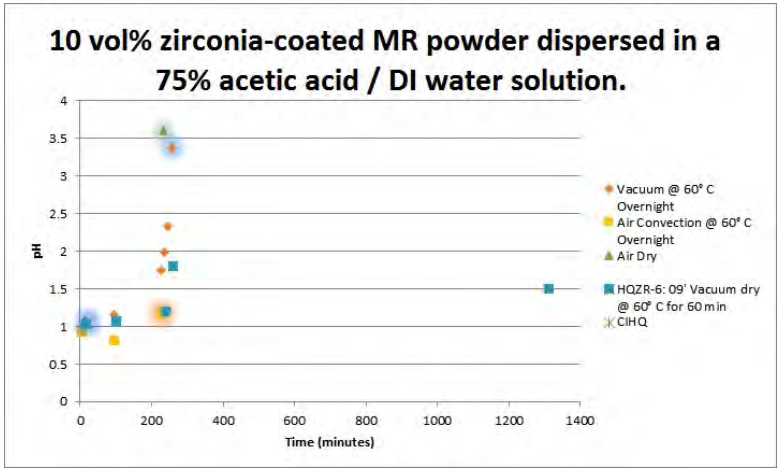

(b) 10 vol.% zirconia-coated MR dispersed in 75% acetic acid and 25% DI water. HJR-3(A-C) and HQ Zr-6 from 2009 were tested.

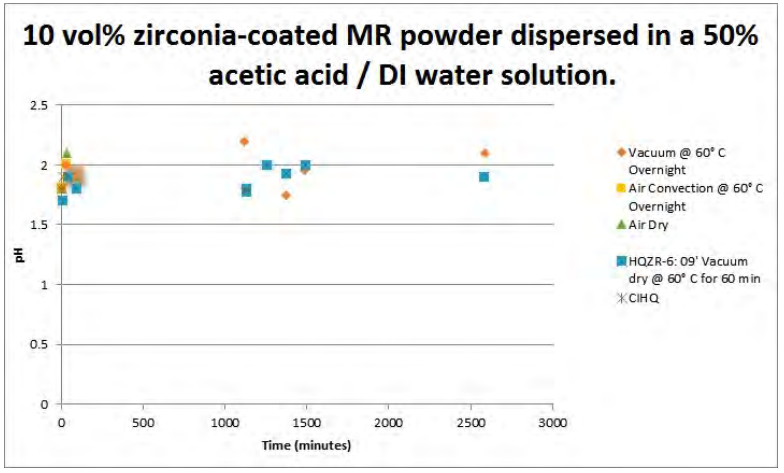

(c) 10 vol.% zirconia-coated MR powder dispersed in 50% acetic acid and 50% DI water. HJR-2(A-C) and HQ Zr-6 from 2009 were tested.

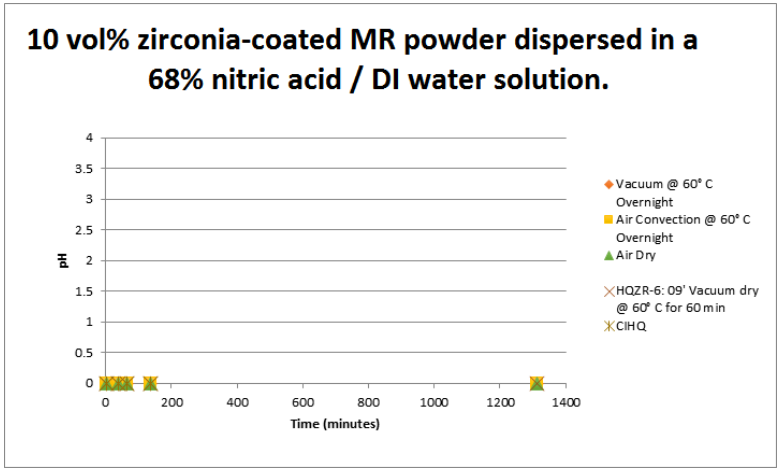

(d) 10 vol.% zirconia-coated MR dispersed in 68% nitric acid and 32% DI water. HJR-3(A-C) and HQ Zr-6 from 2009 were tested. The high concentration of the nitric acid pushed the pH to zero for all measurements, and no useful data could be collected.

Figure 3.7: Six grams of MR powder were added to 8 mL of acid solution. Behavior of several MR powders dispersed in varying concentrations of nitric and acetic acid, time of sample corrosion is identified by highlighted data points.

vacuum-dried batches HJR #(A-B) were the most corrosion-resistant. No useful results were obtained from the nitric acid experiment as the pH for all readings was too low and the corrosion of MR powder in nitric acid solution is not as obvious as the corrosion of the MR powder in acetic acid (Fig. 3.8). The glacial acetic acid was further diluted in the following corrosion experiments. Dilute acetic acid had several advantages over nitric acid; there was obvious corrosion of the samples, signified by large quantities of bubbling that can be seen in Figure 3.8b. The weak acid also has an easily adjustable solution pH when compared to a strong acid such as nitric acid.

(a) 10 vol.% MR powder dispersed in: 68% nitric acid and 32% DI water

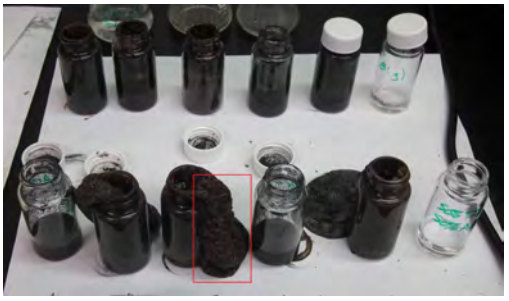

(b) MR powder dispersed in 100% acetic acid (top), and 50% acetic acid and 50% DI water (bottom). Foam produced during MR powder corrosion is highlighted.

Figure 3.8: MR powder in 50% acetic acid and 50% DI water corrodes and bubbles over the sides of the vial. Nitric acid solution and glacial acetic acid produce small bubbles and a black supernatant.

3.3.1.4 Fourth Corrosion Screening Experiment

It was determined that two independent alterations should be made to the batch preparation procedure, to investigate effects that these changes have on corrosion resistance on the MR powder. The CI-HQ powder in HJR batch 6 was milled for 10 minutes prior to addition of DI water and sonication. It was thought that sonication may not completely

remove all agglomeration in the CI-HQ powder. If thes agglomerations break apart and expose the easily corroded CI-powder particles, the rate of corrosion may increase and destabilize the MRF slurry. The order of component addition for preparing sol-gel for HJR batch 7 was altered by adding zirconium butoxide to DI water before nitric acid. All remaining steps in batch preparation remained the same.

The drying procedure was also altered for these two batches. Vacuum drying at higher temperature was investigated to determine the effect this has on MR powder corrosion resistance. After procuring an additional vacuum oven, half of each batch was dried at the standard 60°C and the other half at 100°C in a vacuum ranging between 18–30 in. of Hg overnight. In previous corrosion experiments, coated powders dried in the convection oven and in ambient room conditions showed poor corrosion resistance; these drying methods were no longer investigated. The moisture content of these powders was tested three times to test the precision of the Computrac Max-1000 moisture analyzer. Both the samples, dried at 60°C and 1000°C were analyzed as being $> 1\%$, which is above the allowed moisture content. Drying the samples in a desiccator for 2-3 days provided moisture reduction sufficient to store the material in a closed container.

A corrosion test was performed on HJR 6 & 7 in which 6 g of coated powder was dispersed in 8 mL of 50% glacial acetic acid solution. The composition of the acid solution was chosen to sustain pH stability during the second corrosion screening experiment (Fig. 3.7c, pg. 28). The 50% solution of acetic acid in DI water showed the most promise for corrosion testing; the pH was initially stable, and coated MR powders foamed during corrosion, which provides a useful qualitative indication of corrosion. Before pH was

measured, each sample was shaken for 10 seconds to ensure an evenly dispersed solution. Powders from batches HJR-5A, HJR (6-7), and HQ-Zr 6 were tested. The powder sample from batch HJR-5A was tested to provide a comparison between the old coating procedure and the alterations made in batches HJR (6-7). Sample HJR-5A corroded first, followed closely by HJR-6 dried at 100°C (Fig. 3.9). The corrosion of other samples occurred at some time during the night and could not be recorded. An important observation made during this experiment was that both HJR-5A and HJR-6 dried at 100°C corroded rapidly after agitation. This finding indicates that letting the particles settle between measurements results in an artificial increase in corrosion time.

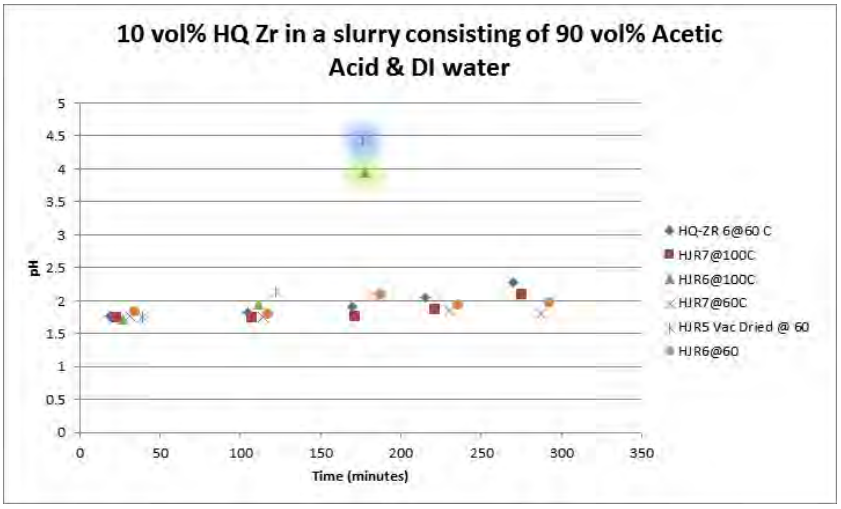

Figure 3.9: Corrosion test with 10 vol.% zirconia-coated CI dispersed in a 50% solution of acetic acid in DI water. HJR-6&7(60), HJR-5A and HQ-Zr 6 from 2009 were tested.

3.3.1.5 Fifth Corrosion Screening Experiment

During this iteration of the experiment, the concentration of zirconia-coated MR powder was maintained at 10 volume percent, dispersed in a 50% solution of acetic acid in

DI water. Powders from batches HJR-5A, HJR (6-7), and HQ-Zr 6 were tested. Magnetic stir-bars and a 9 location stir-plate were used to keep all samples agitated and homogeneous and ensure that the entire solution was at a uniform pH (Fig. 3.10, pg. 32).

This final corrosion experiment utilized nitric acid solution produced by dilution with water until a pH of 2 was reached ($\approx$ 6 µL of concentrated nitric acid in 356 mL of DI water). This dilution enabled detection of pH changes in the solution. An initial exponential increase in pH was observed, followed by a steady and continuous decline; a stable pH value was never reached in this experiment (Fig. 3.11b).

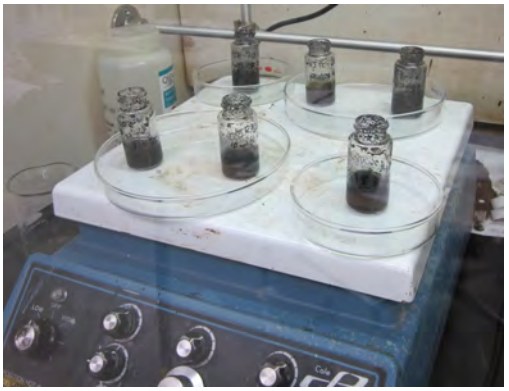

Figure 3.10: Dilute nitric acid corrosion test utilizing magnetic stir-bars and a 9 location stir-plate

All dispersions in nitric acid exhibited similar pH values after 50 hours, although the samples vacuum dried at 100°C had a more rapid initial pH increase.

All samples, except for HJR-6 dried at 100°C, corroded within an hour of each other (Fig. 3.11a). The powder sample from HQ-Zr 6 was the second sample to fail, as indicated by foaming of the dispersion. In other corrosion screening experiments the older powders had exhibited higher corrosion resistance. The intervals between corrosion times during this experiment were much smaller than those shown in Section 3.3.1.4, indicating that sample agitation is an important addition to the corrosion testing procedure.

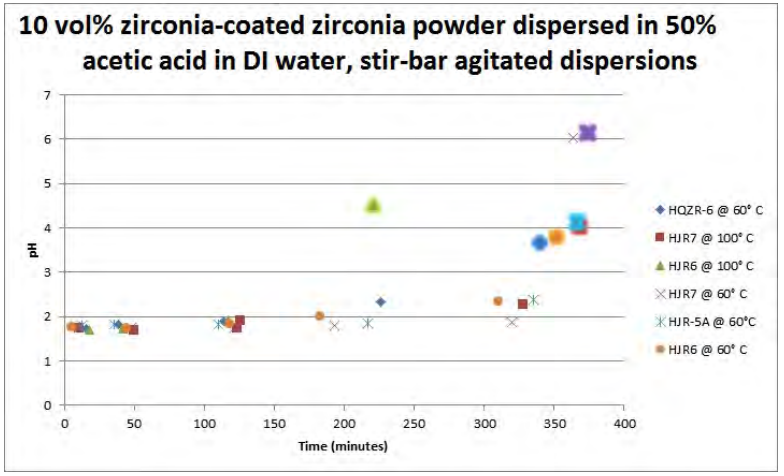

(a) 10 vol.% zirconia-coated MR powder dispersed in a 50% solution of acetic acid in DI water. HJR (6-7) dried at 60°C, HJR-5A and HQ Zr-6 from 2009 were tested. Samples were stirred using a small stir-bar on a 9 location hot plate. *HJR7@60°C had not completely corroded at the termination of this test.

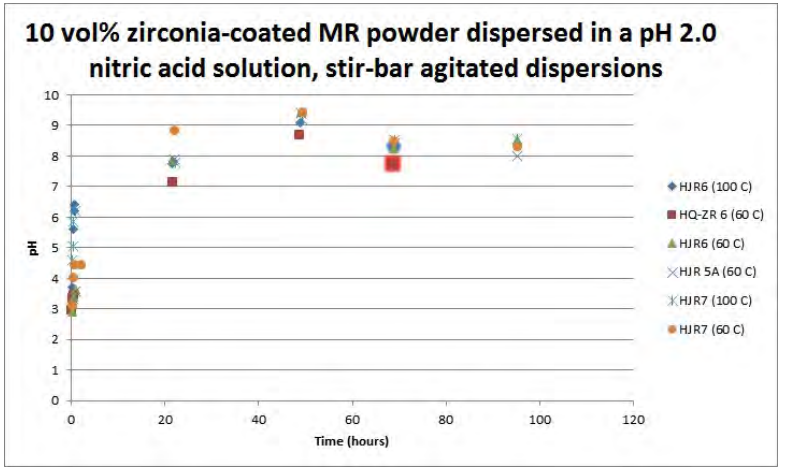

(b) 10 vol.% zirconia-coated MR powder dispersed in 2.0 pH nitric acid solution. HJR (6-7) dried at 60°C, HJR-5A and HQ-Zr 6 from 2009 were tested. Samples were stirred using a small stir-bar on a 9 location hot plate.

Figure 3.11: Results from the final corrosion screening experiments. (a) Samples in dilute acetic acid exhibit a stable pH and then a sharp rise upon initiation of corrosion. (b) Samples in dilute nitric acid exhibit an immediate pH increase, but do not show signs of corrosion for several hours.

3.3.2 16TC-FF Corrosion Resistance Experiment

The goal of this experiment was to improve corrosion resistance of zirconia-coated MR powders by introducing alterations to the batch production procedure. The MR powders produced for this experiment would be exposed to a corrosion tests to quantify which alterations to the powder manufacturing process would be implemented. A 16 treatement-condition full-factorial experiment was designed introduce alterations to the MR powder manufacturing process and investigate the effects that these alterations had on the corrosion resistance of the zirconia-coated powders. A full-factorial experiment was chosen, rather than a high-resolution or screening experiment, to better investigate treatment condition interactions [47]. The four factors that are most likely to affect corrosion resistance was the:

1. Pre-milling the uncoated CI-powder before ultra-sonication.
    (a) Sonication may not break up all agglomerations in the CI-HQ powder. If agglomerations were present, their breakup during polishing would expose uncoated CI-powder and increase the corrosion rate of the slurry. Introducing pre-milling of the CI-particles would decrease the likelihood of having agglomerations in the final product.
2. Altering the synthesis of the zirconium sol-gel.
    (a) This factor was designed to determine if the addition of zirconium butoxide before nitric acid would increase the corrosion resistance of the powder, due to alterations in sol-gel chemistry.
3. Increasing the zirconia sol-gel concentration during the coating phase of the procedure.
    (a) Increasing the sol-gel concentration would produce a more robust coating of the CI-powder particles. Addition of more free zirconia particles to the MR powder, will also act as an additional polishing abrasive.
4. Increasing the drying temperature of the coated particles.
    (a) Reduce drying time of the particles, limiting exposure to the $\sim$ pH 1.0 sol-gel.

The key for the chosen factor settings are described in Table 3.2; the '+' and '−' convention is used for the remainder of the text (Tables 3.2 and 3.3). Table 3.3 provides information on batch name, production date, and factor settings for all batches prepared, and tested in the 16TC FF corrosion experiment. The order of batch production was randomized to mitigate experimental error or environmental variations, although the latter is not believed to have been a significant issue as all work was completed in a fume hood under relatively constant conditions.

Table 3.2: Description of positive and negative factor settings in the 16TC FF corrosion experiment.

Factor	**Batch Alteration**	**Negative Factor Setting (−)**	**Positive Factor Setting (+)**
A	Drying temperature	60°C	105°C
B	Sol-gel concentration	40 vol.%	60 vol.%
C	Sol-gel synthesis order	Nitric acid added before zirconium butoxide (original method)	Zirconium butoxide added before nitric acid (new method)
D	Milling	No milling	10 minutes of milling

Table 3.3: 16TC FF, experimental settings and batch names

Name	Batch Produced	Milling	Sol. Gel Order	Sol. Gel Concen-tration	Drying Temp.	Sol. Gel Prep. Date
HJR 1A	5/2/13	-	-	-	-	5/1/13
HJR 6A	6/5/13	+	-	-	-	5/9/13
HJR 7A	6/5/13	-	+	-	-	6/4/13
HJR 9A	7/8/13	+	+	-	-	6/4/13
HJR 10A	7/10/13	-	-	+	-	7/9/13
HJR 11A	7/10/13	+	-	+	-	7/9/13
HJR 13A	7/16/13	-	+	+	-	7/15/13
HJR 12A	7/16/13	+	+	+	-	7/15/13
HJR 8B	7/2/13	-	-	-	+	5/9/13
HJR 6B	6/5/13	+	-	-	+	5/9/13
HJR 7B	6/5/13	-	+	-	+	6/4/13
HJR 9B	7/8/13	+	+	-	+	6/4/13
HJR 10B	7/10/13	-	-	+	+	7/9/13
HJR 11B	7/10/13	+	-	+	+	7/9/13
HJR 13B	7/16/13	-	+	+	+	7/15/13
HJR 12B	7/16/13	+	+	+	+	7/15/13

Several batches were prepared before the 16TC FF experiment was designed. Portions of these batches were dried in a manner not included in the full-factorial experiment; these drying processes included convection oven, ambient room environment, and low temperature vacuum oven drying. Batches dried using these procedures exhibited poor corrosion resistance in the corrosion screening experiments (Section 3.3.1), and were not included in the full-factorial experiment. The preparation methods for these batches are shown in Table 4.3. Even though these batches did not fit into the full factorial experiment, corrosion testing was still conducted to confirm the results found earlier in Section 3.3.1.

Table 3.4: Additional batch alterations not included in the four treatment condition, full factorial experiment.

Name	Start Date	Milling	Sol. Gel Order	Sol. Gel Concen-tration	Drying Temp. °C	Sol. Gel Prep. Date	Drying Conditions
HJR 1B	5/2/13	-	-	-	60	5/1/13	Convection Oven
HJR 1C	5/2/13	-	-	-	20	5/9/13	Ambient Conditions
HJR 2B	5/7/13	-	-	-	60	6/4/13	Convection Oven
HJR 2C	5/7/13	-	-	-	20	6/4/13	Ambient Conditions
HJR 3B	5/7/13	-	-	-	60	7/9/13	Convection Oven
HJR 3C	5/7/13	-	-	-	20	7/9/13	Ambient Conditions
HJR 4B	5/14/13	-	-	-	60	7/9/13	Convection Oven
HJR 4C	5/14/13	-	-	-	20	7/15/13	Ambient Conditions
HJR 5B	5/14/13	-	-	-	60	7/15/13	Convection Oven
HR 5C	5/14/13	-	-	-	37	5/9/13	Convection Oven
HJR 8A	7/2/13	-	-	-	20	5/9/13	Vacuum Oven

3.3.3 Full Factorial Corrosion Test Experimental Setup

Using the information gained from screening experiments outlined above in Subsection 3.3.1, the following important issues were resolved:

1. Volume percent of HQ Zr powder.
   (a) A zirconia-coated powder concentration of 10 vol% was selected to avoid producing an excessively viscous slurry.
2. Corrosion testing vessel.
   (a) To reduce waste and allow larger stir-bars to be used, 50 mL beakers were used for the mixing vessel.
3. Number of samples to be tested.
   (a) A group of five samples from each batch were tested to better characterize the average corrosion time of the batch and reduce the impact of outliers.
4. Acid type and concentration.
   (a) Glacial acetic acid (50 vol.% in DI water) was chosen for three reasons:
      i. The pH of acetic solutions in DI water remains stable until corrosion occurs.
      ii. The corrosion time of zirconia-coated MR powder in dilute pH 2.0 acetic solution occurs more rapidly than samples in dilute nitric acid.

iii. Corrosion of zirconia-coated MR powder in acetic acid results in a foaming of the dispersion (Fig. 3.8b), enabling use of digital imaging to identify corrosion times.

5. Method of slurry agitation.

   (a) Stir-bars were implemented to ensure sample homogeneity. Previous experience shows the importance of using the same size stir-bar for all samples; using different sized stir-bars produces a large variation in corrosion times.

6. Mixing speed.

   (a) To ensure that all samples were being mixed at 350 RPM, the rotational speed of the stir-plates was checked using a Strobotak optical tachometer device obtained from the LLE OML.

Methods used to execute corrosion testing on the zirconia-coated powder batches developed for the 16TC-FF corrosion resistance experiment are described in Appendix B. A cleaning procedure was developed to produce a consistent testing environment; this procedure is detailed in see Appendix C.

Chapter 4

Four Treatment Condition Full Factorial Experimental Results

4.1 Introduction

This chapter presents the results of the 16TC-FF corrosion experiment, which was designed to increase the corrosion resistance of the MR powder produced at LLE. Results of the 16TC-FF corrosion experiment are followed by ANOM and ANOVA of factor significance. A direct effect of altering the MR powder was the need to distinguish and quantify corrosion resistance between the OCP and NCP MR powders.

4.2 16TC-FF Corrosion Experiment

After completion of the 16TC-FF experiment, the corrosion resistance data was compiled and analyzed in Microsoft Excel. Table 4.1 displays the names, dates, and average corrosion times of MR powder batches that were tested for the full factorial experiment. Table 3.2 highlights the experimental factor settings used to make each batch. Batches HJR: 1A, 2A, 3A, 4A, and 5A were all produced under the same experimental setting. These five batches have an averaged corrosion time of 5.50 hours with a standard deviation for the average corrosion time of 3.49 hours.

Average corrosion time data for batches HJR 6A and 10A were unable to be properly documented due to poor image quality and camera battery failure that occurred after working hours. The first two MR powder batches tested, HJR 6A and 9B, utilized several different stir bar models during their corrosion experiments. All future experiments employed the same stir bar style to minimize experimental differences. For samples HJR: 6A, 9B, 11B, 10B, 6B, 1A, 8A, 12B and CI HQ , the stirring RPM uniformity was not verified. A stirring rate of 350 RPM was used for all batches tested after 7/23/2013; all stirring rates were confirmed using a Strobotak optical tachometer. Low RPM stirring rates were believed to be responsible for the increase in apparent corrosion resistance, because many of the samples in the screening experiments in Subsection 3.3.1 that were

not agitated appeared to last much longer (Fig. 3.7c).

Table 4.1: 16TC-FF corrosion experiment settings and results.

Name	Date Tested	Milling	Sol. Gel Order	Sol. Gel Concentration	Drying Temp.	Sol. Gel Prep. Date	Avg. Corrosion Time (hrs.)	Standard Deviation (hrs.)
HJR 1A†	7/17/13	−	−	−	−	5/9/13	9.35	2.33
HJR 2A	8/13/13	−	−	−	−	5/9/13	2.92	0.35
HJR 3A	7/30/13	−	−	−	−	5/6/13	2.13	0.18
HJR 4A	8/15/13	−	−	−	−	5/6/13	10.15	4.17
HJR 5A	8/12/13	−	−	−	−	———	2.94	1.00
HJR 6A†	7/11/13	+	−	−	−	5/9/13	———	———
HJR 7A	8/14/13	−	+	−	−	6/4/13	7.19	2.41
HJR 9A	———	+	+	−	−	6/4/13	10.42	4.07
HJR 10A	———	−	−	+	−	7/9/13	———	———
HJR 11A	8/13/13	+	−	+	−	7/9/13	13.24	4.78
HJR 13A	8/19/13	−	+	+	−	7/15/13	17.20	1.62
HJR 12A	8/19/13	+	+	+	−	7/15/13	15.29	5.62
HJR 8B	8/7/13	−	−	−	+	5/9/13	7.20	1.84
HJR 6B†	7/17/13	+	−	−	+	5/9/13	9.08	1.51
HJR 7B	8/20/13	−	+	−	+	6/4/13	7.80	3.00
HJR 9B†	7/15/13	+	+	−	+	6/4/13	8.23	1.55
HJR 10B†	7/16/13	−	−	+	+	7/9/13	8.87	0.64
HJR 11B†	7/16/13	+	−	+	+	7/9/13	7.52	1.27
HJR 13B	8/7/13	−	+	+	+	7/15/13	12.35	2.56
HJR 12B†	7/22/13	+	+	+	+	7/15/13	10.10	2.46

† Indicates corrosion experiments where stir-bar RPM was not confirmed to be 350.

§ (+) and (−) indicate factor settings used for the 16TC-FF corrosion experiment (Table 3.2).

Data in Table 4.1 shows a high variability in average corrosion time, indicating that several factors defined in Table 3.2 were significant. Standard deviations (σ) in corrosion times are also high, which suggests that either the powder may be inhomogeneous or there were fluctuations in the experimental environment. Table 4.2 highlights the results of the basic statistical analysis. The average corrosion time for the 16TC-FF experiment was 9.73 ± 2.26 hours. The factor settings used to produce the batches with the highest

average corrosion times, HJR 13A, 12A, and 11A, were all considered for modifying the old production method.

Table 4.2: Simple statistical analysis of corrosion times for MRF powder batches tested in the full factorial experiment.

Result (hrs.)	Average Corrosion Time (hrs.)	Standard Deviation (hrs.)
Average	9.89	2.46
Range	11.70	4.98
Maximum	17.20	5.62
Minimum	5.50	0.64
Median	8.98	2.13

† Corrosion times of batches produced using the same factor settings. HJR 1A, 2A, 3A, 4A, and 5A from Table 4.1 were averaged so as not to bias the results toward one batch production procedure.

Table 4.3 provides information on MR powder batches that were sol-gel coated using the OCP. Several batches were dried using methods not included in the full factorial experiment, including: convection oven drying, drying in an ambient room environment, and room temperature drying in the vacuum oven (Table 4.3). Although these batches did not fit into the 16TC-FF, they were corrosion tested to provide addition information.

The corrosion results for HQ-Zr 18 and CI-HQ powder samples are also included in Table 4.3. Sample HQ-Zr 18 was obtained from an MR powder batch produced in 2009, in accordance with the OCP. It was of interest to determine whether age was a factor in corrosion resistance. Sample from batch HQ-Zr 18 behaved very similarly with respect to corrosion as batches HJR 2A, 3A, and 5A. These four MR powders showed corrosion resistance that was $\sim 3\times$ worse than HJR 1A, and 4A. The uncoated CI powder was corrosion tested to provide information about the improvement in corrosion resistance

that the zirconia coating provided. With an average corrosion time of 6.9 min, it was confirmed that the uncoated CI powder was much more susceptible to corrosion than any of the zirconia-coated MR powders. Corrosion testing results for batches HJR 1B, 2B, and 3C were not obtained due to insufficient supply, as these three batches were heavily used in the screening experiments.

Table 4.3: Additional batches produced with alterations not included in the four treatment condition, full factorial experiment.

Name	Date Tested	Milling	Sol. Gel Order	Sol. Gel Concentration	Drying Temp. °C	Sol. Gel Prep. Date	Drying Conditions	Avg. Corrosion Time (hrs.)	σ (hrs.)
HJR 1B	———	–	–	–	60	5/1/13	Convection Oven	———	———
HJR 1C	8/12/13	–	–	–	20	5/9/13	Ambient	2.95	1.00
HJR 2B	———	–	–	–	60	6/4/13	Convection Oven	———	———
HJR 2C	8/19/13	–	–	–	20	6/4/13	Ambient	3.60	1.13
HJR 3B	8/19/13	–	–	–	60	7/9/13	Convection Oven	2.98	0.93
HJR 3C	———	–	–	–	20	7/9/13	Ambient	4.80	1.25
HJR 4B	———	–	–	–	60	7/9/13	Convection Oven	3.60	0.65
HJR 4C	8/14/13	–	–	–	20	7/15/13	Ambient	3.26	0.32
HJR 5B	5/20/13	–	–	–	60	7/15/13	Convection Oven	4.33	2.34
HR 5C	5/15/13	–	–	–	37	5/9/13	Convection Oven	6.54	4.18
HJR 8A	———	–	–	–	20	5/9/13	Vacuum Oven	10.22	3.00
HQ-Zr 18	9/14/13	–	–	–	60	———	Vacuum Oven	2.24	0.31
Uncoated CI powder	7/23/2013	N.A.	N.A.	N.A.	N.A.	N.A.	N.A.	0.12	0.004

Some statistics on the corrosion rates of the powders included in Table 4.3 are shown in Table 4.4 below. The results provided in Table 4.4 do not include the corrosion results of the uncoated CI powder. The powder sample from batch HJR 8A displayed the highest

average corrosion resistance of OCP powders, 10.22±3.00 hours. The sample from batch HQ-Zr 18 corroded the quickest, with an average corrosion time of 2.24 ± 0.31 hours.

Table 4.4: Simple statistical analysis of corrosion times for extra MR powder batches with alternate drying conditions, data taken from Table 4.3.

Result (hrs.)	Average Corrosion Time (hrs.)	σ (hrs.)
Average	4.45	1.51
Range	7.98	3.87
Maximum	10.22	4.18
Minimum	2.24	0.31
Median	3.60	1.07

The average corrosion time and standard deviation for all MR powder samples is shown graphically in Figure 4.1. It can be seen through a comparison of Tables 4.1, 4.3 and Figure 4.1 that batches 11A, 12A and 13A were the most corrosion-resistant. The common factors between these batches are their higher sol-gel concentration and lower drying temperatures. Samples HJR 1A and 4A appear to be outliers when compared with other batches produced using the OCP. The very large error bars in many of the batches was partially a result of only having five samples to test for each powder. Samples HJR 4A, 5C, 9A, and 12A are examples of those that have corrosion times with the most significant standard deviation.

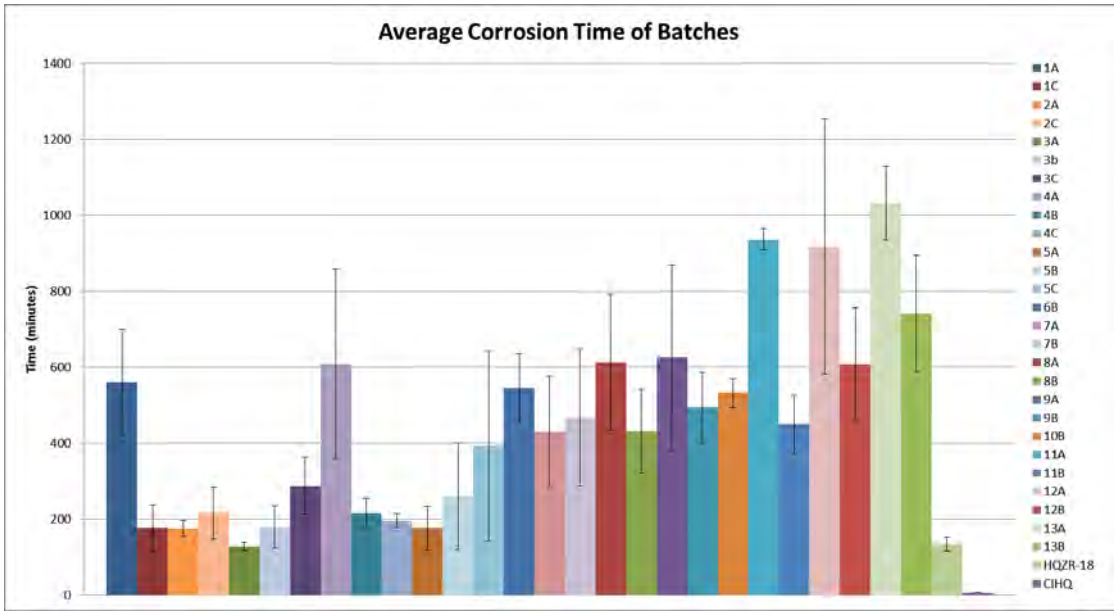

Figure 4.1: Average corrosion time for MR powder batches tested in the 16TC-FF corrosion experiment.

Several batches exhibited corrosion times greater than 10 hours; this extended corrosion time raised concerns that solution evaporation may artificially lower the apparent corrosion time. The onset of corrosion is defined as the time where foaming was apparent (Appendix C: Fig. C.1 pg. 184), or in some rare cases the solution viscosity would increase exponentially as as evidenced by the stationary stir-bar in the photographs (Appendix C: Fig. C.1c). The concern was that evaporation of the solution caused the stir-bar to stop rotating before the onset of corrosion was reached. An evaporation test was performed to determine the evaporation rate of water under the standard corrosion experiment conditions (Fig: 4.2). After 21 hrs the solution had noticeably thickened and the stir-bar stopped spinning after 28 hrs. Of the particles that were tested, samples from MR powder batches HJR 11A, 12A, and 13A survived >16.0 hrs. Two samples

from HJR 13A survived >18.0 hrs, and one sample from HJR 12A survived 21.4 hrs. Because the vast majority of samples corroded well before 21 hrs, solution evaporation does not have a significant impact on the outcome of the corrosion experiment.

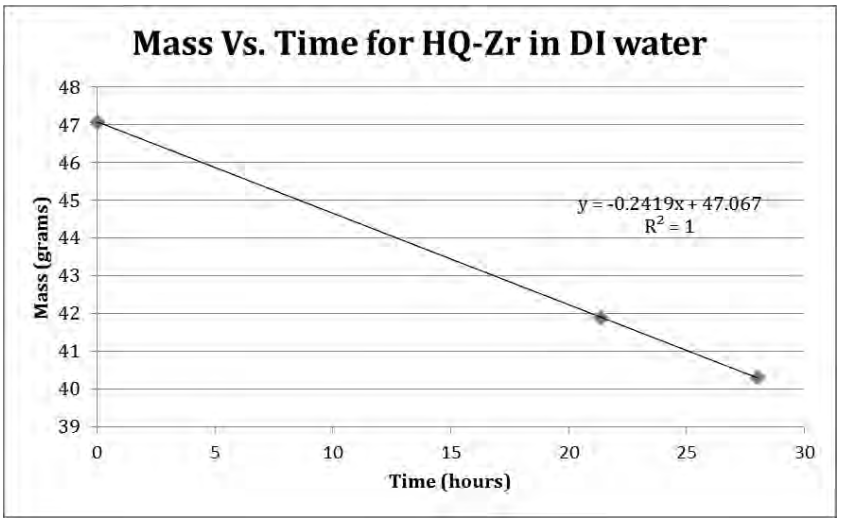

Figure 4.2: Evaporation-rate experiment. The experimental conditions used were consistent with the 16TC-FF corrosion experiment.

4.3 ANOM and ANOVA Analysis

An analysis of means (ANOM) was performed on the results of the full factorial experiment. This process provides insights to the most significant factors and factor interactions. Table 4.5 displays the factor experimental conditions, second level factor interactions, and columns dedicated to the estimation of error. The last two columns of each table represent the average corrosion time and standard deviation. This experiment has only one noise condition [47] (time of corrosion), the noise condition for each treatment condition is equivalent to its characteristic response. The rows labeled m_{+1}

and m_{-1} display the average weight the $+1$ and -1 setting for each column. The following row, labeled 'Δ', portrays the difference between the positive and negative factor settings; the larger the difference, the larger the impact of that setting [47]. The preferred factor setting is associated with the higher level of corrosion resistance. Columns 1, 2, 3, and 15 have the largest absolute 'Δ' values, indicating the significance of factors such as: drying temperature, zirconia sol-gel concentration, order of ingredient addition during synthesis of the zirconia sol-gel, and the interaction between drying temperature and zirconia sol-gel concentration. Factors, such pre-milling of the CI powder powder are of lesser importance. All error columns are have much smaller values than factor columns: 1, 2, 3, and 15. The presence of low 'Δ' values in the error columns indicates that the factors and interactions under investigation are much more significant than the columns dedicated to estimating error.

The results of the 16TC-FF corrosion experiment were also quantified through the analysis of variance (ANOVA) method, which is a statistical measure of the significance of factors and their interactions [47]. The primary information required for this analysis is the variance of each factor setting, which is determined from the sum of squares (SS) calculated for each factor. Each factor column has one degree of freedom (DOF). The five columns used to compute error designate five DOF (one DOF from each error column). The mean square (MS) is defined as the quotient of the SS and DOF. The F-ratio is the quotient of the factor's MS over error's MS. These F-ratios are compared to a critical value (F_{cr}); factors for which F-ratios $> F_{cr}$ indicate that the variance for that term is larger than what would be expected from sources of error. Values for F_{cr} can vary based

Table 4.5: ANOM for the full factorial corrosion experiment.

Batch	**Drying Temp.**	**Sol. Gel Conc.**	**Sol. Gel Order**	**Milling**	**e**	**e**	**e**	**C×D**	**e**	**B×D**	**A×D**	**e**	**B×C**	**A×C**	**A×B**	α	σ
HJR 1-5A	−	−	−	−	+	−	−	+	−	+	+	−	+	+	+	5.50	3.49
HJR 6A	−	−	−	+	−	+	+	−	+	−	−	−	+	+	+	7.68	1.36
HJR 7A	−	−	+	−	−	+	+	−	−	+	+	+	−	−	+	7.19	2.14
HJR 9A	−	−	+	+	+	−	−	+	+	−	−	+	−	−	+	10.42	4.07
HJR 10A	−	+	−	−	+	+	−	+	+	−	+	+	−	+	−	10.58	1.19
HJR 11A	−	+	−	+	−	−	+	−	−	+	−	+	−	+	−	13.24	4.78
HJR 13A	−	+	+	−	−	−	+	−	+	−	+	−	+	−	−	17.20	1.62
HJR 12A	−	+	+	+	+	+	−	+	−	+	−	−	+	−	−	15.29	5.62
HJR 8B	+	−	−	−	+	−	+	+	+	+	−	+	+	−	−	7.20	1.84
HJR 6B	+	−	−	+	−	+	−	−	−	−	+	+	+	−	−	9.08	1.51
HJR 7B	+	−	+	−	−	+	−	−	+	+	−	−	−	+	−	7.80	3.00
HJR 9B	+	−	+	+	+	−	+	+	−	−	+	−	−	+	−	8.23	1.55
HJR 10B	+	+	−	−	+	+	+	+	−	−	−	−	−	−	+	8.87	0.64
HJR 11B	+	+	−	+	−	−	−	−	+	+	+	−	−	−	+	7.52	1.27
HJR 13B	+	+	+	−	−	−	−	−	−	−	−	+	+	+	+	12.35	2.56
HJR 12B	+	+	+	+	+	+	+	+	+	+	+	+	+	+	+	10.13	2.46
m_{+1}	8.90	11.90	11.08	10.20	9.53	9.58	9.97	9.53	9.82	9.23	9.43	10.02	10.55	9.44	8.71		
m_{-1}	10.89	7.89	8.71	9.59	10.26	10.21	9.82	10.26	9.97	10.55	10.36	9.76	9.23	10.35	11.08		
Δ	-1.99	4.01	2.37	0.61	-0.73	-0.63	0.15	-0.73	-0.15	-1.32	-0.93	0.26	1.32	-0.91	-2.37		
SS	15.84	64.33	22.43	1.50	2.13	1.57	0.09	2.13	0.09	6.94	3.44	0.28	7.02	3.29	22.49		

on the confidence level 'P'. Confidence levels of P range from 0.90 to 0.99; a value of 0.95 is used most commonly, and was selected for this experiment [47]. The F_{cr} values for P = 0.90, 0.95, and 0.99 were determined to be: 4.06, 6.61, and 16.26 respectively [47]. For the purposes of this experiment, factors and factor interactions are considered significant if the F ratio is greater than 6.61. While ANOVA is very useful for setting a quantifiable value for significance, it provides no information on whether the m_{+1} or m_{-1} factor setting is preferable. The best effectiveness is achieved when ANOM and ANOVA are used in combination.

Results of the ANOVA calculation are shown in Table 4.6. Three of the four factors [drying temperature (A), zirconia solution gel concentration (B), and zirconia solution gel order of component addition (C)] are greater than the F_{cr} value; only pre-milling of the CI powder (D) was shown to be insignificant. The concentration of the zirconia sol-gel is the most significant factor, as increasing the concentration of sol-gel during the coating process is expected to produce a thicker zirconia coating on the particles. The second most significant factor was the order of component addition during sol-gel synthesis. Powder drying temperature was also significant; the lower drying temperature may reduce crack formation in the sol-gel coating caused by too-rapid loss of solvent at elevated temperature. Typically, factor interactions are less significant than factors; however, three factor interactions were also shown to be significant by ANOVA; these interactions were A×B, B×C, and C×D. The significance of first two interactions is not surprising, as both interactions involve two significant factors, but the significance of C×D indicates that there is a corresponding significant interaction between the order of

component addition during sol-gel synthesis and pre-milling of the CI powder. Another metric for designating significance is %SS, which shows the contribution a factor or interaction makes to the total SS. A significance threshold of 10% total SS was used in the last column of Table 4.6; by this metric only A, B, C, and A×B are significant.

Table 4.6: ANOVA from the full factorial corrosion experiment

Source	SS	DOF	MS	F	%SS
A	15.84	1	15.84	**17.89** *	**10.29** †
B	64.33	1	64.33	**72.69**	**41.82**
C	22.43	1	22.43	**25.34**	**14.58**
D	1.50	1	1.50	1.70	0.98
A×B	22.49	1	22.49	**25.41**	**14.62**
A×C	3.29	1	3.29	3.72	2.14
A×D	3.44	1	3.44	3.88	2.23
B×C	7.02	1	7.02	**7.93**	4.56
B×D	6.94	1	6.94	**7.84**	4.51
C×D	2.13	1	2.13	2.41	1.38
Error	4.43	5	0.89		
Total	153.82	15			

* Bold entries in the F ratio column designate values greater than an F_{cr} of 6.61 at a confidence limit of P = 95.
† Bold entries denote %SS values greater than 10% of the total SS.

The ANOM graph, shown in Fig 4.3, portrays the significance of factors and factor interactions. The significance of factors are determined by the height between m_{+1} and m_{-1}, while the significance of second level factor interactions is determined by the slope of m_{+1} to m_{-1} [47]. An analysis of Tables 3.2, 4.5 and Figure 4.3 shows that MR powders with higher corrosion resistance are produced by adding zirconium butoxide to

the sol-gel prior to nitric acid, using a 60 vol.% zirconia sol-gel, and by employing 60°C vacuum oven drying.

When investigating significant factor interactions, it is important to determine if the interactions are synergistic or anti-synergistic with respect to their factor settings. The significant factor interactions as determined by ANOVA were: A×B, B×C, and C×D as shown in Table 4.6. Figure 4.3 shows that the best setting for A×B is at m_{-1}, while best setting for factor A is m- and factor B is m_{+1} setting. To determine whether the A×B interaction is synergistic with factors A and B, compare the product of the best factor settings of A and B to the best setting of A×B: $m_{-1} \times m_{+1} = m_{-1}$. If the best setting for the interaction agrees with the product of the best setting for each factor, this interaction is synergistic. The interaction B×C is also synergistic, while C×D is anti-synergistic. As noted earlier in Table 4.6 factor D (pre-milling the iron powder) is not a significant factor.

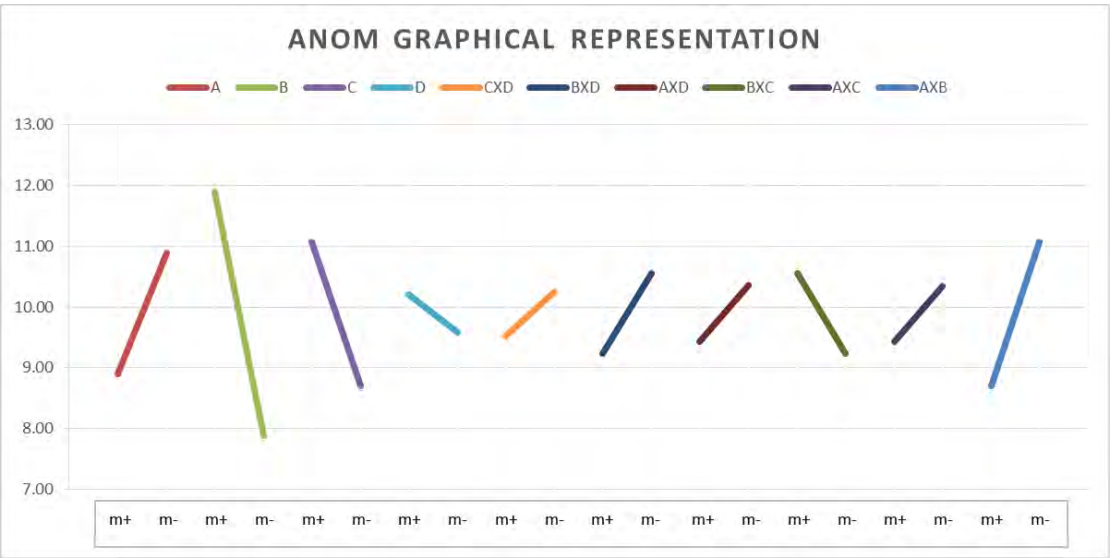

Figure 4.3: A graphical representation of the ANOM results. The m_{+1} setting is at the left of each line while the m_{-1} setting is at the right of each line. The significance of factors are determined by the height between m_{+1} and m_{-1}, while the significance of second level factor interactions is determined by the slope of m_{+1} to m_{-1}. Factors A, B, and C are significant, in addition to the A×B interaction.

Analysis using ANOM and ANOVA was also performed on the standard deviation of corrosion time (Table 4.1 and Fig 4.3). This exercise provides a useful check that the significance of factors and interactions are not being driven or overshadowed by their standard deviations. The analysis follows the same procedure as shown earlier in Tables 4.5 and 4.6, but in this case the average corrosion time (α column) is replaced with the natural logarithm of the standard deviation of corrosion times. Table 4.7 show the results of this ANOVA calculation. The standard deviation in corrosion times is not driving the significance of factors or interactions, since none of the factors or interactions are greater than F_{crit}. One notable result in Table 4.7 is the F ratio of B×D; this comparatively large number suggests that the large F-ratio seen for this interaction in Table 4.6 is

Table 4.7: ANOVA for $ln(\sigma)$ of the average corrosion time, conducted to determine the significance that the corrosion time standard deviation has on factors and interactions.

Source	F
A	3.746
B	0.196
C	4.086
D	1.166
A×B	0.303
A×C	0.541
A×D	1.719
B×C	0.477
B×D	**6.038**
C×D	0.005

significantly effected by corrosion time standard deviation. Factor interactions do not typically have large F-ratios, especially those that involve an insignificant factor [47].

Experimental settings in accordance with Tables 4.5, 4.6 and Fig 4.3, batch HJR 12A was produced using the ideal experimental settings. This batch had an average corrosion time of 15.3 ± 5.6 hrs. Although pre-milling of the CI powder (factor D) was not shown to be significant via ANOM or ANOVA, the m_{+1} setting had a slight positive effect (Fig. 4.3), and was included in the NCP to mitigate the potential of agglomerations. Even though agglomerations are not thought to be a high risk in every batch, pre-milling the powder is seen as a preventative measure. Because more than two kilograms of zirconia-coated powder are used to make one slurry, and only 30 grams of powder were used in the corrosion test, there is still some uncertainty that the same mass of powder used in the testing did not allow for adequate testing of particle agglomeration.

4.4 Summary

- Application of a sixteen treatment-condition full-factorial accelerated corrosion test provided the following benefits:
  - Allowed for the testing of four two-level factors
  - The ability to apply one factor to each step of the powder manufacturing process
  - Provided information on the significance of factors and factor interactions
- Process variables were evaluated using an accelerated corrosion test with a quantifiable time of slurry failure
- The optimal coating was obtained by adding zirconium butoxide prior to nitric acid, increasing sol-gel concentration to 60 vol%, and using a 60°C drying temperature
- The accelerated corrosion test showed that in pH 2 dilute glacial acetic acidic environments the NCP MR powder was 3.5x more durable than OCP MR powder, and 150x more durable than uncoated CIP
  - Average time to NCP MR slurry failure: 1074 min.
  - Average time to OCP Mr slurry failure: 300 min.
  - Average time to CIP slurry failure: 7.2 min.

Chapter 5

Procedures for Characterization of MRF Powders

5.1 Introduction

Following completion of the corrosion experiment and implementation of the resulting alterations to the batch production procedure, it became important to develop a reliable method to characterize the differences between the old and new powder compositions. The primary focus was to obtain quantifiable data on the elemental composition of various powders. Of secondary interest is the quantification of free zirconia present in the bulk powder i.e, whether there was enough free ZrO_2 to act as an additional finishing abrasive.

5.2 Separation of MRF Powder Components

In order to both compare many different MR powders, and quantify the concentrations of their components, it became necessary to develop procedures for isolating powder components (e.g. free zirconia) and for identifying the composition of the post-coating supernatant liquids, discussed in Section 3.2. The powders collected using the following methods are referred to as Process [1-4] and abbreviated as ZrP[1-4]. The methods used to collect and isolate these different powder components are discussed in the following sections.

5.2.1 ZrP1: Collection of Free Zirconia

A 15 g sample of MR powder was extracted from the final product of batch 18A (NCP). This powder was milled for 10 min using a mortar and pestle to break up any larger agglomerations and dislodge clumps of zirconia from the coated powder. The milled powder was placed in a 200 mL plastic container and 100 mL of DI water was added. The slurry was then mixed for 4.0 min using an IKA T10 basic high shear mixer [48], shown in Fig 5.1a. This mixed slurry is uniformly black and slightly more viscous than water (Fig. 5.1b). The slurry can rest for several minutes after dispersion before separation is noticeable. Three 2.5 kilogauss magnets (Fig. 5.1c), were evenly spaced around the outside of the container, and used to draw the bulk of the magnetic powder to the sides of the container, leaving any non-magnetic free zirconia in solution in the middle of the container. The majority of the particles consolidate around the magnets

in < 2 sec. After ≈ 2 min it is assumed that even smaller magnetic particles with weaker magnetic potential will have migrated to the sides of the container, leaving coated iron particles clumped around the magnets and a cloudy white solution in the center of the cup (Fig. 5.1d). A 15 mL pipette was used to extract the cloudy white solution and deposit 14.5 mL of the sample into each centrifuge tube.

After the six tubes were filled, the Fisher Scientific Centrific Model 228 centrifuge was set to run for 15 minutes (Fig. 5.1e). Upon completion, the clear supernatant of each tube was pipetted into a waste container. The remaining 0.1 mL of solid particulate was extracted with a 15 mL pipette and deposited into one 2.0 mL glass vial. Approximately 100 mL of DI water was added to the powder, and the slurry was high shear mixed for another 4.0 min.

This process was repeated on the initial 15 g powder sample with three more batches of six tubes, each filled with 14.5 mL of nonmagnetic slurry. The same powder was used for each repetition, with the goal of determining how much free zirconia was present in the initial 15 g mass. The 1.5 mL of wet solids in the 2.0 mL vial was then placed into a vacuum oven at 100°C and exposed to a $525-675$ Torr vacuum in order to evaporate the remaining liquids. The vial was capped and left undisturbed until sample analysis (Fig. 5.1f). The solids collected during this process were used for X-ray diffraction (XRD) measurements, the dry mass of non-magnetic particulate was not recorded.

A similar procedure was executed with 100 g of 31-B (NCP) powder to determine the

(a) The IKA T10 basic high shear mixer used to evenly distribute particles in the slurry and break up any remaining large agglomerations.

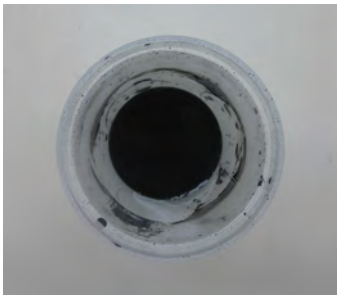

(b) Fifteen grams of zirconia-coated MR powder from batch 18A dispersed in 100 mL of DI water after undergoing high shear mixing for four minutes.

(c) Three 2.5 kilogauss magnets in plastic bags, used to draw the magnetic powder to the sides of the container.

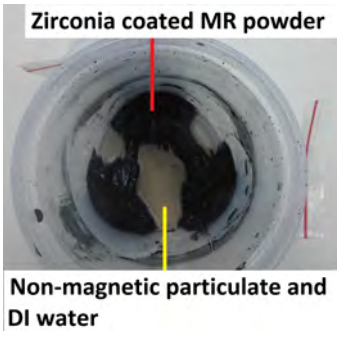

(d) Three 2.5 kilogauss magnets, in small plastic bags, evenly spaced around the base of the cup containing DI water and MR powder. The DI water became cloudy white and was isolated using a 15 mL pipette.

(e) The Fisher Scientific centrifuge with six test tubes prepared for separation.

(f) The resulting quantity of non-magnetic powder collected from six centrifuged vials after the liquid from the slurry had been evaporated in a vacuum oven.

Figure 5.1: Process of gathering free zirconia in MRF powder via magnetic separation.

mass fraction of free ZrO_2 particles in the bulk MR powder. Two iterations of centrifugation were used to collect free zirconia particulate. The wet solids were placed in 20 mL glass sample vials; all excess fluid from the centrifuge tubes were deposited in a 200 mL beaker. Magnetic separation was performed a third time, and the fluid and nonmagnetic particulate was placed in a second 200 mL beaker without undergoing centrifugal separation. Masses of the four empty holding vessels were recorded prior to addition of the slurry. The sample containers were placed in a 95°C convection oven to evaporate the fluid. After 24 hours the fluid had evaporated, and the masses of the vessels with solid particulate were recorded. The MR powder remaining after magnetic separation was kept for later analysis, and labeled as post separation MR powder (PS 31-B).

5.2.2 ZrP2: Collection of Powder from Evaporated Supernatant

Because the NCP used $\sim$ 20% more zirconia sol-gel than the OCP, there is a distinct possibility that any excess zirconia sol-gel could react with itself to form zirconia nanoparticles. To investigate this hypothesis, the supernatant taken from between four and eight batches was collected in a plastic bucket (Fig. 5.2a). Due to the length of time required to make each batch, the solution and particles in this container were several weeks old before the sample was extracted. Using a 250 mL plastic beaker, a 200 mL sample of the supernatant liquid was taken from the top of the container after no additional material had been added for three days (Fig. 5.2b). This sample was placed in the vacuum oven at 100°C and a $525 - 675$ Torr, until the solution had evaporated.

Approximately 1.5 g of gray-white powder was scraped from the beaker and placed in a vial, Figure 5.2c shows the powder before it was transfered to the vial for storage.

(a) Container used to collect supernatant solution from several batches.

(b) A sample of the colored supernatant. Approximately 200 mL of this solution was put into the vacuum oven.

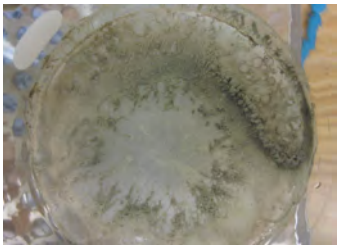

(c) The powder remaining after the supernatant solution had evaporated. This powder was scraped out of the dish and placed into a vial.

Figure 5.2: Procedure for collecting powder from the supernatant solution.

5.2.3 ZrP3: Collection of Particulates in the Supernatant Liquid

Particulate matter was observed in the supernatant liquid container. Because it was not apparent whether this particulate was zirconia-coated MR powder from the wash process described in Subsection 3.2.3 or non-magnetic particulate of an unknown composition, efforts were made to recover the material for analysis. The major portion of particulate resting on the bottom of the supernatant storage container (Fig.5.2a) was removed by siphoning, along with a portion of the supernatant solution (Fig. 5.3a and 5.3b). The container holding the siphoned material was agitated to evenly distribute the particulate before transferring the colloidal solution into six test tubes, each containing 14.5 mL (Fig. 5.3c). The test tubes were centrifuged for 15 min to recover the particulate (Fig. 5.3d). The supernatant was removed by pipetting into a waste vessel. The last

1.0 mL of solution, containing the particulate from each test tube was transfered to a crystallization dish (Fig. 5.3e) and the dish was placed into the vacuum oven at 100°C and $525 - 675$ Torr to evaporate the remaining solution. Approximately 0.1 g of powder was collected from the 87 mL of solution initially placed into the test tubes.

(a) A sample of supernatant solution in a container with some sediment on the bottom.

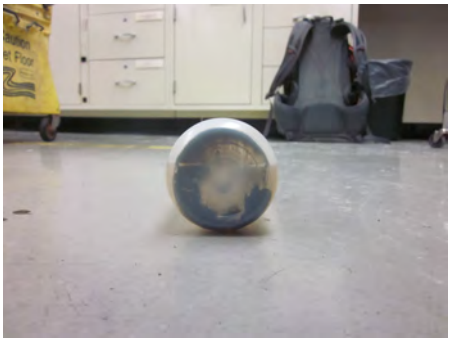

(b) A bottom view of the powder sediment in the Nalgene bottle.

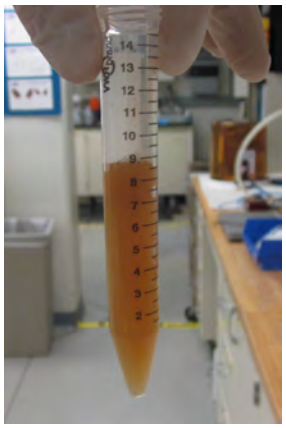

(c) A centrifuge vial partially filled with the supernatant and particulate mixture. Six of these tubes were placed into the centrifuge (Fig. 5.1e), for 15 min.

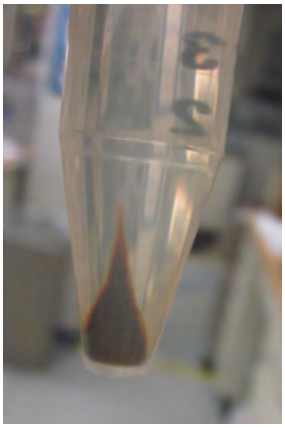

(d) The solution was isolated with a 15 mL pipette and placed into a waste container. The remaining 0.1 mL was used to re-mix the sediment into the solution and was isolated using a 2.0 mL pipet.

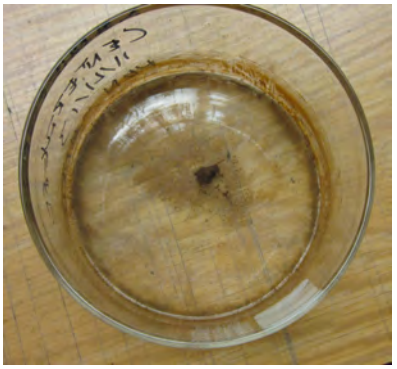

(e) The sediment isolated from the vials shown in Figure 5.3d was placed into a dish and then put in a vacuum oven, at 100°C, $525 - 675$ Torr to evaporate the solution.

Figure 5.3: Procedure for collecting sediment from the supernatant and powder wash process.

5.2.4 ZrP4: Collection of Powder from Calcination of Zirconium Butoxide

Zirconium butoxide was calcinated to obtain a powder with a high concentration of zirconia, to be analyzed with XRD and X-ray fluorescence (XRF). Eighty-nine grams of zirconium butoxide was poured into a 500 mL beaker, with a of mass 169.08 g. This beaker was placed into the convection oven (Fig. 3.4), with the temperature set to 95°C, and convection setting turned on to decrease the time needed for evaporation to occur. The solution was left in the oven over-night. By the next day the solution had evaporated, leaving 10.78 g white powder on the bottom of the beaker. The powder was scrapped out of the beaker into a 10 mL vial.

5.3 Pycnometry of MRF Powders

A Micromeritics Accupyc II 1340 helium gas pycnometer (Fig. 5.4a), was used to determine the density of various MR powders. Prior to measurement, an empty $1.0cm^3$ sample cup was placed on the Sartorius Precision Balance (Fig. 5.4b). Powder free latex gloves were worn when working with the pycnometer and the balance to eliminate contamination from epidermal oils that will reduce instrument precision. The sample cup was filled to $^3/_4$ its volume with the powder sample, and the cup was placed in a vacuum oven at 100°C and $525-675$ Torr for at least one hour to remove moisture. The sample cup was placed in a desiccator and allowed to rest between 15 min - 2 days. The desiccator was kept under 25% humidity. After the powder sample and cup have cooled

(a) Micromeritics Accupyc II 1350 helium gas pycnometer, used for powder density measurements.

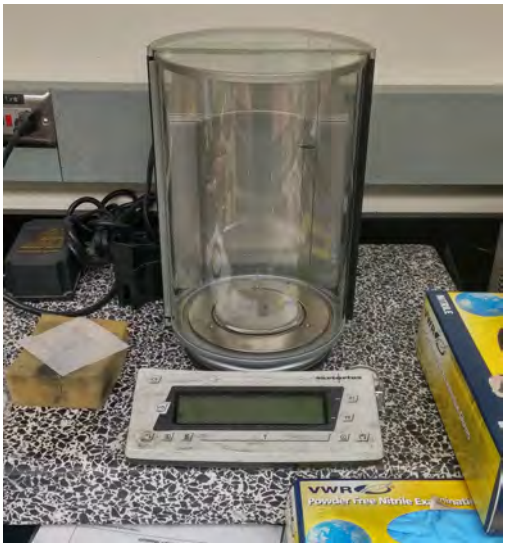

(b) Sartorius Precision Balance.

Figure 5.4: The two instruments used to obtain powder density measurements.

to room temperature, their mass was recorded using the Sartorius Precision Balance. The sample mass, which was input to the Micrometrics software, was obtained by taking the difference between the mass of the filled sample cup and empty sample cup.

Once the mass of the powder sample was been obtained, the sample and cup were transfered to the pycnometer. After at least 10 min of thermal equilibration, the output pressure of the helium regulator was set to $21 - 22$ psi. The measurement parameters included the measurement pressure (19.5 psi), number of purge cycles (20), and number of measurement cycles (25). Increasing the number of purge cycles aided in the stabilization of the powder sample, while increasing the number of measurement cycles improved the precision of results. Once thermal equilibration was reached, the measurement was started. Because the process takes $\approx$ 4 hrs to complete, only two complete

measurements may be obtained in one day.

5.4 X-ray Diffraction Measurements

X-ray diffraction was used to obtain phase and mass fraction information for powder sample components. Table 5.1 shows during which stage of the production samples were collected for testing. These samples were chosen to determine the chemical composition of powders found throughout the production process.

Table 5.1: Samples collected for testing and a brief sample description. The samples involving collection of more concentrated zirconia powders are labeled 'ZrP[1-3]'

Sample	**Description**
CI-HQ (Lot # 03203RS, received on 11/5/2008)	Uncoated CI particles (2.0 µm diameter)
HQ-Zr 3A	A batch of coated particles made on 5/7/13 using the "older coating procedure"
9A	A batch of coated particles made on 10/2013 using the "new coating procedure"
ZrP1: Concentrated Zirconia (from batch 18A, coated using the NCP)	Concentrated zirconia, collected through use of magnetic separation of a MRF powder batch prepared on 11/2013
ZrP2: Supernatant Evaporate	Powder remaining after evaporating the supernatant solution. The supernatant solution was collected from batches created suing the new coating procedure.
ZrP3: Supernatant Particulate	Particles collected from the first step of the wash. The supernatant particulate was collected from batches created using the new coating procedure

A powder sample of the CI-powder was chosen to establish a good background signature for the iron and iron oxides found in most of the samples. This CI-powder sample was taken from the bulk powder storage. The powder sample obtained from batches HQ-Zr 3A (OCP) and 9A (NCP) were prepared utilizing the two different preparation techniques. A significantly higher concentration of zirconia was expected to be found in the zirconia-coated powder collected from batch 9A (made with 60 vol.% zirconium sol-gel, instead of the 40 vol.% sol-gel concentration used in the OCP). The sample containers were shaken for three minutes prior to collection to ensure sample homogeneity.

The amount of free zirconia is believed to play a significant role in the polishing performance of the MR powder. Techniques for free zirconia isolation, described in Subsection 5.2, were used to provide a preliminary estimate of the quantity of free zirconia particles in the powder.

Preliminary XRD scans were taken using the Phillips MPD X-ray Diffractometer in the Mechanical Engineering Department at the University of Rochester. A Cu K_α source was used with an applied voltage of 40kV and current of 30mA, with the beam in line focus. Scans were performed on heat-treated and as-produced samples. The first set of scans was taken with no additional heat treatment. For the second set of scans, each powder was placed in a 700°furnace for 0.5 hours. This heat treatment was performed to induce crystallization of the amorphous zirconia, as no quantitative or semi-quantitative data can be collected on amorphous materials using the Reference Intensity Ratio method to determine mass fraction [49]. The scan settings and maximum sample exposure temperature prior to scanning are displayed in Tables 5.2 and 5.3. All samples were

scanned using both short (2.00 sec) and long (23.00 sec) step times to investigate the effect that step time has on semi-quantitative mass-fraction analysis.

Table 5.2: Scan settings used for powder sample measurements in the Phillips MPD X-ray Diffractometer.

Parameter	**Setting**
Scan Axis	Gonio
Start Position [°2Th.]	10.0000
End Position [°2Th.]	90.0100
Step Size [°2Th.]	0.0300
Scan Step Time [s]	2.000†
Scan Type	Pre-set time
Offset [°2Th.]	0.0000
Divergence Slit Type	Fixed
Divergence Slit Size[°]	0.8059
Specimen Length [mm]	10.00
Receiving Slit Size [mm]	0.5400
Measurement Temperature [°C]	25.00
Anode Material	Cu
Generator Settings	40 kV, 30 mA
Goniometer Radius [mm]	173.00
Dist. Focus-diverg. Slit [mm]	91.00
Incident Beam Monochromator	No
Spinning	No

† Scan times of 10.000s and 23.000s were also used. Scan times of 2.000s are sufficient for survey scans and simple samples. Longer scan times are used when there is a low amount of powder, or higher precision is required.

Table 5.3: Maximum exposure temperature of powder samples during production, extraction process, or heat treatment

Sample	**Composition**	**Initial max. temp. (°C)**	**Heat-treated temp. (°C)**
CI-HQ	Uncoated CI-powder	20	700
HQ-Zr 3A	OCP MR powder	70	700
HJR-9A	NCP MR powder	70	700
ZrP1	Isolated zirconia	100	700
ZrP2	Powder from evaporated supernatant	100	700
ZrP3	Supernatant particulate	100	700

5.5 Scanning Electron Microscopy and Energy Dispersive Spectroscopy

Scanning electron microscopy allows for visualization of differences between: OCP and NCP powder samples, particle size distribution, zirconia coating thickness for particle cross-sections, and free zirconia appearance. The backscatter detector in this instrument highlights regions of varying atomic composition, which is particularly useful in identifying coating thickness. The EDaX detector employs Energy Dispersive Spectroscopy to provide both semi-quantitative mass fraction data and X-ray maps that highlight the location and concentration of elements in the SEM micrograph. With the proper sample preparation, a wide variety of information may be obtained through the use of the SEM.

5.5.1 Epoxy Puck Sample Preparation

In order to expose particle cross-sections, MR powder was mixed with an epoxy and cast into pucks that were then ground and polished. This technique was based on a procedure used by Shorey et. al. for the nanoindentation of CI particles used in MRF [50]. Two different thermosetting epoxy formulations were used: a conductive thermosetting epoxy (ProbeMet produced by Buehler), and a two-part epoxy suitable for use in vacuum environments (Stycast 1266 produced by Emerson & Cuming).

To make the thermosetting epoxy pucks, 6.0 g of a 50:50 mixture of MR powder and epoxy were poured into a cylindrical mold and 10 g of epoxy was added to the top of the powder mixture/epoxy. The mold was placed onto the stage of a pre-heated thermosetting press (Fig. 5.5b), and exposed to a pressure of 29 MPa. The pressure was maintained for three minutes, allowing the epoxy to set. The pressure was released, and the epoxy puck was extracted from the mold. The surface of the puck was ground using the Buehler Belt Surfacer (Fig. 5.5c). The puck was then ground using the Buehler water lubricated grinder (Fig. 5.5d), rotating the part 90°each time a finer grit was used. The part was polished using a motorized pad polisher and 1.0 µm alumina powder and water (Fig. 5.5e). Once scratches were no longer visible, the sample was transfered to another pad polisher and polished with 0.05 µm alumina polishing slurry.

(a) "ProbeMet" conductive thermosetting molding compound used to make the first set of epoxy pucks.

(b) The Buehler thermopress used to form the conductive epoxy pucks.

(c) A Buehler Belt Surfacer used to prepare the pucks for finer grinding and polishing.

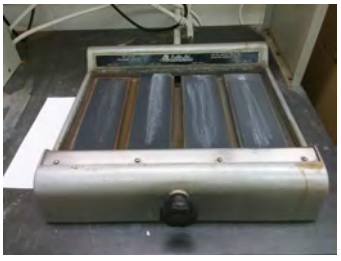

(d) The Buehler water lubricated grinder, with grit sizes of: 240, 320, 400, and 600.

(e) A motorized pad polisher with 1.0 µm alumina powder and water polishing solution, a second pad polisher with 0.05 µm polishing powder was also used.

(f) Four gold sputter coated thermosetting epoxy pucks.

Figure 5.5: Production of Probe Met thermosetting conductive epoxy pucks with embedded MRF powder.

The second epoxy, Stycast 1266 vacuum epoxy, was evaluated as an alternative to the original thermosetting epoxy. This two-part epoxy was selected for its uniform liquid composition, superior performance while under vacuum (minimal outgassing), and lack

of metallic components. The epoxy was mixed at a mass ratio of 100 parts resin to 28 parts hardener. A cylindrical aluminum mold was placed onto an aluminum sample dish. Five grams of epoxy were added to the mold; 2.0 g of powder was mixed into the epoxy and an additional 5.0 g of the epoxy was added to the top of the powder-epoxy mixture. The mold containing the sample was baked in a vacuum oven at 65°C at ≈ 375 Torr for two hours. After the pucks have been removed from the casts, they are ground and polished using a motorized grinding / polishing wheel (Fig. 5.6a).

(a) The motorized grinding and polishing wheel used to polish the Stycast 1266 pucks.

(b) Four polished epoxy pucks, from upper left to lower right: A sputter coated 'blank', HQ-Zr 4 in Stycast 1266 with no sputter coating, sputter coated 31-B, sputter coated HQ-Zr 4.

Figure 5.6: Procedure for making Stycast 1266 vacuum epoxy pucks with embedded MRF powder.

Several pucks were made using the combinations outlined in Table 5.4. A variety of powders were used to highlight the differences between batch production procedures. After polishing, the pucks were ready for SEM preparation, which involves applying a conductive coating to the top surface; these procedures are described in the section below.

Table 5.4: MRF powder and epoxy puck samples, a ✓indicates that an epoxy puck was made using that method.

Powder Sample	**Composition**	**Probe Met Thermosetting Conductive Epoxy**	**Stycast 1266 Vacuum Epoxy**
CI-HQ	Uncoated CI-powder		✔
HQ-Zr 4	OCP MR powder	✔	✔
31-B	NCP MR powder	✔	✔
325 Mesh	OCP MR powder	✔	
325 Mesh	NCP MR powder	✔	

5.5.2 Preparing samples for the SEM

Standard SEM aluminum sample stubs are placed on the counter, and conductive carbon tape was adhered to the surface of the sample stub. Care was taken to avoid touching the surface of the sample, to avoid sample contamination. All samples were coated with gold or carbon to reduce charging on the surface of the samples in the SEM.

5.5.2.1 Gold sputter coating

The prepared sample stub was placed into the bell jar of the "Denton Vacuum Desk II" sputter coater in the URnano facility at the University of Rochester (Fig. 5.7a) . The system was turned on, the "Sputter" button was pressed twice, and the sample chamber was pumped down to 50 mTorr, using a rotary pump. The regulator for the argon line was opened until the chamber pressure reached $\approx$ 500 mTorr. The Denton Vacuum Desk II argon line needle valve was closed, and the system was pumped down to 100 mTorr. This process was repeated two more times to remove any remaining air in the chamber

and ensure a predominantly argon atmosphere. The final pressure in the bell jar was 100 mTorr. The sputtering current in the chamber was adjusted to 15 mA, a coating time of 90 seconds was set, and the 'Start' button was depressed to start the coating run. Approximately 90 Å of gold was deposited in 90 seconds by this process. The vacuum was shut off, and the sample was removed from the chamber. A thin layer of conductive carbon paint was applied to the interface between the sample and the sample stub, ensuring that the sample was properly grounded to minimize charge collection during imaging.

5.5.2.2 Carbon coating

Several samples were evaporatively coated with carbon, because gold has a similar excitation energy to zirconia when analyzed by EDS. Coating samples with carbon allows for higher imaging resolution due to its smaller atomic size when compared to gold. The Ladd Carbon Evaporator is shown in Fig. 5.7b; operational procedures for the evaporator are displayed in Figure 5.8.

(a) Denton Desk II vacuum sputter coating instrument, used to gold sputter coat various samples for the SEM.

(b) Ladd carbon evaporator, used to carbon coat various samples for the SEM.

Figure 5.7: Two coating instruments used to prepare samples for the SEM

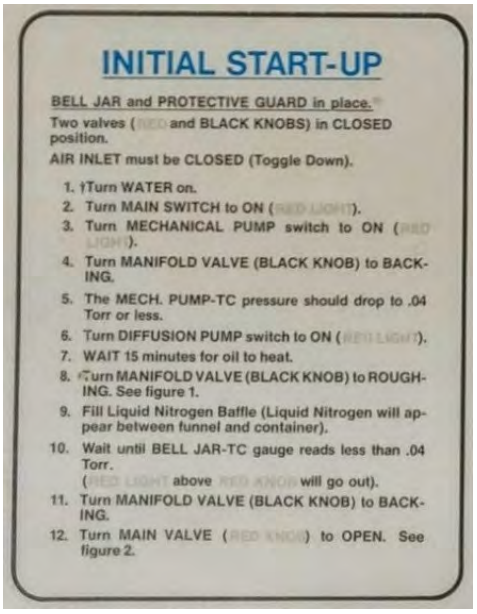

INITIAL START-UP

BELL JAR and PROTECTIVE GUARD in place.

Two valves (and BLACK KNOBS) in CLOSED position.

AIR INLET must be CLOSED (Toggle Down).

1. †Turn WATER on.
2. Turn MAIN SWITCH to ON ( ).
3. Turn MECHANICAL PUMP switch to ON ( ).
4. Turn MANIFOLD VALVE (BLACK KNOB) to BACKING.
5. The MECH. PUMP-TC pressure should drop to .04 Torr or less.
6. Turn DIFFUSION PUMP switch to ON ( ).
7. WAIT 15 minutes for oil to heat.
8. Turn MANIFOLD VALVE (BLACK KNOB) to ROUGHING. See figure 1.
9. Fill Liquid Nitrogen Baffle (Liquid Nitrogen will appear between funnel and container).
10. Wait until BELL JAR-TC gauge reads less than .04 Torr.
    (above will go out).
11. Turn MANIFOLD VALVE (BLACK KNOB) to BACKING.
12. Turn MAIN VALVE ( ) to OPEN. See figure 2.

(a) Instructions for the start-up of the Lad evaporator.

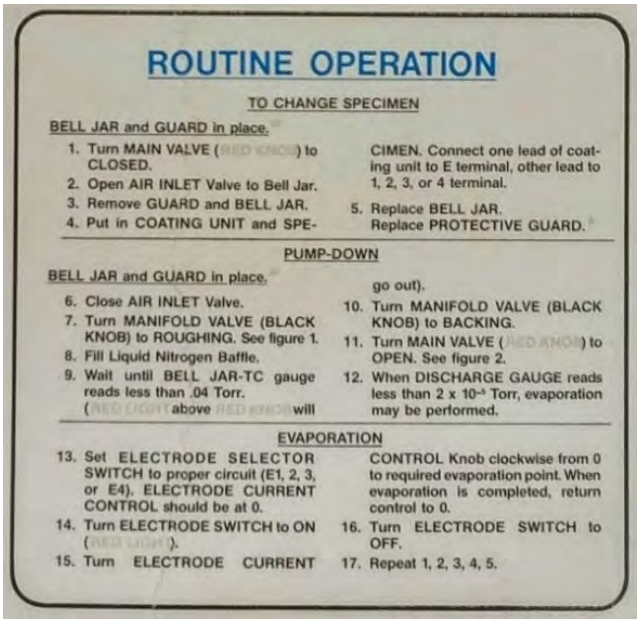

ROUTINE OPERATION

TO CHANGE SPECIMEN

BELL JAR and GUARD in place.

1. Turn MAIN VALVE ( ) to CLOSED.
2. Open AIR INLET Valve to Bell Jar.
3. Remove GUARD and BELL JAR.
4. Put in COATING UNIT and SPECIMEN. Connect one lead of coating unit to E terminal, other lead to 1, 2, 3, or 4 terminal.
5. Replace BELL JAR. Replace PROTECTIVE GUARD.

PUMP-DOWN

BELL JAR and GUARD in place.

6. Close AIR INLET Valve.
7. Turn MANIFOLD VALVE (BLACK KNOB) to ROUGHING. See figure 1.
8. Fill Liquid Nitrogen Baffle.
9. Wait until BELL JAR-TC gauge reads less than .04 Torr.
   (above will go out).
10. Turn MANIFOLD VALVE (BLACK KNOB) to BACKING.
11. Turn MAIN VALVE ( ) to OPEN. See figure 2.
12. When DISCHARGE GAUGE reads less than 2 x 10^{-4} Torr, evaporation may be performed.

EVAPORATION

13. Set ELECTRODE SELECTOR SWITCH to proper circuit (E1, 2, 3, or E4). ELECTRODE CURRENT CONTROL should be at 0.
14. Turn ELECTRODE SWITCH to ON ( ).
15. Turn ELECTRODE CURRENT CONTROL Knob clockwise from 0 to required evaporation point. When evaporation is completed, return control to 0.
16. Turn ELECTRODE SWITCH to OFF.
17. Repeat 1, 2, 3, 4, 5.

(b) Instructions for the operation of the Lad evaporator.

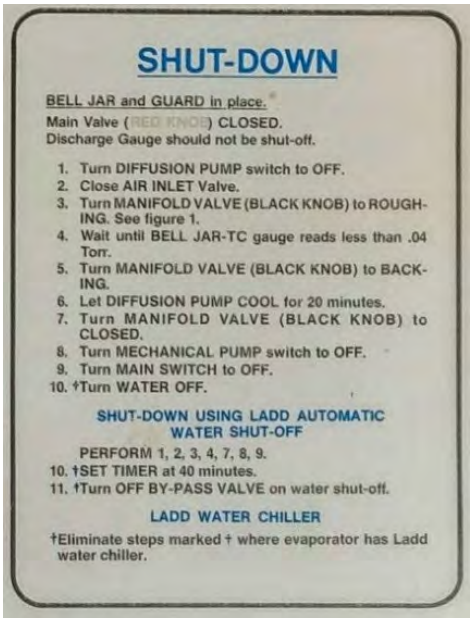

SHUT-DOWN

BELL JAR and GUARD in place.

Main Valve ( ) CLOSED.

Discharge Gauge should not be shut-off.

1. Turn DIFFUSION PUMP switch to OFF.
2. Close AIR INLET Valve.
3. Turn MANIFOLD VALVE (BLACK KNOB) to ROUGHING. See figure 1.
4. Wait until BELL JAR-TC gauge reads less than .04 Torr.
5. Turn MANIFOLD VALVE (BLACK KNOB) to BACKING.
6. Let DIFFUSION PUMP COOL for 20 minutes.
7. Turn MANIFOLD VALVE (BLACK KNOB) to CLOSED.
8. Turn MECHANICAL PUMP switch to OFF.
9. Turn MAIN SWITCH to OFF.
10. †Turn WATER OFF.

SHUT-DOWN USING LADD AUTOMATIC WATER SHUT-OFF

PERFORM 1, 2, 3, 4, 7, 8, 9.

10. †SET TIMER at 40 minutes.
11. †Turn OFF BY-PASS VALVE on water shut-off.

LADD WATER CHILLER

†Eliminate steps marked † where evaporator has Ladd water chiller.

(c) Instructions for the shut-down of the Lad evaporator.

Figure 5.8: Operation instructions for the Lad evaporator.

5.5.3 SEM Techniques

The samples were brought into the SEM lab and loaded onto the sample holder. The 'sample loading' instructions were read carefully before loading the sample holder into the SEM imaging chamber. Three SEM imaging modes were utilized: the SE2 secondary electron detector, the InLense secondary electron detector, and the Backscatter Detector (BSD). Semi-quantitative mass fraction data and X-ray maps were obtained using the EDaX EDS X-ray spectrometer.

Switching between the SE2 and InLense detector is accomplished via software control on a computer workstation. The focal point is first obtained using the SE2 detector; the InLense detector can then be used if required. The working distance and acceleration voltage are first set, and then the brightness and contrast are adjusted before finding the focal point. A typical scan speed for focus and sample location was 2; the scan speed was set to 4 during image capture.

Collection of micrographs using the BSD requires the detector to be moved directly under the beam column from its normally retracted position. The highest point on the sample stage was set at a working distance of greater than 10 mm to avoid collision of the detector with the samples or the stage. The BSD was inserted into the chamber from the rear of the SEM. The Backscatter Detector was selected in the software for focusing and micrograph collection. A substantial difference in sample height prior to moving or rotating the sample stage was noted, as short working distances improve the clarity of BSD micrographs. Because BSD registers primary electrons, areas of

higher average atomic number will appear brighter on the screen, therefore iron will appear brighter than zirconia or iron oxide; increasing acceleration voltage will further accentuate differences.

5.6 X-ray Photoelectron Spectroscopy Measurements

X-ray Photolectron Spectroscopy (XPS) is a quantitative surface measurement technique. When a monochromatic Al K_α source with an energy of 1486.6eV is used, surface composition from depths of $3-30$ nm can be analyzed [51]. This measurement technique was adopted for the measurement of MR powder coating thickness. Several MR powder samples (Table 5.5) were adhered to aluminum sample stubs with carbon tape and sent to the Cornell Center for Materials Research (CCMR) for analysis.

Additional MR powder samples (Table 5.5) were affixed with clear adhesive to a copper base layer and measured at the URnano XPS facility in Gavett Hall at the University of Rochester. To minimize sample contamination, nitrile gloves were worn when affixing samples to the XPS sample stage. Following standard operating procedures [52], the sample stage was loaded into the Kratos Axis Ultra XPS. All samplers were exposed to a survey scan (300 - 1,500 eV), followed by multi-pass region of interest (ROI) scans for: Fe 2p (745 - 785 eV), Zr d3 (1,300 - 1312 eV), and O 1s (944 - 962 eV). The data was exported to Casa XPS software for analysis [53].

Table 5.5: Samples tested using X-ray Photoelectron Spectroscopy. Sample preparation designates either a powder sample being placed on the stage, or the sample embedded in an epoxy puck.

Powder Sample	Composition	Sample Testing Location	Test Date
ZrP1	Free zirconia* powder	CCMR†	11/22/13
18A	New coating procedure	CCMR	11/22/13
PS 18A	Powder remaining after ZrP1	CCMR	11/22/13
ZrP1	Free zirconia	URnano†	4/2/14
ZrP2	Supernatant Particulate§	URnano	4/2/14
325-OCP	Old coating procedure	URnano	4/2/14
325-NCP	New coating procedure	URnano	4/2/14
HQ-Zr 4	Old coating procedure	URnano	4/2/14
31-B	New coating procedure	URnano	4/2/14
PS 31-B	Powder remaining after ZrP1	URnano	4/2/14
31-B	New coating procedure	URnano	7/7/14
HQ-Zr 4	Old coating procedure	URnano	7/7/14
Blank:	Stycast puck	URnano	7/7/14

*: See Subsection 5.2.1 for more information on this method of isolating zirconia from the bulk powder
†: Cornell Center for Materials Research
‡: University of Rochester integrated nanosystems center
§: See Subsection 5.2.3 for more information on this method of collecting zirconia from the supernatant
/: Remaining powder after zirconia separation technique, ZrP1.

5.7 Analyzing Particle Size Distribution of MRF Powder

Particle size-distribution was accomplished with the Acoustosizer IIs [54] by measuring particle size and zeta potential in a colloidal dispersion. A 5 wt% MRF slurry was created by adding 10 g of MR powder to 190 g of 0.01 M KNO_3; the potassium nitrate solution was used to stabilize the slurry by increasing its ionic strength [55]. The IKA T10 high-shear mixer was used to homogenize the slurry prior to analysis using the Acoustosizer IIs. To minimize settling of the dispersion, the stir-rod was set to

350 RPM with a pumping speed of 2.5 selected, from the analog control panel. Five milliliters of the surfactant Darvan *C surfactant was added to the slurry to improve stability. Approximately 2 mL of 2 M NaOH was added to shift the slurry from the IEP (pH 6.5) to pH 13. The dispersion was allowed to stabilize for five minutes. The density, concentration, and dielectric constant of the MR powder sample was input to the Colloidal Dynamics software, the ESA measurement mode was selected, and data collection was initiated. Each slurry was measured three times to produce a standard deviation for the particle size distribution results.

5.8 Corrosion Rate Analysis with pH Monitoring

The variance in corrosion resistance of NCP MR powders was determined using a pH-monitored corrosion test. Two improvements were introduced to the procedure outlined in Subsection 3.3.3. Slurry pH was recorded once per minute, allowing for onset of corrosion to be quantified by the change of pH rather than relying on the observation of the time when foaming begins in the slurry. Due to the increased corrosion resistance of the NCP MR powders (HJR 12A in Table 4.7), sample containers were covered with Parafilm to mitigate slurry evaporation (Fig. 4.2).

Prior to the start of the corrosion test, pH probes procured from Vernier [56] containing a USB interface wire, were connected to a laboratory computer containing Logger Lite Software [57]. The measurement interval was set to once per minute. The pH $\approx$ 2.5, 10 vol% MR powder slurries were placed on the stir-plate that was set to 350 RPM.

The pH probes were placed in the slurries and the beakers were covered with parafilm to minimize the evaporation rate. After this initial setup, the corrosion experiment was left unattended until the following day, when the collected pH vs. time data was exported to Microsoft Excel for analysis.

5.9 X-ray Fluorescence Measurements

X-ray Fluorescence data on sample composition was obtained using a Bruker Tracer III-V hand-held XRF instrument. The instrument was placed into the stand, shown in Figure 5.9a below. Power to the instruement is activated using a key as a safety precaution due to the X-ray source (Fig. 5.9b). Filter selection depends on the analyzed material; each filter requires a specific current and operating voltage. For analysis of iron and zirconium, the green filter (12.0mm Al, 1.0mm Ti, 6.0mm Cu) was selected and loaded into the instrument. After connecting the instrument to a computer and turning the instrument and computer on, the X-ray tube settings were updated for measurements with the green filter (40kV, and 43 μA); Fig. 5.9c shows the instrument settings used for the analysis .

Several scans of potential sample holders were collected to determine which holder produced the lowest background noise signature. The sample holders evaluated included a small plastic sample dish, Parafilm, printer paper, and the coated paper backing of the Parafilm. The Parafilm backing made the lowest background noise and was selected

as the sample holder. Figure 5.9d displays a powder sample, obtained from the calcination of zirconium butoxide, in place on the instrument ready for measurement. All samples were measured for 180 seconds. Efforts were made to keep the sample size consistent, although for some specimens there was not enough powder available. Data was collected using the S1PXRF program, and exported to Bruker's ARTAX software for further analysis.

(a) Bruker Tracer III-V hand-held X-ray Fluorescence instrument resting on a stand.

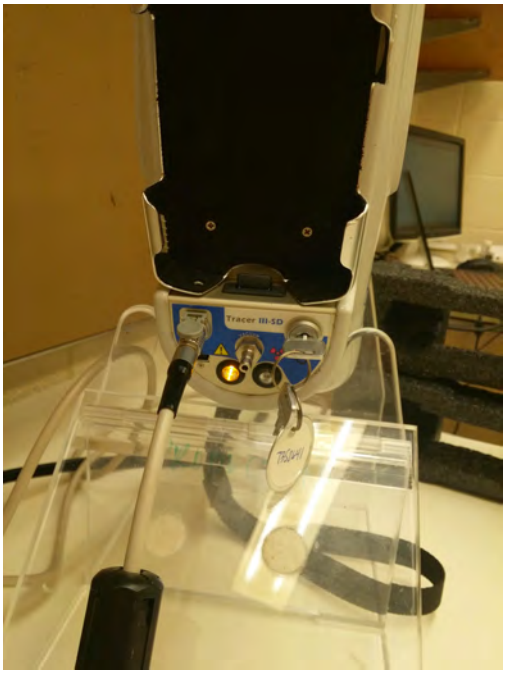

(b) The instruments power key is in the 'ON' position, indicated by the yellow LED. The X-ray source is not active, shown by the lack of illumination in the second LED.

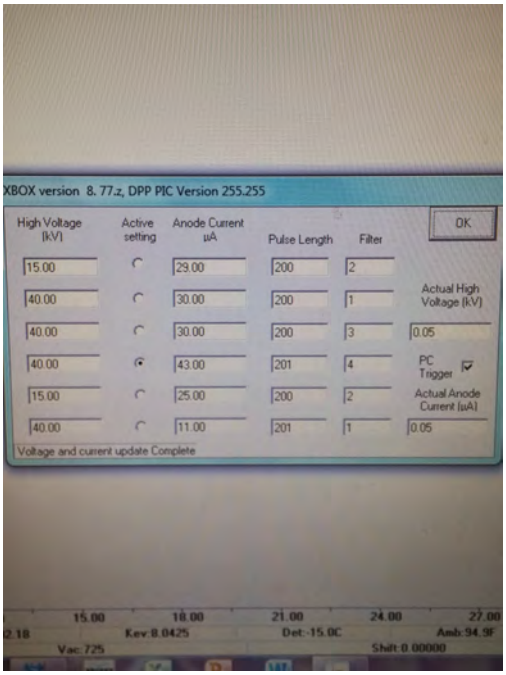

(c) GUI of the selection of the appropriate filter, beam current, and beam voltage settings.

(d) Evaporated zirconium solution gel powder sample resting on wax-paper, ready for measurement. Eraser provided for scale.

Figure 5.9: Tracer III-V XRF instrument setup and sample measurement

5.10 Summary

- MR powder samples were analyzed using a variety of analytical X-ray techniques and measurement of physical properties.
- A variety of powder samples were analyzed to better characterize the MR particles :
  - CIP: carbonyl iron powder.
  - OCP: MR powder manufactured using the old coating procedure.
  - NCP: MR powder manufactured using the new coating procedure.
  - ZrP1: free zirconia collected from NCP MR powder using magnetic isolation.
- A magnetic separation procedure was developed to isolate free zirconia nanoparticles from the bulk MR powder.
  - This procedure was implemented to quantify the mass fraction of zirconia nanoparticles in the bulk powder.
  - ZrP1 powder samples were measured with various analytical X-ray techniques to determine its purity.
- Sample preparation for XRD measurements was minimal. Powders were either measured with no alteration, or heat treated for 30 minutes at 700 °C, however, scans took 7.4 hours to complete.
  - Long scan times limited the number of measurements, making it impossible to develop a statistically significant set of data to be used for future comparison.

- Sample preparation for XPS measurements was minimal. A thin layer of powder was adhered to conductive adhesive affixed to the sample stage:
  - Measurement of eight powder samples took ∼8 hrs.
  - Long scan times made it impossible to develop a statistically significant set of data.
- No sample preparation was required for powders measured using XRF, which enabled the collection of large sets of data, sufficient for statistical analysis.
  - Sample measurement using XRF took 3 min, which is > 150x faster than XRD and XPS, and ∼ 0.5x faster than EDS .
- Samples measured using EDS and SEM required either a gold or carbon coating:
  - The evaporative carbon coating process took ∼1 hr.
  - The gold sputter coating process took ∼15 min.
  - Including the time required for sample preparation, EDS scans of eight samples took ∼3 hrs.
- Imaging of MR powder surface morphology with SEM was simple, as the two secondary electron detectors (InLens and SE2) were sufficient to characterize the particle surfaces, and the same samples measured using EDS were imaged using SEM.
- Imaging of MR powder cross-sections was labor intensive. The most successful sample preparation was accomplished by:

  - Embedding and drying powder samples in Stycast 1266 vacuum epoxy.
  - Grinding and polishing epoxy puck surfaces using a motorized grinding / polishing wheel.
  - Coating the pucks using evaporative carbon coating and loading the samples into the SEM for analysis using the InLens and BSD detectors.

- Preparation of samples for density measurements was labor intensive, requiring a multi-step drying procedure lasting ∼1hr.
- Density measurements took ∼3 hrs. to complete, but required no oversight after the first 0.5 hr.
- Measurement of particle size distribution using the Acoustosizer IIs was labor intensive, requiring calibration of the pH probe and ESA sensor before each use. Additionally, the system needed to be thoroughly cleaned prior to measuring a new powder sample.
- Introducing pH probes to the accelerated corrosion experiment significantly simplified the procedure used for the 16TC-FF accelerated corrosion test by eliminating the need for documenting corrosion times with photographs.

Chapter 6

Experimental Results

6.1 Introduction

This chapter will cover a variety of methods used to obtain more detailed information about powder characteristics. Three different areas were explored: elemental analysis, imaging , and measurements of physical parameters. Various techniques were employed for each method. Elemental analysis was performed with a wide variety of X-ray excitation techniques. Scanning electron microscopy was used to collect micrographs from a wide variety of powder samples and exposed powder cross-sections, providing information on: particle size distribution, surface characteristics, and zirconia coating thickness. Physical parameters, including density and particle size distribution, were analyzed through the application of gas pycnometry, and colloidal dynamics. Through a

combination of these techniques, a more complete understanding of zirconia-coated MR powders was achieved.

6.2 Elemental Analysis

A high priority was placed on producing a method to accurately determine the atomic composition of various MR powders, particularly after the alterations to the production method, described in Section 4.2 had gone into effect. This section will cover results collected using: X-ray Diffraction (XRD), Energy Dispersive Spectroscopy (EDS), X-ray Mapping (XRM), X-ray Photoelectron Spectroscopy (XPS), and X-ray Fluorescence (XRF).

6.2.1 X-ray Diffraction

The data from all XRD scans was analyzed using the X'Pert HighScore software [49]. To obtain accurate peak matches, background noise was filtered out and $K_{\alpha 2}$ peaks were removed before the peak search was executed. The complex peak patterns of the high temperature scans often required use of a variety of peak search functions, including element and compound filtering. Some limitations of this method are also addressed, such as the need for all matched scans to have Reference Intensity Ratio (RIR) information. Use of peak shift, an analysis option that adjusts the position (2θ) of the matched compound to more closely match the measured peak positions, can introduce significant variability in semi-quantitative mass fraction results.

The results of scans performed on as-produced powders are shown in Figures 6.1 – 6.8. Each figure is divided into three parts: (1) the intensity vs. 2θ plots; (2) identified phase plot: and (3) a results table including the semi-quantitative mass fraction. The left hand plots display the diffraction intensity (in number of counts) vs. 2θ. The red line displays the collected data, while the colored vertical lines outlined in gray display the position and intensity of the matched compound. Stick plots display the peak location and intensity of the collected data (located at the top in red) and the matched data (located below). Additional information is displayed in the results table. The match score indicates how close the matched peaks compare to the measured data in terms of intensity and 2θ on a scale of 1-100%; the compound name and chemical formula are also included. The RIR score is used to calculate the semi-quantitative mass fraction. It is necessary that each match has a RIR to obtain semi-quantitative data. Not all matches in the database have a RIR. The scale factor adjusts the matched pattern intensity to the measured data, which will vary with differences in sample preparation, scan time, and complexity of the sample. Not all of this information is displayed in each results table; however, the most important information is the semi-quantitative mass fraction. Significant effort was spent on finding the matches that produced the best scores. The resulting diffraction patterns may vary slightly, resulting in two different samples matching the same material with slightly different diffraction patterns. Examples can be seen in Fig. 6.2 and Fig. 6.6; both have the same semi-quantitative % of iron and magnetite, but Fig. 6.2 matched with magnetite and Fig. 6.6 matched with iron oxide. Another influencing factor is the order in which the matching patterns are selected, which can

change the list of secondary matches.

Although it was known that no crystalline zirconia would show up in the low temperature scans, they did provide a good idea of the non-amorphous mass fractions of materials in the powder. These values are indicated in the column labeled SemiQuant[%]. These scans also provided a baseline for comparison.

The scan of the untreated ≈ 2.0 µm CI produced very good results. Peaks were distinct and there was a small number of background counts. As expected, iron was the only match at 100% in Fig. 6.1. This measurement used the short scan setting, and took ~ 1.5 hrs. The same settings were used for all remaining powder samples. Powder 3A (Fig. 6.2) made using the old coating procedure showed non-amorphous components of iron (57%) and magnetite (Fe2+Fe3+2O4 @ 43%). Powder 9A (Fig. 6.4), created with the new coating procedure, showed the same composition of 57% iron and 43% iron oxide, which confirmed the expected result. The low temperature scan of concentrated zirconia collected via ZrP1 did require a longer scan time ($\sim$ 17 hrs). This scan was the only one to show a broad amorphous peak, which is an indication that this powder has high concentrations of amorphous zironia. The only crystalline match from this low temperature synthesis process was magnetite (Fig. 6.6), indicating that larger CI particles were successfully separated and that only smaller, fully oxidized iron particles remained attached to (or surrounded by) the zirconia. This viewpoint agrees with the hypothesis that the structure of the zirconia coated MR particles have a zirconia outer layer, with an iron oxide underlayer covering an iron core [4]. A powder sample from ZrP3 had high amounts of background noise and only a weak set of peaks (Fig. 6.8);

however, due to the lack of a distinct amorphous signature, this sample was not re-scanned with a larger step time. Peak matching for this sample yielded three iron oxide forms: magnetite (Fe_3O_4, 11%); burnt ochre (Fe_2O_3, 22%); and magnetite, Fe_2O_3, 66%). Although burnt ochre and magnetite have the same chemical formula, they have different peak structures, indicating the presence of a variety of iron oxides in the sample. The presence of remaining unoxidized iron is surprising, considering that the particles remained in the aqueous supernatant solution for several weeks. The scan of the ZrP2 powder (Fig. 6.7) did not display any signs of amorphous materials. The peaks were matched with nitrammite $(NH_4)(NO_3)$, which highlights another issue with the peak matching algorithm; $(NH_4)(NO_3)$ is actually ammonium nitrate.

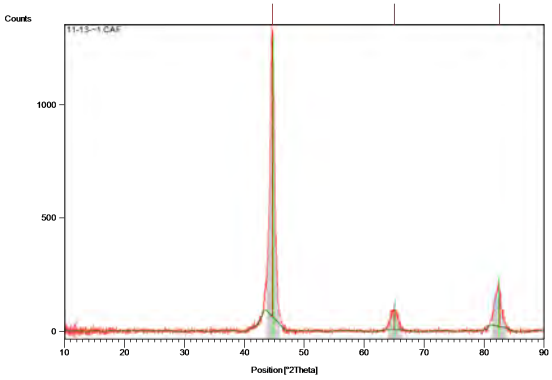

(a) Intensity vs. 2θ Plot

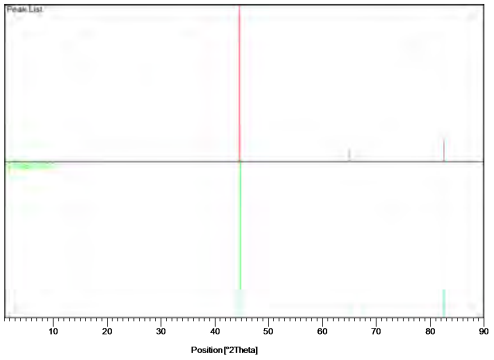

(b) Identified Phase Plot

No.	Ref. Code	Score	Compound Name	Chemical Formula	RIR	SemiQuant [%]	Scale Factor
1	01-087-0722	95	Iron	Fe	10.760	100	0.910

(c) semi-quantitative mass fraction data

Figure 6.1: Carbonyl Iron XRD scan results with a maximum synthesis temperature of 20°C and a 1.48 hour scan time.

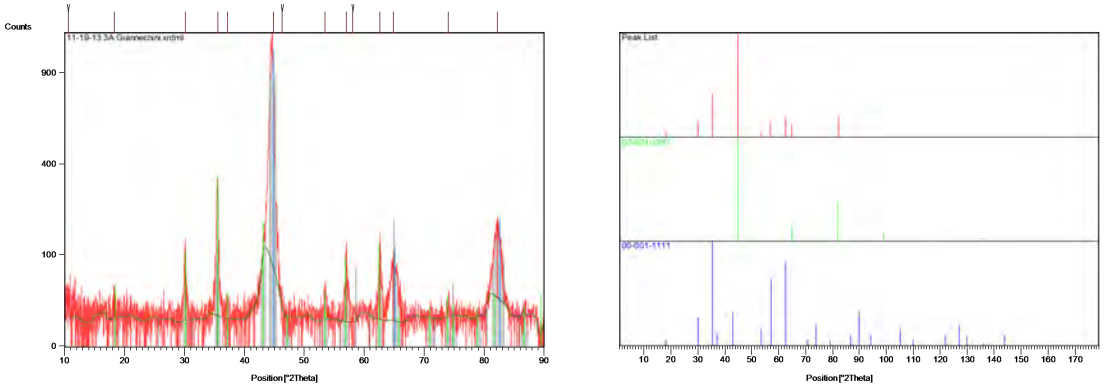

(a) Intensity vs. 2θ Plot (b) Identified Phase Plot

No.	Compound Name	Chemical Formula	RIR	SemiQuant [%]	Scale Factor	Displacement [°2Th.]
1	Magnetite	Fe2.957 O4	4.870	43	0.287	0.178
2	Iron	Fe	10.760	57	0.831	0.011

(c) semi-quantitative mass fraction data

Figure 6.2: MR powder sample scan results from batch HJR 3A (made using the old coating procedure) with a maximum synthesis temperature of 70°C and a 1.48 hour scan time.

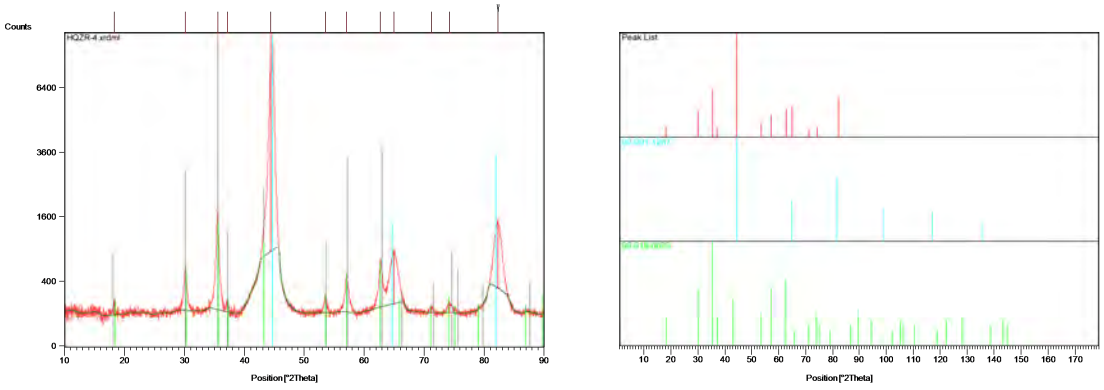

(a) Intensity vs. 2θ Plot (b) Identified Phase Plot

No.	Visible	Score	Compound Name	Chemical Formula	RIR	SemiQuant [%]	Scale Factor	Ref. Code	Displacement [°2Th.]
1	☑	60	Magnetite, syn	Fe +2 Fe2 +3 O4	4.900	24	0.140	00-019-0629	0.150
2	☑	63	Iron	Fe	10.760	76	0.976	01-087-0722	-0.326

(c) semi-quantitative mass fraction data

Figure 6.3: MR powder sample scan results from a long duration scan of batch HQ-Zr 4 (made using the old coating procedure) with a maximum synthesis temperature of 70°C and a 7.41 hour scan time.

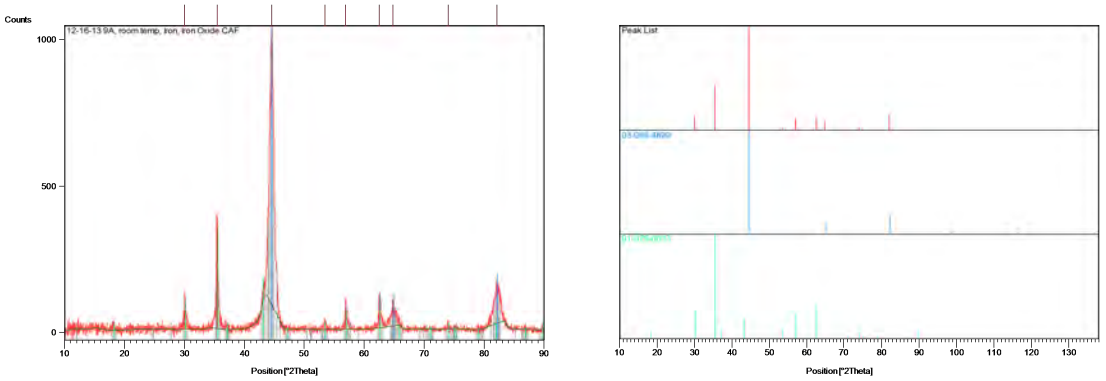

(a) Intensity vs. 2θ Plot (b) Identified Phase Plot

No.	Score	Compound Name	Chemical Formula	RIR	SemiQuant [%]	Scale Factor	Displacement
1	57	Iron	Fe	10.770	57	0.932	
2	55	Iron Oxide	Fe3 O4	5.030	43	0.326	

(c) semi-quantitative mass fraction data

Figure 6.4: MR powder sample scan results from batch HJR 9A (Table 4.1, pg. 41) with a maximum synthesis temperature of 70°C and a 1.48 hour scan time.

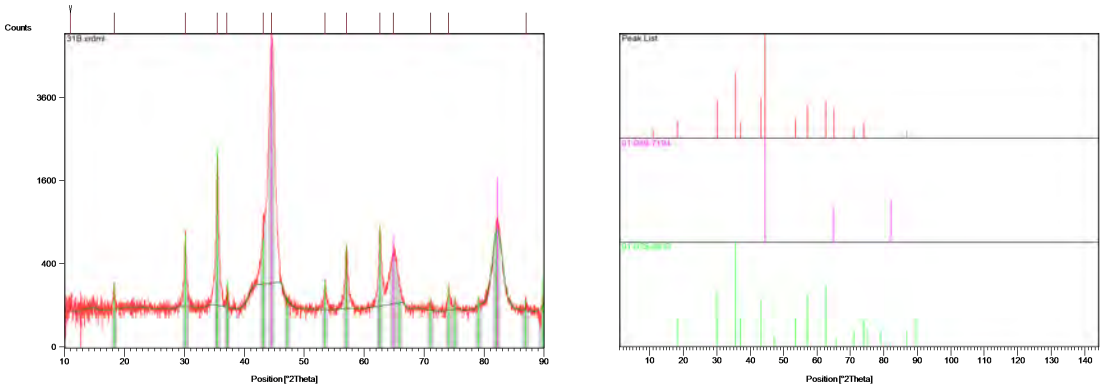

(a) Intensity vs. 2θ Plot (b) Identified Phase Plot

No.	Visible	Score	Compound Name	Chemical Formula	RIR	SemiQuant [%]	Scale Factor	Ref. Code	Displacement [°2Th.]
1	☑	50	Iron	Fe	10.770	53	0.930	01-089-7194	-0.170
2	☑	82	Iron Oxide	Fe3 O4	5.030	47	0.387	01-075-0033	-0.011

(c) semi-quantitative mass fraction data

Figure 6.5: MR powder sample scan results from a long duration scan of batch 31B (made using the new coating procedure) with a maximum synthesis temperature of 70°C and a 7.41 hour scan time.

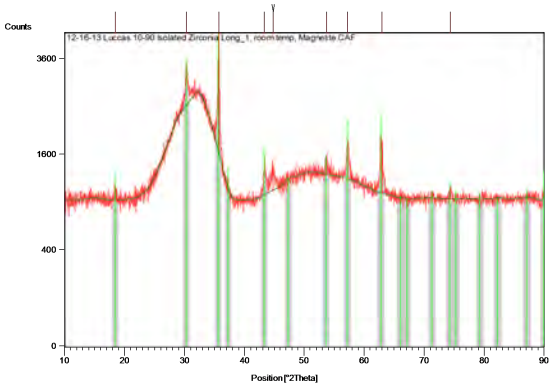

(a) Intensity vs. 2θ Plot

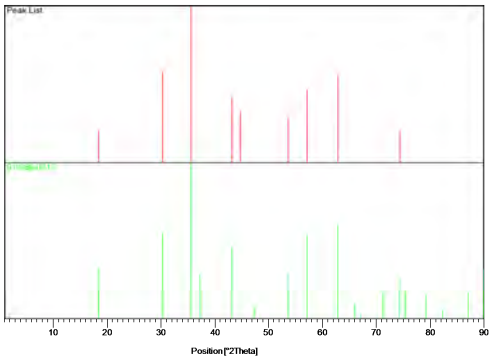

(b) Identified Phase Plot

No.	Visible	Ref. Code	Score	Compound Name	Chemical Formula	RIR	SemiQuant [%]
1	✔	01-088-0315	73	Magnetite, syn	Fe3 O4	5.100	100

(c) semi-quantitative mass fraction data

Figure 6.6: XRD scan results from isolated zirconia, (ZrP1 from Table 5.1, pg. 64) with a maximum synthesis temperature of 100°C and a 17.04 hour scan time.

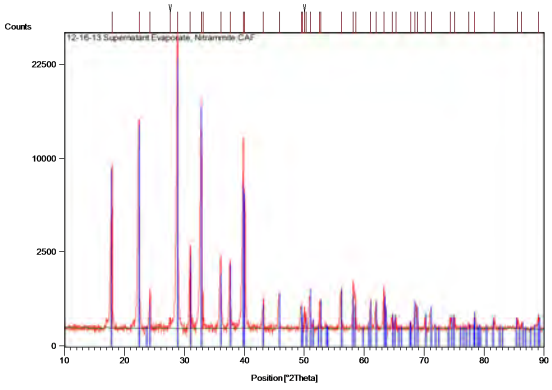

(a) Intensity vs. 2θ Plot

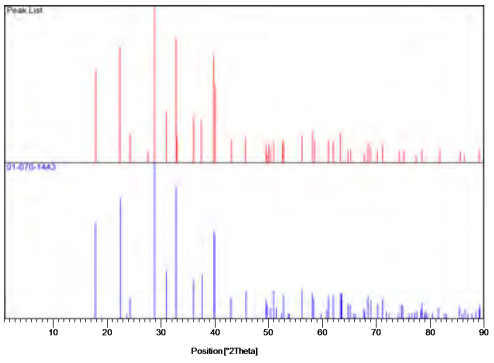

(b) Identified Phase Plot

No.	Ref. Code	Score	Compound Name	Chemical Formula	RIR	SemiQuant [%]	Scale Factor
1	01-070-1443	79	Nitrammite, syn	N H4 N O3	1.150	100	0.842

(c) semi-quantitative mass fraction data

Figure 6.7: XRD scan results from the supernatant evaporate (ZrP2 from Table 5.1) with a maximum synthesis temperature of 100°C and 1.48 hour scan time.

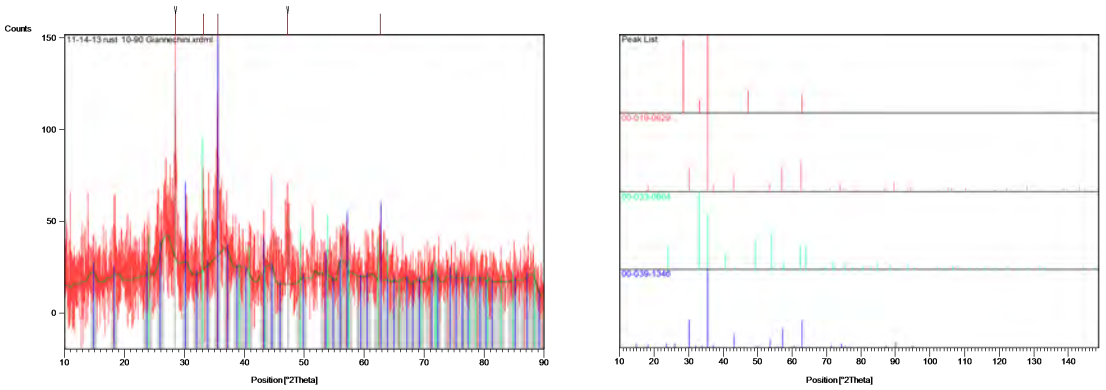

(a) Intensity vs. 2θ Plot (b) Identified Phase Plot

No.	Score	Compound Name	Chemical Formula	RIR	SemiQuant [%]
1	19	Magnetite, syn	Fe +2 Fe2 +3 O4	4.900	11
2	12	burnt ochre	Fe2 O3	2.400	22
3	23	Maghemite-\ITC\RG, sy	Fe2 O3	1.400	66

(c) semi-quantitative mass fraction data

Figure 6.8: XRD scan results from the supernatant particulate (Zr P3 from Table 5.1) with a maximum synthesis temperature of 100°C and 1.48 hour scan time.

The intensity vs. 2θ plots, identified phase plot and semi-quantitative mass fraction of the components for the scans of powders heat treated at 700°C for 30 minutes are shown in Figures 6.9 – 6.15. The carbonyl iron powder (Fig 6.9) completely oxidized after 30 minutes in the 700°C furnace and had begun to melt, forming several $\approx 3.0 - 7.0$ mm agglomerates which were removed from the powder. Four different phases of iron oxide were identified from the diffraction patterns: hematite (Fe_2O_3, 42%); wuestite ($Fe_{0.925}O$, 25%); magnetite (Fe_3O_4, 23%); and iron oxide (FeO, 10%).

Magnetorheological powders made using both the old (3A – Fig 6.10) and new (9A – Fig 6.12) coating procedures contained zirconium oxide, with the new coating procedure showing almost twice the amount of zirconia in the bulk powder with pattern shifting

enabled. The mass fraction of zirconia in both powders was relatively low ($< 10\%$); the remaining mass was composed of iron oxide. Sample from MR powder batch 3A is composed of: iron oxide (Fe_2O_3, 95%) and baddeleyite (ZrO_2, 4%). Sample from MR powder batch 9A contained iron oxide (Fe_2O_3, 93%) and baddeleyite (ZrO_2, 7%), nearly doubling the mass fraction of zirconia measured in batch 3A.

A long scan time was used for the ZrP1 measurement (Fig 6.14), with the three highest peaks registering over 10,000 counts. The magnetic separation process worked well, with the composition of the ZrP1 powder assaying as being zirconium oxide ($ZrO_{1.95}$, 85%) and iron oxide (Fe_2O_3, 15%). The powder sample from ZrP3 (Fig 6.15) had an increased mass fraction of zirconia compared to the coated MR powders. The ZrP2 powder sample (comprised of ammonium nitrate) completely evaporated when it was left in the 700 °C furnace for one-half hour.

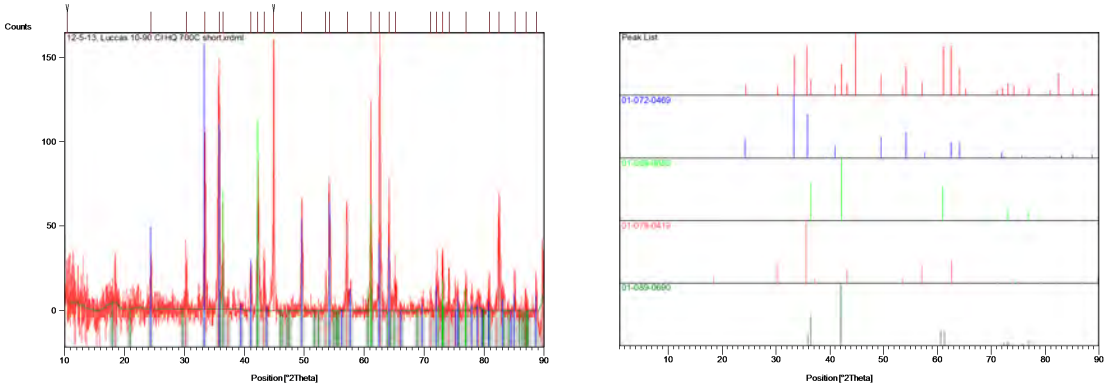

(a) Intensity vs. 2θ Plot (b) Identified Phase Plot

No.	Compound Name	Chemical Formula	RIR	SemiQuant [%]	Scale Factor
1	Hematite	Fe2 O3	3.240	42	0.954
2	Wuestite, syn	Fe0.925 O	3.880	25	0.685
3	Magnetite	Fe3 O4	5.140	23	0.840
4	Iron Oxide	Fe O	5.000	10	0.354

(c) semi-quantitative mass fraction data

Figure 6.9: XRD scan results for heat-treated CI powder with a maximum synthesis temperature of 700°C; a 1.48 hour scan time was used for the analysis.

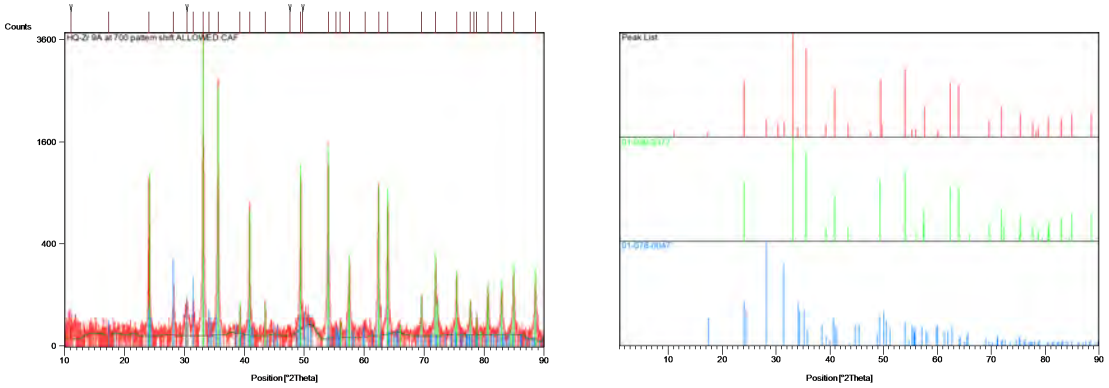

(a) Intensity vs. 2θ Plot (b) Identified Phase Plot

No.	Ref. Code	Score	Compound Name	Chemical Formula	RIR	SemiQuant [%]	Scale Factor
1	01-080-2377	93	Iron Oxide	Fe2 O3	3.290	96	1.021
2	01-074-1200	7	Baddeleyite, syn	Zr O2	4.640	4	0.065

(c) semi-quantitative mass fraction data

Figure 6.10: Heat-treated MRF powder sample scan results from MR powder batch 3A made using the old coating procedure. The maximum synthesis temperature was 700°C and a 1.48 hour scan time was used in the analysis.

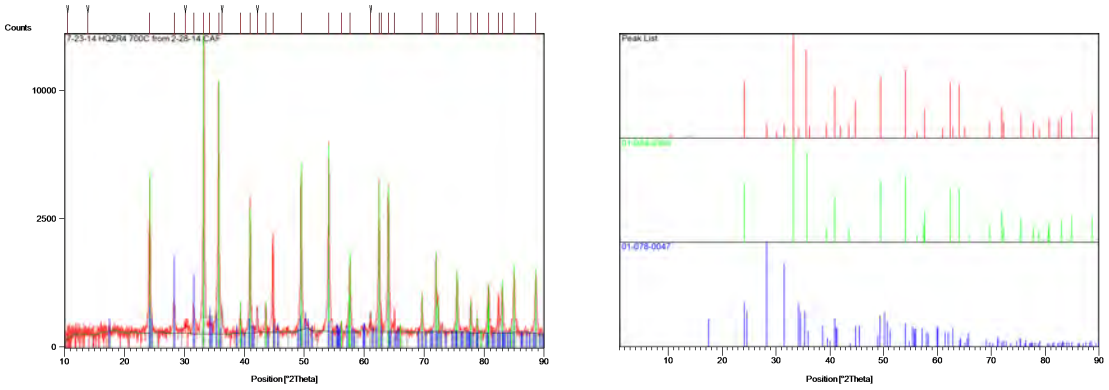

(a) Intensity vs. 2θ Plot (b) Identified Phase Plot

No.	Score	Compound Name	Chemical Formula	RIR	SemiQuant [%]	Scale Factor	Ref. Code	Displacement [°2Th.]
1	88	Iron Oxide	Fe2 O3	3.270	93	0.988	01-084-0306	0.038
2	24	Zirconium Oxide	Zr O2	3.520	7	0.080	01-078-0047	0.070

(c) semi-quantitative mass fraction data

Figure 6.11: Heat-treated powder sample scan results from a long duration scan of batch HQ-Zr 4, made using the old coating procedure. The maximum synthesis temperature was 700°C and a 7.41 hour scan time was used for the analysis.

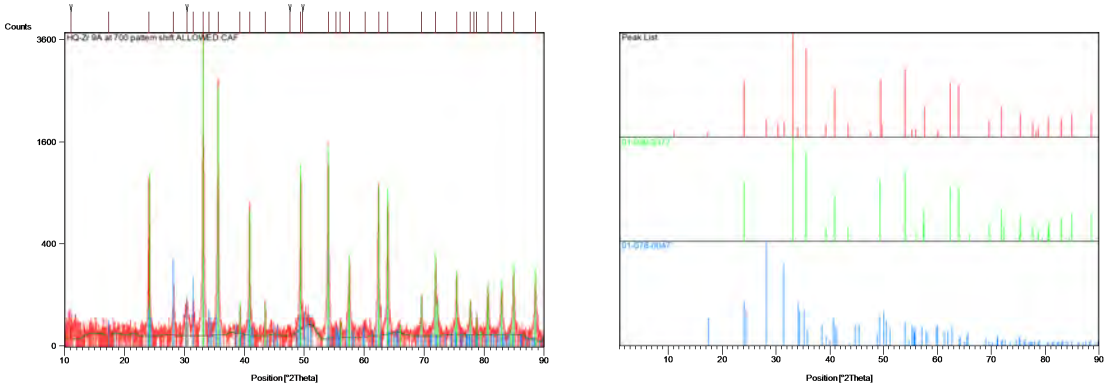

(a) Intensity vs. 2θ Plot (b) Identified Phase Plot

No.	Ref. Code	Score	Compound Name	Chemical Formula	RIR	SemiQuant [%]
1	01-080-2377	92	Iron Oxide	Fe2 O3	3.290	93
2	01-078-0047	35	Zirconium Oxide	Zr O2	3.520	7

(c) semi-quantitative mass fraction data

Figure 6.12: Heat-treated MR powder sample scan results from batch 9A (Table 4.1), with a maximum synthesis temperature of 700°C and a 1.48 hour scan time.

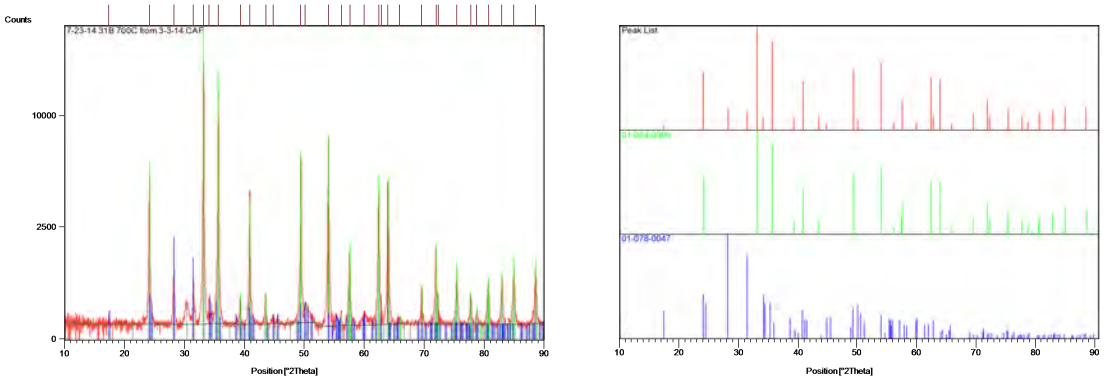

(a) Intensity vs. 2θ Plot (b) Identified Phase Plot

No.	Score	Compound Name	Chemical Formula	RIR	SemiQuant [%]	Scale Factor	Ref. Code	Displacement [°2Th.]
1	94	Iron Oxide	Fe2 O3	3.270	91	0.991	01-084-0306	-0.002
2	46	Zirconium Oxide	Zr O2	3.520	9	0.101	01-078-0047	0.030

(c) semi-quantitative mass fraction data

Figure 6.13: MRF powder sample scan results from a long duration scan of MR powder batch 31B, with a maximum synthesis temperature of 700°C and a 7.41 hour scan time.

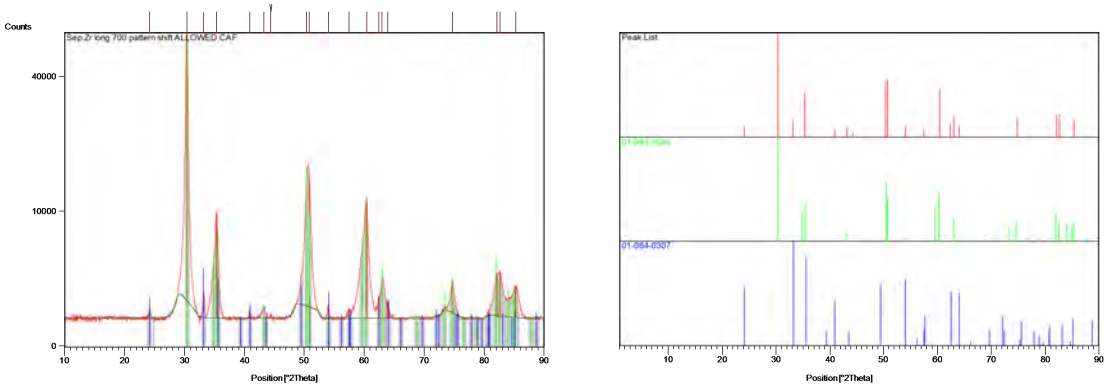

(a) Intensity vs. 2θ Plot (b) Identified Phase Plot

1	01-081-1544	79	Zirconium Oxide	Zr 01.95	10.260	85	0.957
2	01-084-0307	53	Iron Oxide	Fe2 03	3.270	15	0.054

(c) semi-quantitative mass fraction data

Figure 6.14: XRD scan results from ZrP1 (Table 5.1 on page 64) with a maximum synthesis temperature of 700°C. A 17.04 hour scan time was used for the analysis.

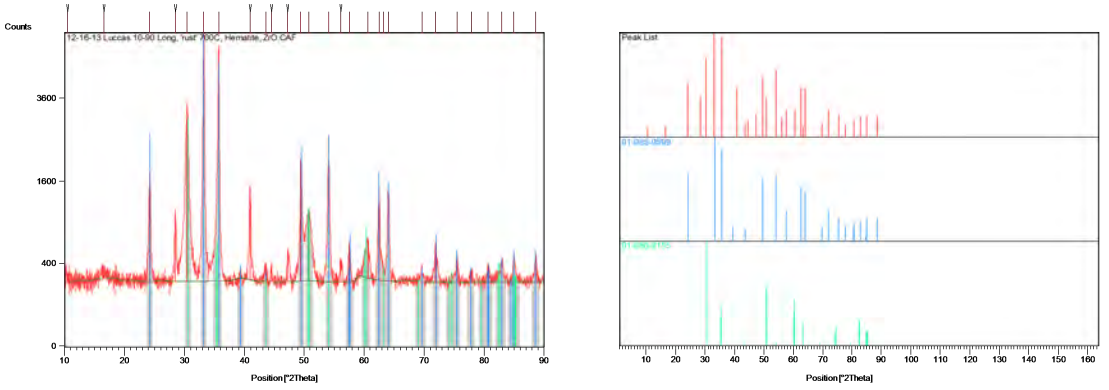

(a) Intensity vs. 2θ Plot (b) Identified Phase Plot

No.	Compound Name	Chemical Formula	RIR	SemiQuant [%]	Scale Factor
1	Hematite	Fe2 03	2.910	87	0.984
2	Zirconium Oxide	Zr 01.99	9.720	13	0.484

(c) semi-quantitative mass fraction data

Figure 6.15: XRD scan results from a ZrP3 powder sample (Table 5.1), with a maximum synthesis temperature of 700°C. A 17.04 hour scan time was used for the analysis.

Several areas in the analysis of the measurements that introduce variability: include

the setting selected for the compensation for background counts, manual peak editing, allowing pattern shifts, only using matches that have RIR values (necessary for computing mass fraction percent), and what match is first selected. Figure 6.16f demonstrates some of the variability in mass fraction that occurs, when matches with comparable scores were interchanged. Often the difference in mass fraction is $\leq 2-5\%$, but since the coated powders contain a small percentage of zirconia, this small variation needs to be taken into account. Prioritizing matches with RIR values also plays a role in the precision and accuracy of the results. The semi-quantitative mass fraction cannot be calculated unless every match has a RIR value, which becomes a problem because the first match for most scans did not have a RIR value. For iron oxide, there were often over 10 matches of various oxide compositions that ranged generally in score by ± 3. For example, all peak and stick plots in Fig. 6.16f appear to be very good matches and the various forms of iron oxide had very similar scores, indicating that they were reasonable choices. Depending on the initial pick, the available match scores for zirconia ranged from 33-48. In two of these analysis conditions, a 5 mass percent difference between Fig. 6.16c (hematite, Fe_2O_3 @ 83%; zirconium oxide, $ZrO_{1.99}$ @ 13%) and Fig. 6.16f (iron oxide, Fe_2O_3 @ 83%; baddeleyite, ZrO_2 @ 17%) was observed, which indicates the necessity to check several combinations of matches when there are many similar matches in the list. Knowledge of the MR powder composition can help to eliminate errors at this stage. The combination with the highest combined score, which indicates both sets of peak data are matched well with the scan, will provide the best results.

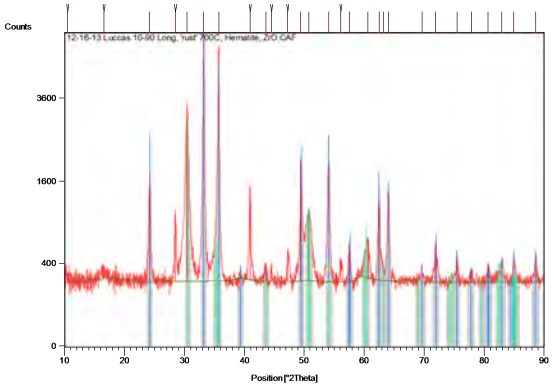

(a) Intensity vs. 2θ Plot

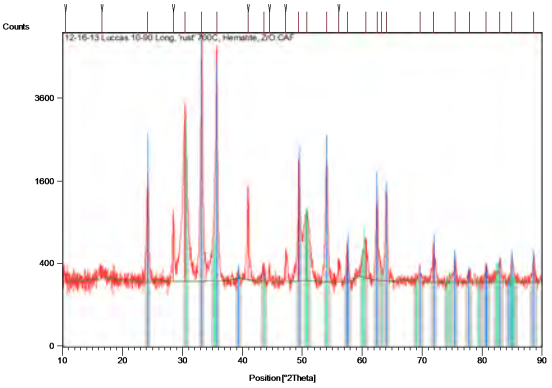

(b) Identified Phase Plot

No.	Compound Name	Chemical Formula	RIR	SemiQuant [%]	Scale Factor
1	Hematite	Fe2 O3	2.910	87	0.984
2	Zirconium Oxide	Zr O1.99	9.720	13	0.484

(c) Component match scores: hematite (85) and zirconium oxide (48)

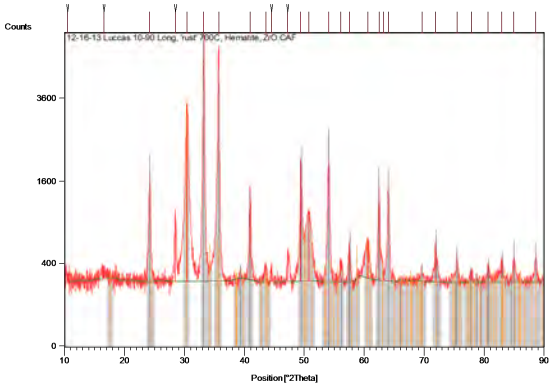

(d) Intensity vs. 2θ Plot

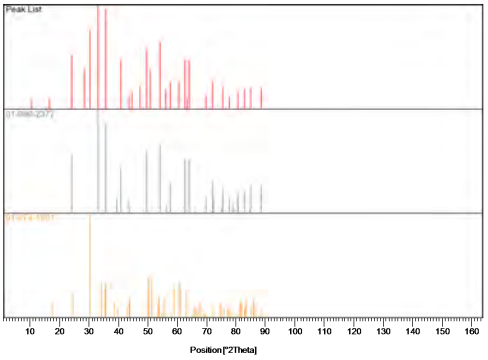

(e) Identified Phase Plot

No.	Score	Compound Name	Chemical Formula	RIR	SemiQuant [%]
1	85	Iron Oxide	Fe2 O3	3.290	83
2	33	Baddeleyite, syn	Zr O2	8.650	17

(f) Component match scores: iron oxide (85) and baddeleyite (33)

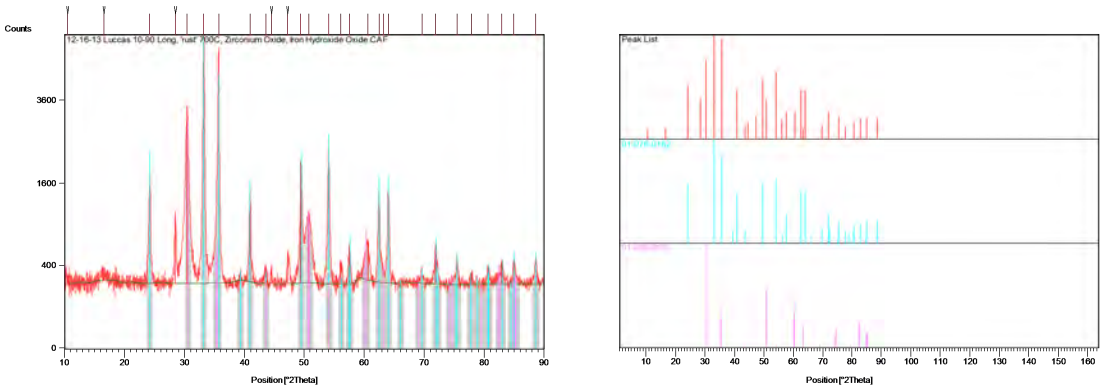

(g) Intensity vs. 2θ Plot (h) Identified Phase Plot

No.	Compound Name	Chemical Formula	RIR	SemiQuant [%]	Scale Factor
1	Iron Hydroxide Oxide	Fe1.833 (O H)0.5	2.740	88	1.046
2	Zirconium Oxide	Zr O1.99	9.720	12	0.484

(i) Component match scores: iron hydroxide oxide (87) and zirconium oxide (48)

Figure 6.16: Three different combinations of matches for the ZrP3 powder sample heat-treated at 700°C, and the effect these different combinations have on mass fraction.

The peak shift parameter can have a significant effect on both the score of the matches as well as the mass fraction of the components. The match score for iron oxide increased by 17 when peak shifting was allowed between Fig. 6.17 and Fig. 6.18, while the mass fraction of baddeleyite was halved. It is good practice to at least check for the change in scores when peak shifting is enabled. For this scan, enabling peak shifting increased the total score of the matches by 11, while the score for baddeleyite was decreased. Allowing the shift is very important when the powder scans have a high number of peaks, especially when the scan duration is short.

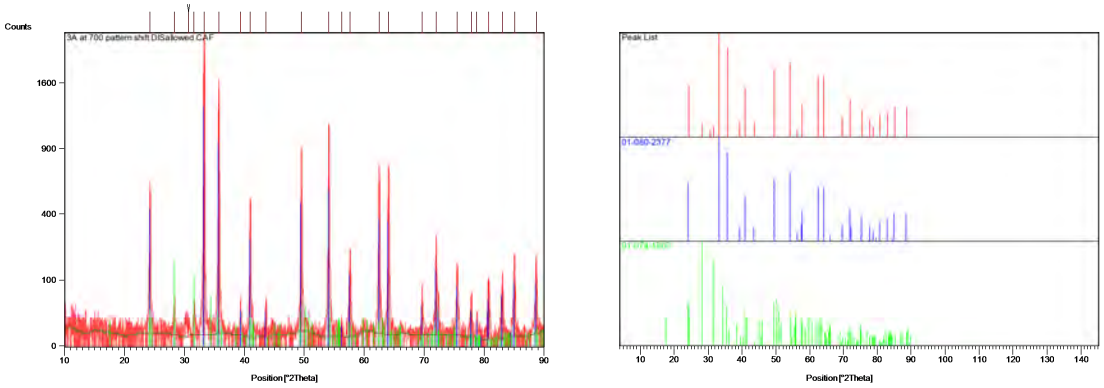

(a) Intensity vs. 2θ Plot (b) Identified Phase Plot

No.	Ref. Code	Score	Compound Name	Chemical Formula	RIR	SemiQuant [%]
1	01-080-2377	76	Iron Oxide	Fe2 O3	3.290	92
2	01-074-1200	13	Baddeleyite, syn	Zr O2	4.640	8

(c) semi-quantitative mass fraction data

Figure 6.17: Powder HQ-Zr 3A heat treated at 700°C, with peak shifting disabled.

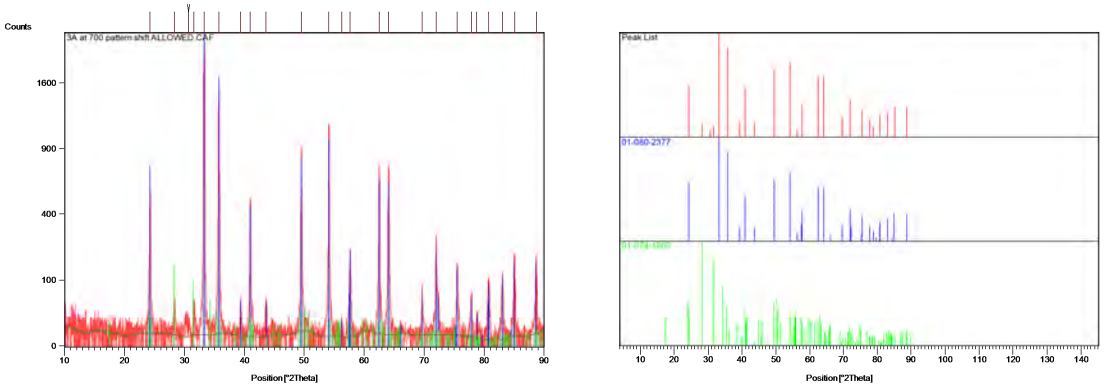

(a) Intensity vs. 2θ Plot (b) Identified Phase Plot

No.	Ref. Code	Score	Compound Name	Chemical Formula	RIR	SemiQuant [%]
1	01-080-2377	93	Iron Oxide	Fe2 O3	3.290	96
2	01-074-1200	7	Baddeleyite, syn	Zr O2	4.640	4

(c) semi-quantitative mass fraction data

Figure 6.18: Powder HQ-Zr 3A heat treated at 700°C, with peak shifting enabled.

6.2.2 Energy Dispersive Spectroscopy

Elemental analysis can be performed using EDS, where an incident beam of high energy electrons produces a spectrum of X-ray signals upon collision with the sample. The X-rays are converted into an array of electrical signals upon collision with the EDS detector [58]. The quantified X-ray energies are then mapped to the corresponding elements. Quantitative data can be obtained if the EDS data undergoes atomic number, absorption, and fluorescence correction abbreviated as ZAF[58]. All samples measured with EDS were exposed to a 23.0 KeV electron beam for two minutes. Quantitative results were obtained with element normalized, standardless ZAF correction of characteristic K_{α_1}, L_{α_1}, and M_{α_1} X-rays.

Seven MR powder samples were analyzed using the "EDaX" brand EDS detector in the Zeiss-Auriga SEM/FIB instrument located in the URnano Metrology Facility. The EDS measurements were used to determine the mass fraction of elements from a wide range of MR powder samples (Table 6.1). All samples were prepared by spreading a thin layer of MR powder on carbon tape that had been adhered to an SEM sample stub. The MR powder samples were overcoated with carbon rather than gold, because the characteristic X-ray energies for zirconium L_{α_1} and gold M_{α_1} are very similar (Zr L_{α_1} = 2.042 KeV, Au M_{α_1} = 2.120 KeV) and interferes with quantitative data collection [59]. The energy for the carbon K_{α_1} (0.277 KeV) is too small to interfere with zirconium or iron signals. Powder samples from ZrP1 and ZrP3 were gold-coated, since the strength of the zirconium signal emitted from these samples was sufficiently large to differentiate

the zirconium peaks from those of gold,

Table 6.1: Sample description and coating techniques used on samples measured using EDS.

Sample	**Description**	**Coating Techniques**
31-B	0.5 − 2.0 µm iron powder coated using the NCP	Carbon evaporation
PS-31 B	0.5−2.0 µm iron powder remaining after ZrP1, prepared using the NCP	Carbon evaporation
HQ-Zr 4	0.5 − 2.0 µm iron powder coated using the OCP	Carbon evaporation
325-NCP	Sub 44 µm iron powder coated using the NCP	Carbon evaporation
325-OCP	Sub 44 µm iron powder coated using the OCP	Carbon evaporation
ZrP1	Concentrated zirconia collected via magnetic separation	Gold sputter
ZrP3	Concentrated zirconia collected from the first step of the MRF powder wash process	Gold sputter

Four different MRF powders, that were believed to have unique iron and zirconium ratios due to distinct combinations of particle size and coating technique were tested. Two powders with high zirconia concentration, ZrP1 and ZrP3, were evaluated to determine the level of success in isolating zirconia from the MRF powder batches. There was interest in determining the differences in composition of the powders, as well as the utility of using EDS for characterization of other MRF powders. Comparison of the EDS results for sample 31-B to sample HQ-Zr 4 indicates that the NCP produces powders with a higher concentration of zirconium (Table 6.2), which was also confirmed by the results from 325-NCP and 325-OCP. Measurement of sample ZrP1 displayed a very

high concentration of zirconium relative to iron ($\approx 8:1$), indicating that the magnetic separation technique (ZrP1) was successful in collecting free zirconia from the bulk MR powder. The high ratio of zirconium to iron ($\approx 3:1$), measured in sample ZrP3 indicates that most of the particles removed from the bulk powder during the wash process (Section 3.2.3, pg. 16) have a high concentration of zirconia. The presence of zirconia-rich particles in ZrP3 indicates that some free zirconia is lost during the wash process, and reduces the concentration of free zirconia in the final MR powder. The higher concentration of zirconium in ZrP1 than ZrP3 implies that magnetic separation is useful method for extracting free zirconia from MRF powder. Sample PS 31-B (the MR powder remaining after ZrP1) shows a higher concentration of iron than was observed in sample 31-B, along with lower concentrations of oxygen and carbon. Both samples have a similar concentration of zirconium. The difference in the weight % of the various elements in PS 31-B and 31-B indicates a reduced zirconia concentration in PS 31-B, which is consistent with the expected result.

All samples analyzed by EDS showed a high weight % of carbon (Table 6.2); this high signal was due to both carbon tape under the powder layer and the carbon coating on the MR powder samples (Table 6.1). Samples ZrP1 and ZrP2 both showed a gold concentration, due to the sputter coating, of ~ 10 wt% due to the sputter coating. The reduction of the carbon signal in 325-NCP and 325-OCP as compared to the other the MR powder samples measured using the same settings is likely due to the larger particle size in these samples as compared to the volume of the incident beam [58].

Table 6.2: Quantitative results from EDS analysis (measurement time = 2.0min). This analysis provides the atomic weight % of elements present in seven powder samples. Calculation of weight % is derived from the measured intensity of characteristic X-rays emitted from the samples after the ZAF correction algorithm has been applied.

Sample	Fe K_{α_1}	Zr L_{α_1}	O K_{α_1}	C K_{α_1}	Au L_{α_1}
31-B	46.83	4.26	14.71	34.20	
PS 31-B	54.97	4.32	12.97	27.75	
HQ-Zr 4	52.23	1.77	11.34	34.66	
325-NCP	54.40	8.17	19.66	17.77	
325-OCP	61.45	6.19	16.74	15.63	
ZrP1	2.73	22.85	21.26	44.26	8.91
ZrP2	7.69	24.62	23.48	34.33	9.88

6.2.3 X-ray Mapping

The EDaX EDS detector was used to produce X-ray maps of samples from three different powders. Element concentration is proportional to the number of colored pixels in element maps. Samples that were mapped include: (1) a carbon-coated MR powder sample from batch 31-B (Fig 6.19); (2) a cross-section of a particle from MR powder batch 325-NCP embedded in a gold-coated thermosetting epoxy puck (Fig 6.20); and (3) a gold-coated powder sample from ZrP1 (Fig 6.21). All maps were collected with a 20.0 KeV acceleration voltage. It was expected that X-ray maps of these powders would provide information on the diversity in elemental location and concentration within the samples.

The map of sample 31-B is representative of the NCP MR powders. The mapped area (12.25 µm × 9.2 µm) contained a small agglomeration of ≈ 25 particles (Fig 6.19a). There was a significant iron signature that corresponded to the particle locations. Concentration of the oxygen signature around the agglomeration indicates the presence of

oxides. The zirconium signal is also concentrated on the agglomeration. A high carbon signature originating from the carbon tape that the particles were adhered to was also observed.

It was expected that mapping a cross section of a large ($\approx 35m\mu$ diameter) 325-NCP particle would show a higher zirconium concentration around the edge of the coated particle (Fig 6.20a). The strong iron signature coincides with the location of the particle (Fig. 6.20b). Buehler ProbeMet conductive thermosetting molding compound (Fig 5.5a, pg. 69), which the 325-NCP powder was embedded in, contains copper and silica, explaining the presence and location of the oxygen, silicon, and copper signatures (Fig. 6.20c and 6.20f - 6.20g) [78]. There is a weak zirconium signature present on the left and top portions of the particle; X-ray mapping was incapable of confirming the presence of a contiguous zirconia coating. The low mass fraction of zirconia, limited resolution of X-ray mapping, and sample geometry all contributed to the inability to create a map of the zirconia coating [58]. A carbon signature was present in the areas surrounding the coated iron particle.

A powder sample from ZrP1 was mapped to determine its zirconia and iron concentrations (Fig 6.21). The weak iron signature may indicate that sub-micron sized iron particles, whos magnetic potential is too small to be removed during the ZrP1 process, are coated by the sol-gel. The oxygen signature implies the presence of oxides. There is a strong zirconia signal, which suggests the success of ZrP1 in isolating zirconia particles from the MR powder.

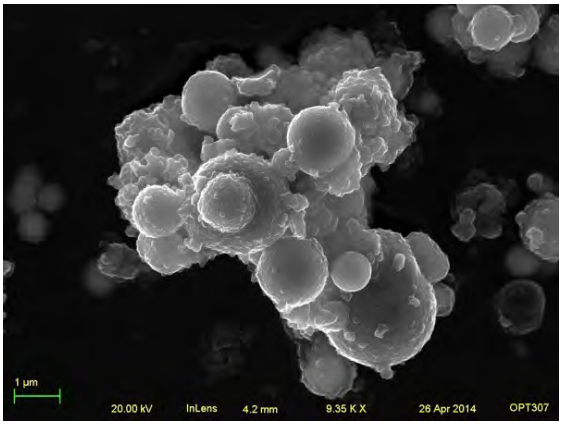

(a) An SEM image of a clump of MRF particles from batch 31-B

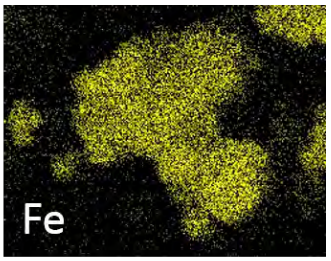

(b) An X-ray map showing the location and concentration of iron in Figure 6.19a

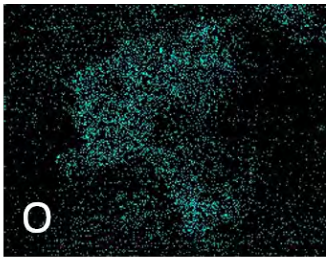

(c) An X-ray map showing the location and concentration of oxygen in Figure 6.19a

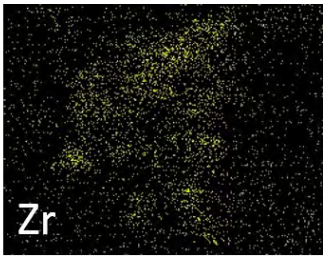

(d) An X-ray map showing the location and concentration of zirconia in Figure 6.19a

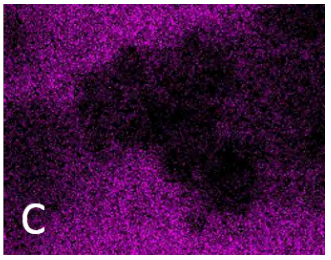

(e) An SEM micrograph and X-ray maps showing the location and concentration of carbon in Figure 6.19a

Figure 6.19: An X-ray map created using an EDAX detector and a carbon coated MRF powder sample from batch 31-B.

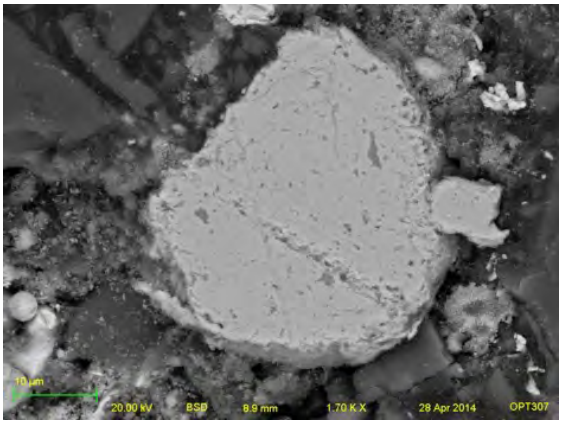

(a) An SEM image of a particle cross section from batch 325-N embedded in a thermosetting epoxy puck

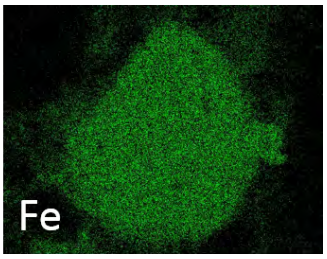

(b) An X-ray map showing the location and concentration of iron in Figure 6.20a

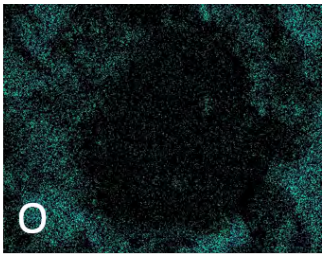

(c) An X-ray map showing the location and concentration of oxygen in Figure 6.20a

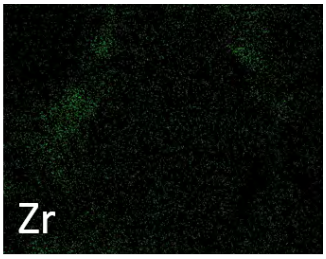

(d) An X-ray map showing the location and concentration of zirconia in Figure 6.20a

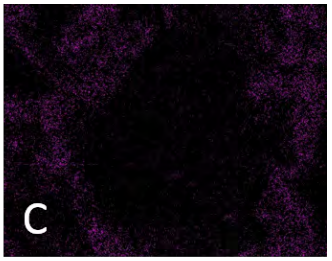

(e) An X-ray map showing the location and concentration of carbon in Figure 6.20a

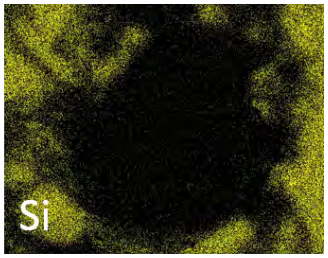

(f) An X-ray map showing the location and concentration of silicon in Figure 6.20a

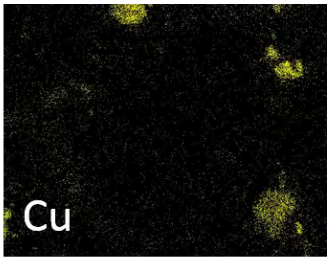

(g) An X-ray map showing the location and concentration of copper in Figure 6.20a

Figure 6.20: An SEM micrograph and X-ray maps created using an EDAX detector and a gold coated MRF powder sample from batch 325-N embedded in a thermosetting epoxy puck shown in Figure 5.5f on page 69. Note the significant concentrations of copper and silicon present in the thermosetting epoxy.

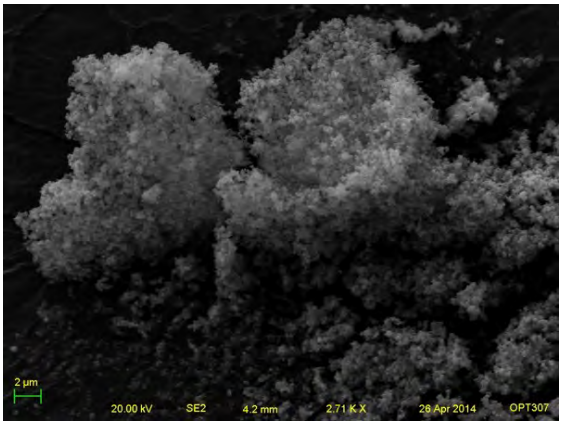

(a) An SEM image of a clump of carbon coated particles obtained from process ZrP1

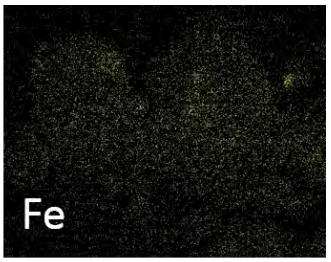

(b) An X-ray map showing the location and concentration of iron in Figure 6.21a

(c) An X-ray map showing the location and concentration of oxygen in Figure 6.21a

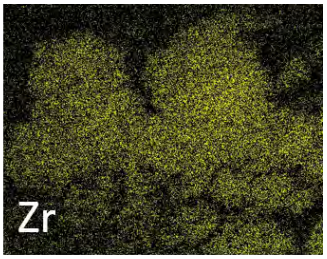

(d) An X-ray map showing the location and concentration of zirconia in Figure 6.21a

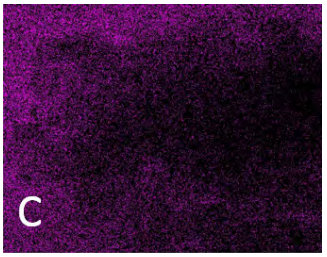

(e) An X-ray map showing the location and concentration of carbon in Figure 6.21a . The strong carbon signature is caused by the carbon tape which the particles are adhered to.

Figure 6.21: An SEM micrograph and X-ray maps created using an EDAX detector and a gold coated powder sample from batch ZrP1.

6.2.4 X-ray Photoelectron Spectroscopy

Surface characteristics of MRF powder samples were analyzed with X-ray photoelectron spectroscopy (XPS). This analysis technique provides data from a thin surface region, between $3 - 30$ nm, dependent on material and inelastic mean free path (IMFP) of

electrons [51]. Scan results of MRF powder samples sent to the Cornell Center for Materials Research (CCMR) are shown in Figure 6.22, and Table 6.3. Samples were prepared by applying a layer of MRF powder to a piece of carbon tape on an SEM sample stub. The powders sent for analysis at CCMR were: (1) magnetically separated zirconia powder (ZrP1); (2) Batch 18A (an NCP powder); and (3) a sample from MR powder batch 18A remaining after magnetic separation (PS 18A). It was expected that results from the ZrP1 scan would have no iron signal, and that 18A would have a stronger zirconia signal than PS 18A. All scans had strong carbon signatures from the adhesive carbon tape that the MRF powders were adhered to. Organic contaminants, including dust and finger-prints, may have further increased the carbon content. Oxygen had the highest elemental concentration in all scans; the strong oxygen signal indicates the presence of ZrO_2, Fe(II) oxide, and Fe(III) oxide in the $\approx$ 20 nm scan depth. Results from the scan of ZrP1 powder sample shows a significant zirconium signal, with no iron detected (Table 6.3). The powder sample from batch 18A showed a larger iron signal than zirconium, which indicates a significant portion of the powder has a coating less than $\approx$ 20 nm thick [51]. The PS 18A scan has a slightly lower ratio of zirconium to iron when compared to the 18A sample which may be due to the zirconia extracted via ZrP1. These results indicate that the ZrP1 process was successful in separating free zirconia from the iron powder, while also demonstrating that the coating thickness of the MR powders have at least some regions less than 20 nm thick.

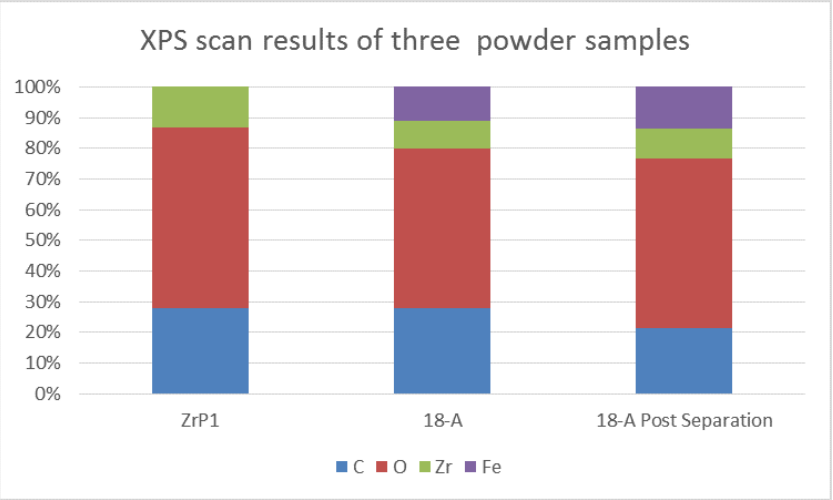

Figure 6.22: Three powder samples analyzed with XPS at CCMR. Powder from ZrP1, 18-A, and a sample from 18-A remaining after zirconia separation process ZrP1.

Table 6.3: Three MRF powder samples adhered to carbon tape, sent to CCMR for XPS analysis

	Element (Atomic %)			
Powder Sample	**C**	**O**	**Zr**	**Fe**
ZrP1	27.99	58.93	13.08	0.00
18A	27.90	52.14	8.76	11.20
PS 18A	21.47	55.29	9.69	13.55

Several more MR powders were analyzed at the URnano XPS facility in Gavett Hall at the University of Rochester. These additional measurements verified the results obtained from CCMR shown in Table 6.3 and increased the number of samples analyzed by XPS. The MR powders scanned in the URnano facility were placed onto an adhesive copper strip, with the intent of reducing the carbon signature due to the tape used in earlier experiments. A scan of the adhesive was collected to provide a background signature, to serve as a comparison to the other results. Surprisingly, scan results for all samples

had strong carbon signatures. The strongest carbon signal was found in a scan of the copper adhesive (Table 6.4), indicating a high concentration of carbon on the adhesive's surface. Because the MR powder samples were applied to the adhesive as a monolayer, it is likely that the strong carbon signature present in all sample scan results is derived from the background noise of the adhesive. The carbon signal was not present in the data obtained from CCMR; it was likely removed during data-processing. The range of oxygen content was significant (12.39% for the adhesive and 42.2% for 325-NCP). When compared to the background signature from the adhesive, the MRF powders have a high oxygen concentration, which confirms the findings in Table 6.3 and suggests that oxides are present in the MR powder samples. When comparing powders of similar particle size, the NCP MRF powders had a greater atomic concentration of oxygen than the OCP powders. The ratio of iron to zirconium was smaller in NCP powders than OCP powders, which implies that there is a thicker ZrO_2 coating on the NCP powders due to the decreased iron signal. Analysis of the powder sample from ZrP1 produced no signal from iron, which agrees with the results in Table 6.3. The small iron signature in ZrP2 suggests that some carbonyl iron particles are removed when the supernatant is decanted during the drying procedure (Subsection 3.2.3).

Table 6.4: XPS results from region of interest scans for a variety of MRF powder samples.

	Element (Atomic %)							
Powder Sample	**C**	**O**	**Zr**	**Fe**	**Si**	**N**	**F**	**Fe/Zr**
31B	60.09	33.16	4.65	1.36	0.10	0.00	0.64	0.29
HQ-Zr 4	68.13	26.85	2.33	0.98	1.72	0.00	0.00	0.42
PS 31B	69.86	25.77	2.60	0.74	1.01	0.00	0.00	0.28
325-NCP	47.63	42.17	4.39	5.56	0.26	0.00	0.00	1.27
325-OCP	52.49	38.01	3.69	5.42	0.40	0.00	0.00	1.47
ZrP1	50.43	40.32	9.26	0.00	0.00	0.00	0.00	0.00
ZrP2	58.48	33.84	6.21	0.34	0.81	0.00	0.00	0.05
Adhesive	86.31	12.39	0.00	0.00	0.79	0.51	0.00	0.00

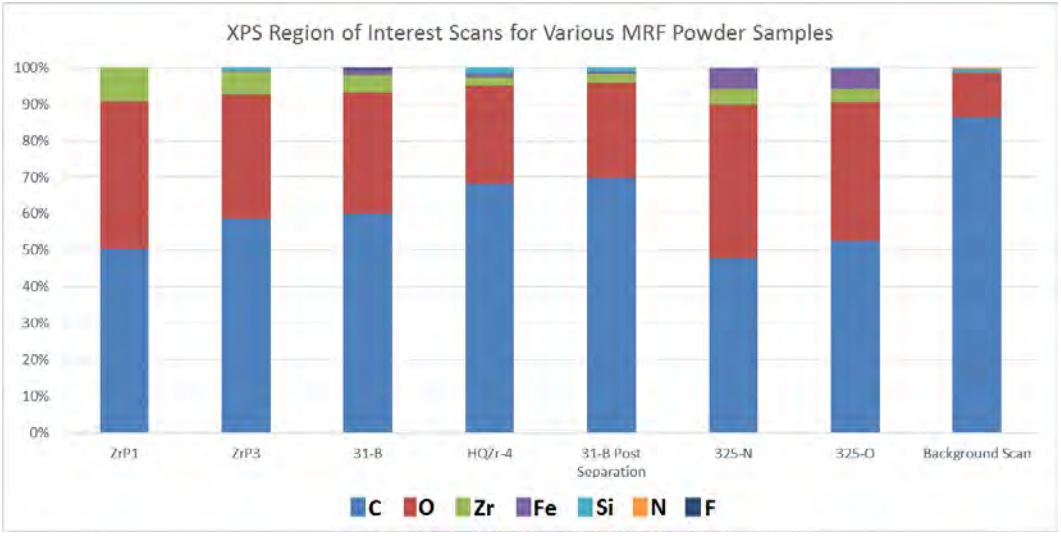

Figure 6.23: XPS region of interest results for a variety of MRF powder samples.

6.2.5 X-ray Fluorescence

Thirty-five MR powder samples were measured using XRF in under three hours, which is orders of magnitude faster than other analytical X-ray techniques used. These samples

required no preparation prior to measurement and the analysis time for each powder was only three minutes. It was also possible to collect data from samples with a very low volume of powder. The XRF technique is nondestructive and analyzed samples taken from bulk MR powders could be returned to the original containers directly after analysis. The raw data collected with the S1PXRF program was analyzed using Bruker's ARTAX software. A Bayesian deconvolution method in the ARTAX program was used to match raw spectral data to the elements present in the scans. The deconvoluted data from 41 measurements were normalized for quantitative analysis and the region of interest (ROI) and normalized data were exported to Microsoft Excel. Iron and zirconium were the only detected elements. When data collection is performed without use of a vacuum chamber, energy dispersive (ED) XRF is incapable of detecting elements lighter than sodium[60].

The NCP MRF powders produced larger zirconia signals than the OCP MRF powders (Fig. 6.24). Results of individual scans are very similar to the average results for that sample type. The NCP MR powder 50B shows a 0.09% difference in atomic composition when compared to the averaged data from 11 NCP powders (Table 6.5). Measurements of the iron powders show very high purity (99.96% Fe), although the trace elements of carbon and nitrogen present in the BASF CI powder could not be detected [61]. Results from scans of ZrP1 and ZrP4 both showed zirconium purities of over 98.5%. The zirconium signal from NCP MRF powders was twice the intensity of OCP powders, confirming the significant increase in total zirconia concentration in these powders.

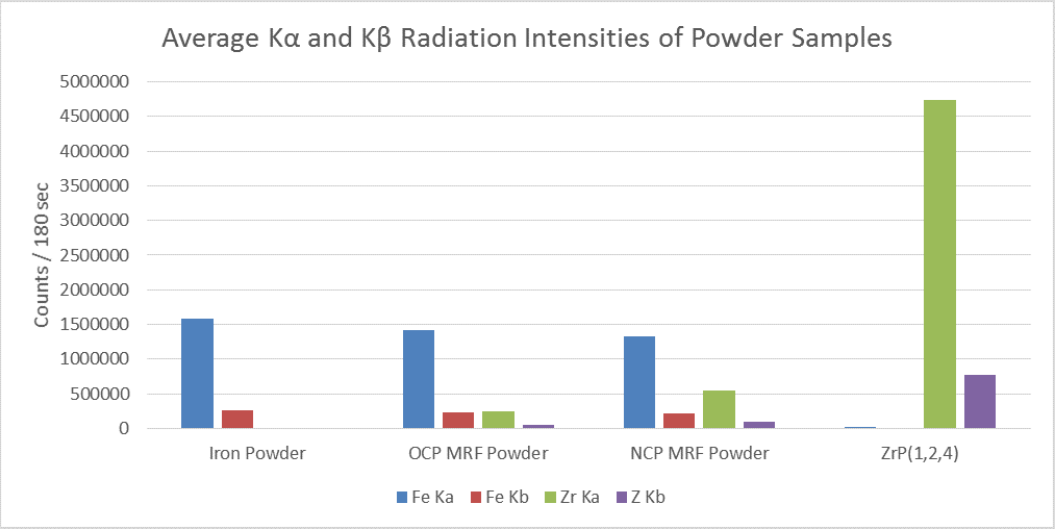

Figure 6.24: The average K_α and K_β intensities for (a) CI powder; (b) OCP MR powders; (3) NCP MR powders; and (4) concentrated zirconia powders.

Table 6.5: Quantitative results from XRF measurements of two types of MR powders, iron powders and concentrated zirconia powder samples.

	Counts / 180s				Atomic %	
Sample	Fe K_α	Fe K_β	Zr K_α	Zr K_β	Fe	Zr
CI-HQ	1,621,274	285,358	686	81	99.96	0.04
HQ-Zr 4	1,472,989	260,255	253,322	46,904	85.32	14.68
50B	1,339,404	238,508	565,935	105,709	70.30	29.70
ZrP1	74,623	13,453	641,6357	1,036,985	1.15	98.85
ZrP4	3,008	677	743,7428	1,222,363	0.04	99.96
Iron Powders[1]	1,587,133	262,213	457	151	99.97	0.03
OCP Powders[2]	1,415,983	239,948	244,157	46,063	85.41	14.59
NCP Powders[3]	1,323,138	222,675	546,810	102,594	70.69	29.31
ZrP# Powders[4]	29,381	4,840	4,730,100	77,4323	1.56	98.44

[1] Average results from two CI-HQ and 325-mesh powder measurements
[2] " " " measurements of eight OCP MRF powders
[3] " " " measurements of eleven NCP MRF powders
[4] " " " seven measurements of ZrP1, ZrP2, and ZrP4 powders

6.3 Mass-Based Calculation of Powder Composition

An estimate of zirconia concentration can be made using the difference between the initial mass of uncoated CI-HQ powder and the final mass of the coated MR powder. For both the OCP and NCP powder, the coating process starts with 200 g of CI-HQ powder. The average mass of 71 NCP MR powder batches is 229.7 ± 5.1 g, which represents a ∼30 g increase from the initial 200 g of CI-HQ powder; the average mass of five OCP MR powder batches is 213.5 ± 3.7 g. Results from various X-ray techniques show that the only chemical species in the coated powders are iron, iron oxides, and zirconia. The 30 g mass increase can thus be attributed to the adsorption of zirconia onto the iron powder during the sol-gel coating process. Table 6.6 shows estimates of mass fraction distribution based on the "change in mass calculation" (ΔMC) of the MR powder during coating. Several additional mass fraction distributions were calculated based on an assumed decrease in CI mass caused by corrosive dissolution of iron during coating with the pH ∼1 sol-gel.

Table 6.6: Estimate for mass fraction of MR powder components based on the change in mass during the coating process. Additional values are based on assumed loss of iron.

	Mass Fraction(%)		
MR Powder	Fe, Fe(ii,iii)	ZrO_2	Assumed Loss of Iron*
OCP †	93.68	6.32	0
OCP	89.83	10.7	5
OCP	85.10	14.90	10
OCP	80.37	19.63	15
NCP§	87.09	12.91	0
NCP	82.73	17.27	5
NCP	78.38	21.62	10
NCP	74.03	25.97	15

* Assumed loss of iron from dissolution of iron ions from corrosion of the CI-HQ powder during coating in the pH ∼1 sol-gel.
† Based on an average OCP batch mass of 213.5g.
§ Based on an average NCP batch mass of 229.7g.

6.4 Pycnometry

An AccuPyc II 1340 helium gas pycnometer was used to perform density measurements of uncoated CI powders, OCP and NCP MR powders. Several uncoated CI powder samples were analyzed prior to evaluating the coated MR powders to confirm both the precision of both the measurement technique and the AcuPyc II 1340 instrument. Before being loaded into the pycnometer sample cup, all coated powders were agitated to normalize particle size distribution. The order of measurements performed on the OCP and NCP MR powders were randomized to reduce the impact of experimental error. The average NCP powder density is lower than the average OCP powder density, indicating a higher concentration of zirconia (Table 6.7).

Results from iron powder measurements were precise; for seven samples, $\sigma = 0.001$

g/cm^3 (Fig. 6.25a and Table 6.7).The OCP and NCP MR powders had density ranges of 0.630 g/cm^3 and 0.573 g/cm^3, which is approximately four times greater than the range reported for the iron powder densities (Fig. 6.25). The measured density of ZrP4, powder obtained from the calcination of zirconia sol-gel at 100°C, was 2.462 ± 0.001 g/cm^3. This measurement is much lower than the density of ZrO_2 (5.76 g/cm^3 [62]), indicating that the calcination temperature was too low, and organic polymers from the sol-gel are still present in the powder.

Table 6.7: Results of density measurements of iron powders, OCP and NCP MRF powders.

Sample Type	Avg. Density (g/cm^3)	σ (g/cm^3)	Median (g/cm^3)	Range (g/cm^3)
NCP Powders*	6.211	0.133	6.221	0.573
OCP Powders†	6.605	0.213	6.601	0.630
Iron Powders§	7.661	0.056	7.683	0.147

* Results from 34 sample measurements.
† Results from eight sample measurements.
§ Results from seven sample measurements.

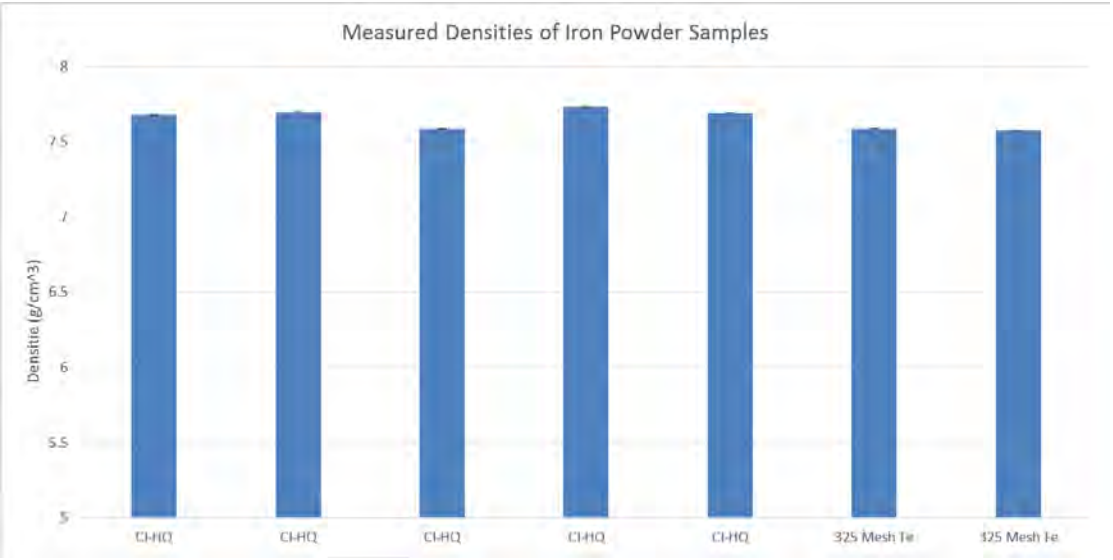

(a) Density measurements (with an average standard deviation = 0.056 g/cm^3) of two types of iron powder used as the base of MR powders.

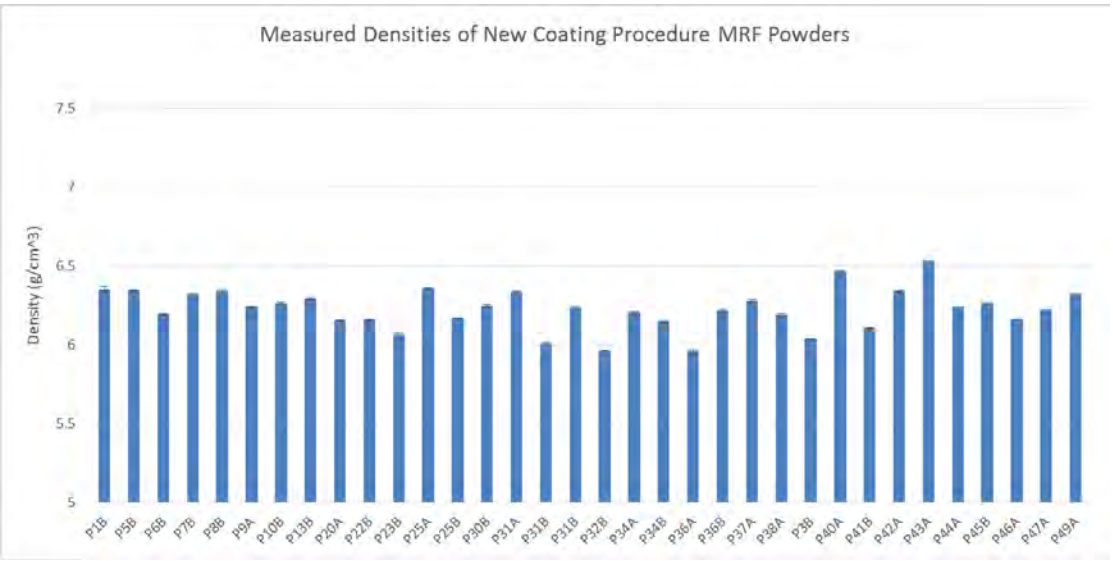

(b) Density measurements (with an average standard deviations = 0.133 g/cm^3) of 34 NCP MRF powders.

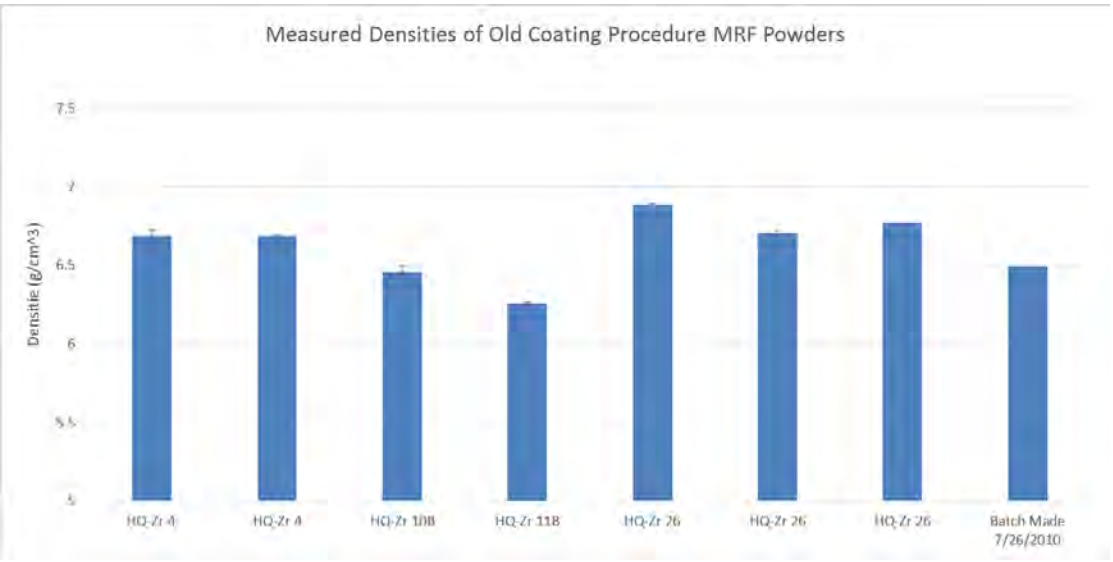

(c) Density measurements (with an average standard deviation = 0.213 g/cm^3) of eight OCP MRF powders.

Figure 6.25: Three graphs displaying results of density measurements of uncoated CI powders, OCP and NCP MRF powders.

6.5 Combined Technique Mass Fraction Analysis

Results from a several analytical techniques have been combined both to investigate their accuracy and obtain a better idea of powder composition. Pycnometry data yields information on MR powder density, volume and mass. Analytical X-ray techniques contribute semi-quantitative mass fraction data. By using the measured sample density, mass, and volume in conjunction with semi-quantitative results from a different analytical technique, a new theoretical density value was calculated (Table 6.8). A CI-HQ powder density of 7.661 g/cm^3 was used, based on average density measurements (Table 6.7). A density of 5.76 g/cm^3 was used for zirconia [62]. The iron oxide species was assumed to be Fe(ii,iii) based on XRD results (Section 6.2.1). A value of 5.1 g/cm^3 was used for the density of Fe(ii,iii) [63]. A porosity term was added to the calculation, which

provided a second term to evaluate the validity of a given analytical X-ray technique. The calculated density may match the measured density, while the calculated volume may be significantly larger or smaller than the measured value. The porosity term was calculated from the product of the powder's mass, the inverse density of the species, and the semi-quantitative mass fraction distribution. A negative porosity indicated the calculated volume was larger than the measured sample volume.

X-ray diffraction designates specific oxide concentration, while the other X-ray techniques provide information on element concentration. For the elemental analysis techniques that can't provide oxide concentration, the ratio between iron and iron oxide concentrations were adjusted to provide the best fit to the measured volume and density. The mass fraction distribution for ΔMC (#1-6 in Table 6.8) are based on the assumptions made in Section 6.3. For calculations done with the OCP powders XRF #3, the ΔMC #3 calculations resulted in the best fit to the measured data (Table 6.8). The XRD and EDS measurements estimate a significantly lower concentration of zirconia and lower densities when compared to the results of XRF measurements. Of the NCP powder calculations, XRF #9, ΔMC #4, and ΔMC #6 showed the closest fit to pycnometry measurements. The XRD measurement shows a close fit to the measured volume, but the calculated density is 0.09g/cm^3 higher than the density measurement from pycnometry. The EDS data shows a ∼13% increase in calculated volume and a 0.43g/cm^3 lower than measured density.

Table 6.8: Mass fraction and porosity % calculations of OCP and NCP MRF powders, using pycnometry data to supplement XRF, XRD, EDS, and ΔMC measurements.

	Mass Frac. (%)			**Calculated Results**		
	Fe	Fe(ii,iii)	ZrO_2	Vol. (cm^3)	Porosity (%)	ρ (g/cm^3)
OCP Powder Data						
Pycnometry Data*				0.2191		6.69
XRF #1†	85.0	0.0	15.0	0.2008	8.38	7.38
XRF #2	63.8	21.2	15.0	0.2212	−0.94	6.83
XRF #3	58.0	27.0	15.0	0.2267	−3.46	6.68
XRF #4	42.5	42.5	15.0	0.2416	−10.25	6.29
XRF #5	0.0	85.0	15.0	0.2824	−28.89	5.20
ΔMC #1§	60.7	33.0	6.3	0.2270	−3.58	6.70
ΔMC #2	59.5	30.3	10.2	0.2268	−3.49	6.69
ΔMC #3	58.2	26.9	14.9	0.2265	−3.37	6.69
XRD	54.7	41.3	4.0	0.2335	−6.55	6.53
EDS	45.0	50.0	5.0	0.2433	−11.02	6.30
NCP Powder Data						
Pycnometry Data*				0.2120		6.24
XRF #6†	70.0	0.0	30.0	0.1896	10.5327	7.09
XRF #7	52.5	17.5	30.0	0.2048	3.3789	6.64
XRF #8	35.0	35.0	30.0	0.2195	−3.7750	6.19
XRF #9	31.0	39.0	30.0	0.2115	−2.9574	6.25
XRF #10	0.0	70.0	30.0	0.2276	−18.0827	5.30
ΔMC #4§	41.0	46.1	12.9	0.2199	−3.7291	6.24
ΔMC #5	39.5	43.5	17.3	0.2205	−4.0493	6.24
ΔMC #6	38.9	39.5	21.6	0.2191	−3.3794	6.24
XRD	47.7	42.3	9.0	6.4576	−0.0300	6.33
EDS	21.0	61.0	19.0	0.2379	−12.2622	5.81

* Density and volume results from density measurements collected with the Accupyc II 1340.
† This row, along with the rows below, demonstrate the effect that increasing concentrations of oxidized iron has on the volume and density of the MR powder.
§ ΔMC represents mass fraction calculations based on the difference between initial and final batch mass.

6.6 Mass Fraction of free Zr in bulk MRF powder

A magnetic separation technique was employed to determine the concentration of free zirconia in the bulk MRF powder (Subsection 5.2.1, pg. 56). The concentration of free zirconia in the powder affects the amount of additional polishing abrasives that are added to the MRF slurry. In this experiment, 100 g of NCP MR powder was milled for ~ 5 min and exposed to high shear mixing prior to magnetic separation and centrifuging of the nonmagnetic particulate slurry (Subsection 5.2.1s). The solid particles at the bottom of the centrifuge tubes were transfered to 20 mL glass sample vials, and the remaining slurry in the test tubes was placed in 200 mL beakers. The sample containers were placed in a convection oven to evaporate the DI water. The mass of the free zirconia was determined by subtracting the mass of the empty sample containers from that of the containers holding the dried sample powder (Table 6.9). The 100 g of NCP MR powder yielded 0.28349 g of solid particulate after drying.

Table 6.9: Mass of nonmagnetic particulate collected via magnetic separation from 100 g of NCP MRF powder.

	Mass (g)		
Collection Vessel	Vessel	Vessel w/ Particulate	Particulate
Vial #1	13.47482	13.32550	0.11516
Vial #2	13.44838	13.33005	0.11833
Beaker #1*	223.04	223.07	0.03
Beaker #2*	217.40	217.42	0.02
Total			0.28349

* Because the mass of the empty beakers exceeded the weighing range of the analytical balance, a balance with a larger weight range (but lower accuracy) was used instead.

6.7 Surface Characteristics and Coating Thickness

Micrographs collected by SEM were used to characterize both the surfaces and cross sections of various MR powders. It was expected that micrographs of the OCP and NCP MR powders might be visually distinct, as they were produced by different methods. Scanning electron microscopy also enabled the comparison between the surface structures on the zirconia coated MRF powders and the concentrated zirconia powder collected via ZrP1 (Subsection 5.2.1). Micrographs of MRF powder cross sections were analyzed using ImageJ [64] to provide semi-quantitative information on the zirconia coating thickness of the MRF powders.

Micrographs of powder samples from batch 31B (NCP) show a variety of particle sizes and surface structures (Fig. 6.26). The surface structure of PS 31B (the MR powder remaining after procedure ZrP1), is indistinguishable from that of 31B (Figs. 6.26b, and 6.26d). Due to the wide variety of surface characteristics observed (Fig. 6.26a, 6.26b, and 6.27), distinguishing between MR powder samples made from the OCP and NCP is not feasible using SEM imaging. A similar comparison of 325-OCP and 325-NCP micrographs resulted in the same conclusion (Figs. 6.28b, and 6.28c). Although the 325 mesh iron powder used as the base of 325-NCP and 325-OCP was expected to be smooth and spherical, the particles shown in Fig. 6.28 have rough and uneven surfaces. The free zirconia particles collected through process ZrP1 were observed to be $\approx$ 100 nm flakes (Fig. 6.29c); similar particles were found adhered to the surface of the coated MR powder (batch 31B, Fig. 6.29d and batch 325-NCP, Fig. 6.28d).

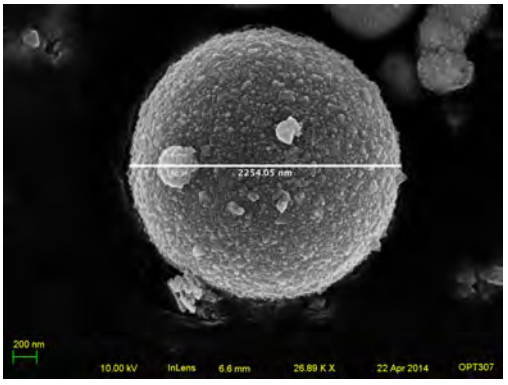

(a) Micrograph of a 2.33 µm diameter particle from batch 31B collected with the InLens detector at 10.0 kV.

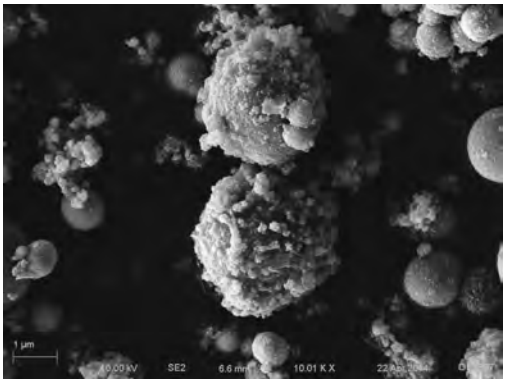

(b) A close-up view of two particles from batch 31B after zirconia separation process ZrP1. This micrograph was collected with the SE2 detector at 10.0 kV.

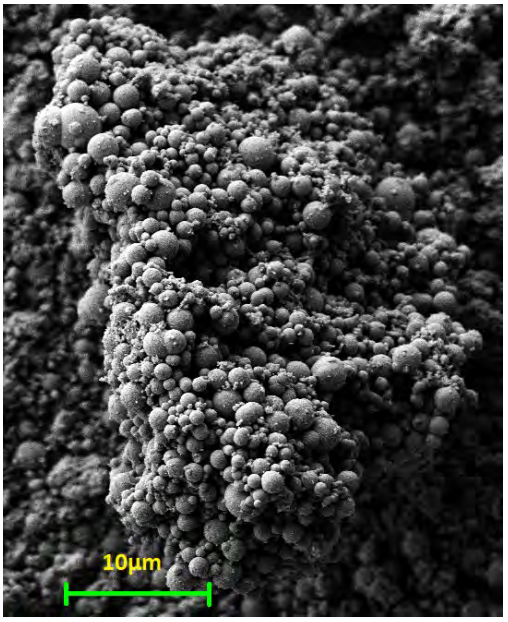

(c) A large clump of particles from batch 31B with a $3.5-0.25$ µm range in diameter. This micrograph was collected with the SE2 detector at 5.0 kV.

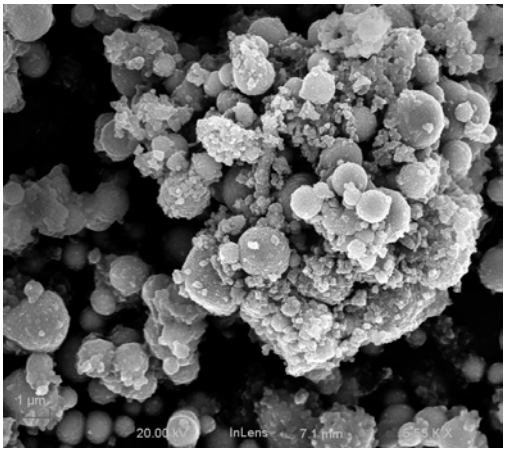

(d) A cluster of particles from batch 31B. The non-spherical agglomerations are suspected to be free zirconia particles. This micrograph was collected with the InLens detector at 20.0 kV.

Figure 6.26: Four SEM micographs of batch 31B powder samples that show a wide range in particle size, surface characteristics, and concentration of free zirconia agglomerations.

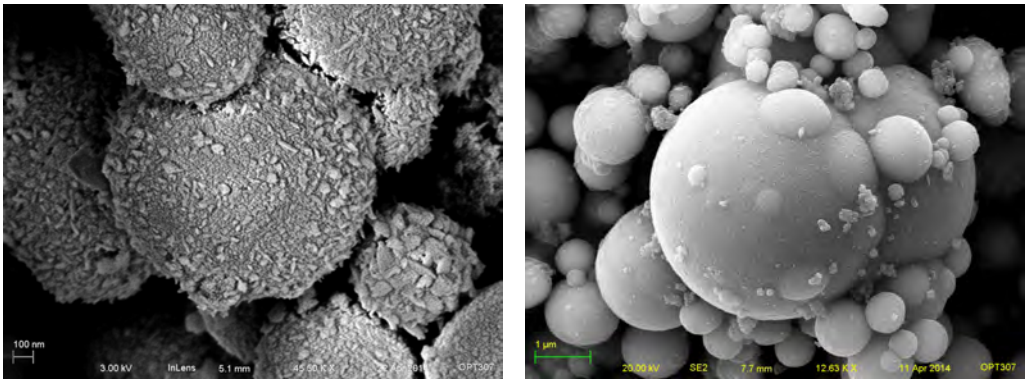

(a) Several small particles from batch HQ-Zr 4 collected with the InLens detector at 3.0 kV. The central particle is 1.38 µm in diameter.

(b) Several large particles the from batch HQ-Zr 4; this micrograph was collected with the SE2 detector at 20.0 kV.

Figure 6.27: Two SEM micrographs of HQ-Zr 4 powder samples showing a wide range in particle size, surface characteristics, and fewer agglomerations of free zirconia than Figure 6.26

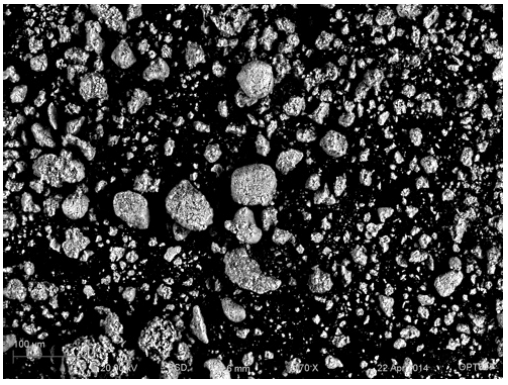

(a) A large field of view of 325-NCP particles. The four central particles are ≈ 45 µm in diameter. This micrograph was collected with the BSD at 20.0 kV.

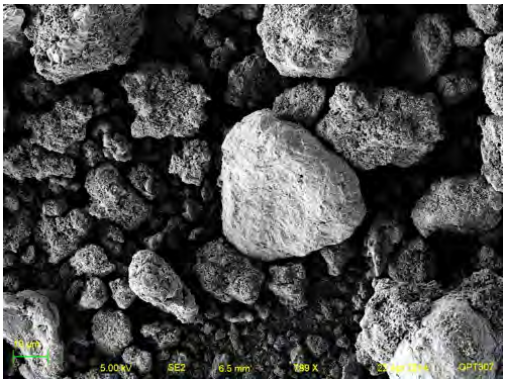

(b) Detail of 325-NCP particles. The central particle is 44 µm in diameter. This micrograph was collected with the InLens detector at 5.0 kV.

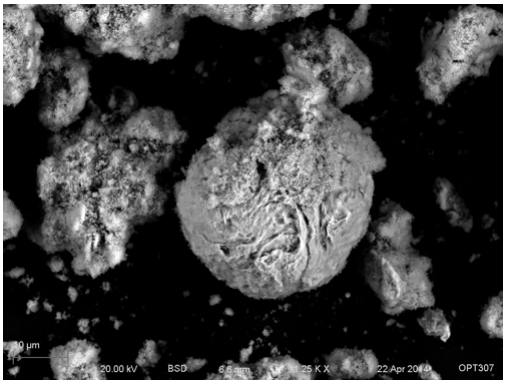

(c) Detail of 325-OCP particles. The central particle is 36 µm in diameter. This micrograph was collected with the BSD at 20.0 kV.

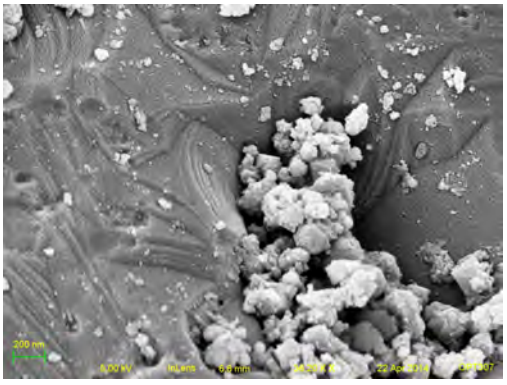

(d) Surface detail of a 325-NCP particle. This micrograph was collected with the InLens detector at 5.0 kV.

Figure 6.28: Four SEM micrographs of the 325 mesh coated MR powders displaying a 70 µm to > 1 µm range in particle size, with a range of shapes, and rough surface characteristics.

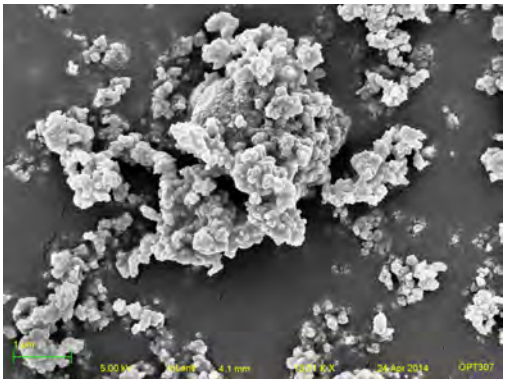

(a) A large field of view of an agglomeration of ZrP1 particles. This micrograph was collected with the InLens detector at 5.0 kV.

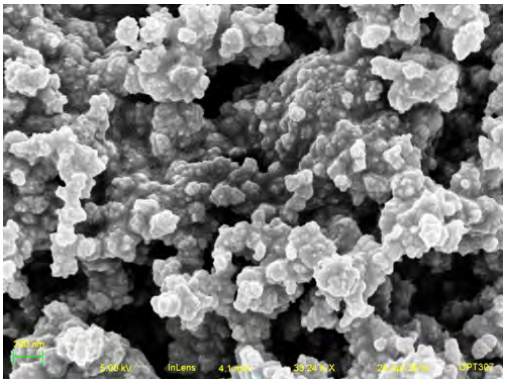

(b) Detail of an agglomeration of ZrP1 particles. This micrograph was collected with the InLens detector at 5.0 kV.

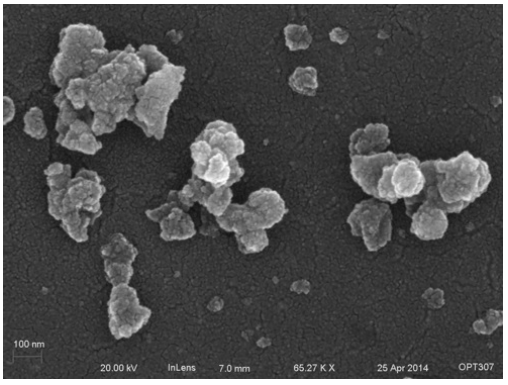

(c) Detail of smaller ZrP1 particles with diagonal lengths ranging from 452 nm to 196 nm. This micrograph was collected with the InLens detector at 20.0 kV.

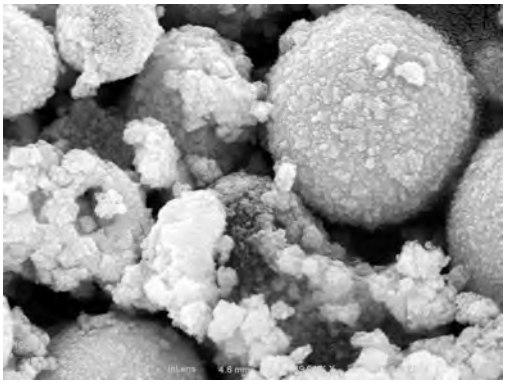

(d) Detail of free zirconia agglomerations resting on 31-B particles. This micrograph was collected with the InLens detector at 10.0 kV.

Figure 6.29: Micrographs of zirconia particles extracted via ZrP1. Figure 6.29c and the lower half of Figure 6.29d show the flake-like structure of the ZrO_2 particles.

Semi-quantitative information on the thickness of the zirconia coating on the NCP MR powders was obtained from SEM images of particle cross sections. Sample cross sections were prepared using the procedure outlined in Section 5.5.1. Micrographs of powder-cross sections were collected using a combination of the BSD and InLens detector. The InLens detector provides high resolution, while the BSD highlights regions of different

atomic composition. Micrographs of uncoated CI-HQ iron powder were obtained to serve as a comparison between coated and uncoated cross sections. The images in Fig. 6.30 show a clear transition between the iron powder and the epoxy. In contrast to the iron powder, the cross sections of powder from Batch 31B show distinct rings around the iron particle, which are due to the zirconia coating (Fig. 6.31). Because the BSD detector responds to primary electrons, and the intensity of primary electron signal increases with atomic number, the zirconia will appear darker than the iron. There is a significant range in zirconia coating thickness between particles; the central particle in Figure 6.31c has an average coating thickness of 197.7 ± 19.5 nm, while the coating thickness of the large particle in Figure 6.31d is 58.6 ± 9.8 nm.

(a) A micrograph of uncoated CI-HQ iron powder cross sections. The micrograph was collected with a mix of BSD and InLens detectors at 20.0 kV.

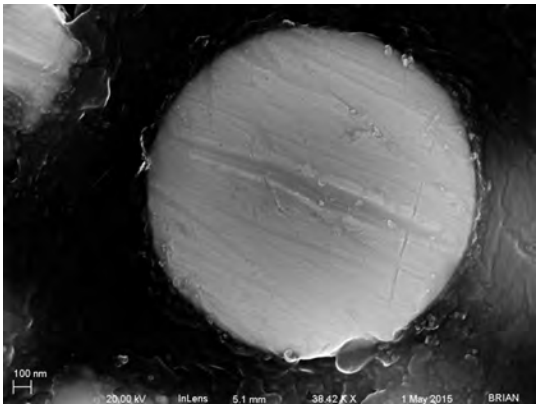

(b) A close up of a CI-HQ cross section highlighting the sharp distinction between the iron powder and epoxy. The micrograph was collected using a combination of both the BSD and InLens detectors at 20.0 kV.

Figure 6.30: Two micrographs of uncoated CI-HQ iron powder cross sections.

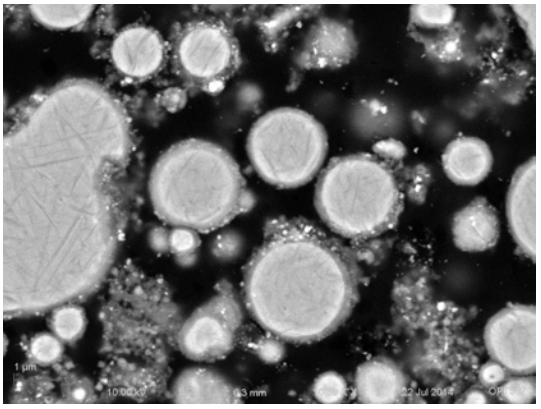

(a) A micrograph highlighting the variation in particle size and shape. The zirconia coating is visible as a darker ring around the iron particles. The micrograph was collected with BSD at 10.0 kV.

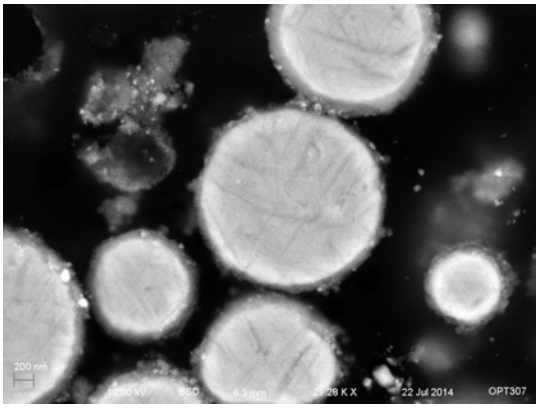

(b) The center particle has a mean coating thickness of 58.5 nm, while the top particle has a mean coating thickness of 137.4 nm. The micrograph was collected with the BSD at 10.0 kV.

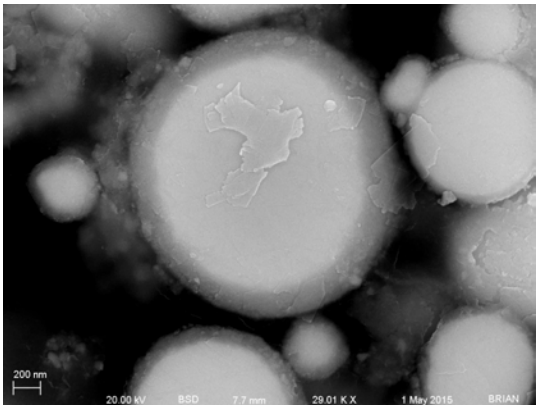

(c) A 2.0 µm diameter particle with an average coating thickness of 198 nm, calculated from the average of 38 line scans. The micrograph was collected using a combination of the BSD and InLens detectors at 20.0 kV.

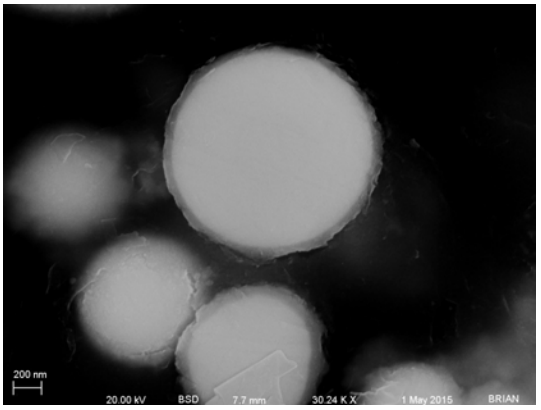

(d) A 1.5 µm diameter particle with an average coating thickness of 58.6 nm, calculated from the average of 42 line scans. The micrograph was collected using a combination of the BSD and InLens detectors at 20.0 kV.

Figure 6.31: Micrographs of cross sections of particles from Batch 31B. These images illustrate the large variability in the thickness of the zirconia coating on the iron powder.

6.8 MRF Powder Size Distribution

The particle size distribution of NCP MR powders was analyzed using the electrokinetic sonic amplitude (ESA) capability of the Colloidal Dynamics AcoustoSizer IIs. Analysis from eight powders show variations in both average particle size, and size distribution

(Fig. 6.32a). All reported measurements had zeta potentials under −25 mV, which is significantly removed from the isoelectric point (IEP) of the MRF powder [65]. The mean particle size was 2.46 ± 0.35 µm; the maximum D_{50} of the BASF CI-HQ powder specification sheet is 2.0 µm (Table 6.10) [61]. A D_{80} of 22.66 ± 4.87 µm suggests the presence of agglomerates that are $\approx 10\times$ the average particle diameter. The presence of large agglomerates implies the smaller agglomerates may also be present throughout the powder, which would increase the D_{50} particle size.

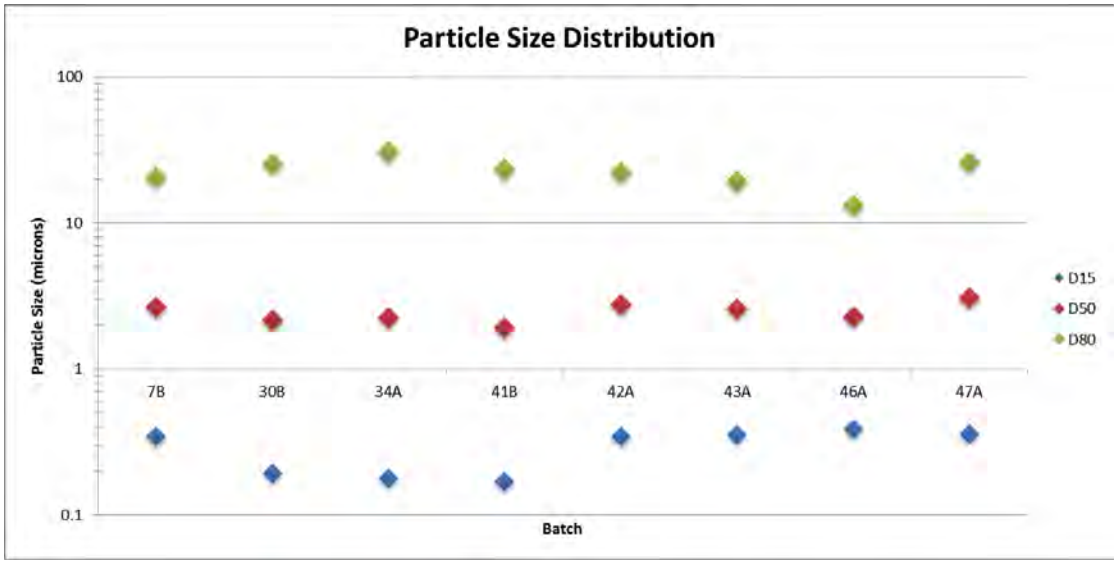

(a) A scatter plot displaying the D15, D50, and D85 particle sizes for a variety of MRF powders on a log scale. The powders were measured using the Acoustosizer IIs.

Table 6.10: Particle size distribution and zeta potential data of nine MRF powder batches measured with the Acoustosizer IIs.

Batch	D15 (µm)	D50 (µm)	D80 (µm)	Zeta Potential (mV)
7B	0.348	2.648	20.501	−34.2
30B	0.193	2.167	25.484	−27.0
34A	0.179	2.246	30.726	−28.1
41B	0.171	1.931	23.458	−34.4
42A	0.347	2.773	22.388	−28.3
43A	0.356	2.591	19.247	−27.9
46A	0.391	2.279	13.320	−46.9
47A	0.362	3.061	26.149	−32.8
Mean	0.293	2.462	22.659	−32.5
σ	0.088	0.346	4.867	6.2

6.9 pH Monitored Corrosion Test

Further corrosion tests were performed on the NCP MR powder both to determine the variability in corrosion resistance between batches and to refine the quality control procedure for future batches. The pH of acidic MRF slurries was recorded as a function of time. The trend line for each MRF powder batch in Figure 6.33a represents the average pH of four samples. The pH of most batches was ≈ pH 2.5 during the first 8.5 hrs; over the next 5.5 hrs the pH increased at a rate of ≈ 0.5 pH/hr. By the fifteenth hour, the pH had stabilized between 5.0 and 6.0. The transition from slurry stability to failure was defined as the point in time when the average pH reached 3.0 (Fig. 6.33a). The average time to failure for these slurries was 9.30 ± 0.69 hrs, with a 3.95 hr range between maximum and minimum failure time (Table 6.11).

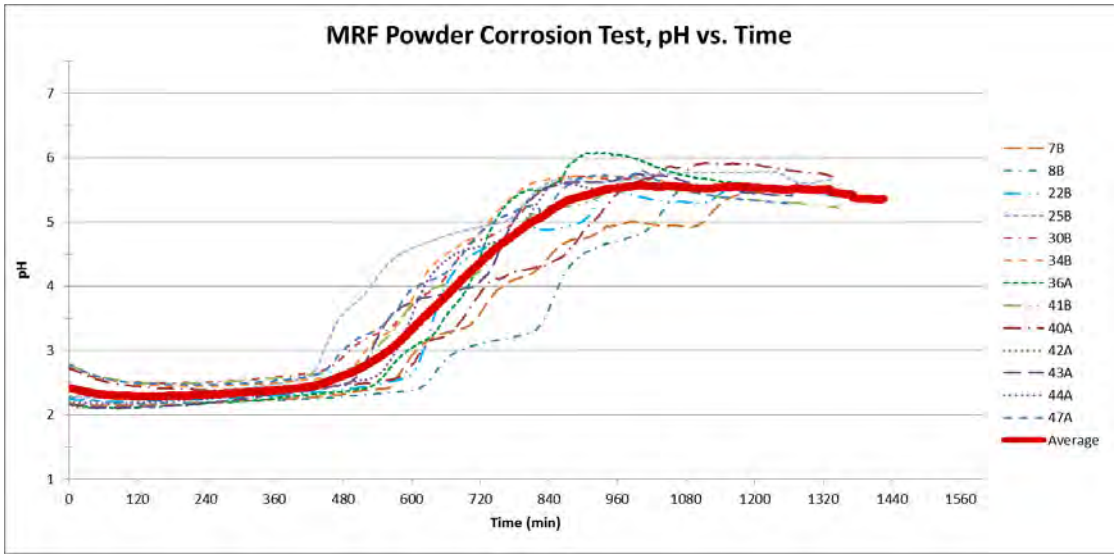

(a) Results of pH vs. time corrosion tests on 13 NCP MRF powder batches. The average for all results is highlighted with the red solid trend line.

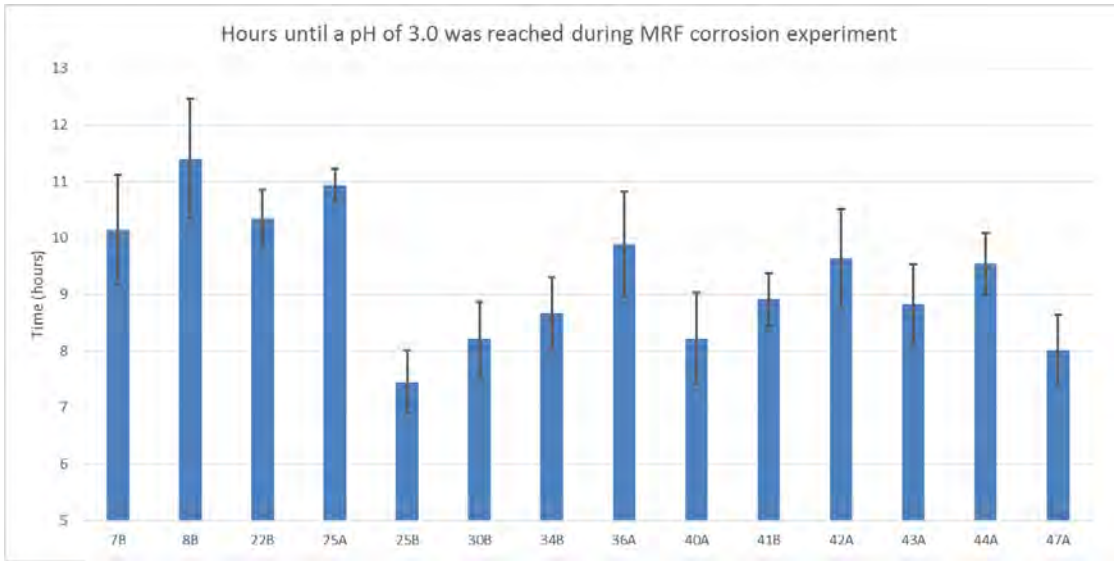

(b) Time until a pH of 3.0 was reached during the MRF corrosion experiment. Based on supporting data from other experiments, a pH value of 3 was considered the pH at which the slurry was no longer stable.

Figure 6.33: Results of stir-bar agitated, pH 2.5 glacial acetic acid MRF corrosion tests, measured in real time using Logger-Lite pH software and USB pH electrodes.

Table 6.11: Time to NCP MRF slurry failure during the pH-monitored corrosion test.

Batch	Corrosion (hrs)	σ
7B	10.15	0.97
8B	11.40	1.07
22B	10.35	0.51
25A	10.93	0.29
25B	7.45	0.56
30B	8.22	0.66
34B	8.67	0.64
36A	9.86	0.92
40A	8.22	0.81
41B	8.92	0.46
42A	9.63	0.88
43A	8.83	0.71
44A	9.55	0.55
47A	8.02	0.62
Average	9.30	0.69
Range	3.95	0.78

6.10 Summary

- X-ray diffraction was used to determine both phase and semiquantitative mass-fraction of species in MR powders:
  - Measurements using XRD confirmed the presence of an amorphous zirconia coating, and a high concentration of iron oxides in the iron core.
  - Scans were performed on unaltered samples and samples heat treated at 700°C.
  - Semiquantitative mass fraction analysis provided information on the ratio between iron and iron oxides and the concentration of zirconia in the MR powder samples.

- X-ray photoelectron spectroscopy, an analytical surface measurement technique sensitive between 3 - 30 nm, was used to characterize the surface composition of MR powders:
  - Issues with sample geometry significantly detract from the effectiveness of this technique.
  - Presence of an iron signal indicates portions of particle coatings are < 30 nm.
- Energy dispersive spectroscopy was employed to quantify the mass fraction of components in MR powders:
  - All measurements exhibited a significant carbon signal due to the carbon tape that the samples were adhered to.
  - Due to differences in sample geometry, there was a significant range in the carbon signal between samples.
  - This technique provided semiquantitative results, component mass fraction distribution was inaccurate.
- *The most successful analytical X-ray technique used in this work was found to be X-ray fluorescence*
  - *Results were highly repeatable,* $< 0.5\%$ σ *found in scans of 11 NCP MR powders*
  - *This technique provides semiquantitative mass fraction analysis, as oxygen cannot be detected in a standard atmosphere environment*

- The concentrations of iron and zirconia in the following samples measured using XRF are:
  - CIP: 99.97% Fe, 0.03% Zr
  - OCP MR powder: 85.41% Fe, 14.59% Zr
  - NCP MR powder: 70.69% Fe, 29.31% Zr
  - ZrP1 powder: 1.56% Fe, 98.44% Zr
- Zirconia concentration was estimated using a change in mass calculation (ΔMC) for the difference between initial and final powder mass (Table 6.6, pg. 118)
  - Dissolution of iron particles occurred when exposed to pH 1 sol-gel.
  - Calculations were derived from assumed loss of iron, from 0% - 15% during the coating process.
  - This calculation provided a reference point for the semiquantitative analysis obtained using X-ray techniques.
- Helium gas pycnometry was used to characterize CIP, OCP and NCP MR powder samples:
  - The lower densities seen in measurements of NCP powders (6.211 g/cm^3) confirmed the increased concentration of zirconia relative to the OCP MR powders (6.605 g/cm^3).
  - The NCP and OCP MR powders exhibit ~4x greater range in density results than CI powder, which suggests that inconsistencies are present in the coating procedure.

- Results from several analytical techniques were combined to improve the characterization of MR powder composition (Table 6.8, pg. 123).
  - Mass fraction data was obtained from analytical X-ray techniques, densities were obtained from pycnometry measurements, a theoretical density was calculated using both sets of data, a porosity term was added to provide an estimation of error.
  - Results from X-ray fluorescence measurements are similar to the values predicted by the ΔMC.
- The mass fraction of free zirconia in the bulk MR powder was measured at 0.28% when ZrP1 was used.
- Surface topography and morphology of MR powders were evaluated using SEM micrographs.
  - SEM micrographs revealed significant variance in surface characteristics of MR particles.
  - It is not possible reliably differentiate between OCP and NCP MR powder by relying solely on surface imaging.
  - Frequent occurrence of particle agglomerations suggests that formation occurs during the drying process.
  - The sample obtained using ZrP1 is similar to zirconia agglomerations on MR powder.

- SEM micrographs of MR powder cross sections were used successfully to image the zirconia coating:
  - MR powders were embedded in Stycast 1266 epoxy and polished.
  - A large variance in coating thickness was observed.
  - The NCP MR powder possesses a thicker ZrO_2 coating on average than OCP MR powder.
  - The maximum coating thickness observed on a NCP MR particle was 200 nm.
- The electrophoresis method was used to determine the particle size distribution powder samples.
  - Zeta potential and particle size analyzer (Acoustoizer lls) was used to determine particle size distribution:
  - The average particle size was 2.5 μm.
  - D80 particles $\sim$ 10x larger than the manufacture's specifications of 2 μm indicates that large agglomerations are formed during MR powder drying process.
- Continuous pH monitoring during the accelerated corrosion test quantified the time of slurry destabilization.
  - The 16TC-FF corrosion experiment relied on observation of foam developing in the samples.

- Slurries remained stable at pH ∼2.3 for ∼560 min.
- Significant variance in corrosion times were observed (Fig. 6.33, pg. 134).
- This technique allows corrosion experiments to use the same acid as is used in the MR slurry.

Chapter 7

Discussion

7.1 Introduction

Research on the application of MRF to the polishing of free-form CVD ZnS optics lead to the development of alkaline MR slurries based on zirconia-coated CI-powder. These slurries posses the capability of high material removal rate along with long-term slurry stability [5]. Salzman et al. introduced a further modification to the MR slurry by adjusting the pH to the acidic region, taking advantage of both chemical etching and mechanical removal of the CVD ZnS surface [6, 66]. The acidic pH slurries employing the zirconia-coated powder exhibited greater stability when compared to the acidic slurries composed of uncoated CI-powder produced by Kozhinova et al. [3, 6, 38]. However, zirconia-coated CI-powder based slurries still showed a tendency to increase in pH at

the rate of ∼0.5 pH per day [6]. The instability in pH indicates that some oxidation of the CI powder is occurring, in spite of the presence of the protective zirconia coating.

The work presented in this thesis was focused on: (1) further increasing the corrosion resistance of zirconia-coated CI-powder; and (2) developing a procedure to characterize the composition and morphology of the coated MR powder. Many techniques were employed in order to gain a more complete understanding about the morphology and structure of zirconia-coated MRF powder. Corrosion resistance, particle size distribution, species concentration and coating thickness were all measured. In this section, the relative success of each technique is discussed and recommendations are made for a future protocol for MR powder quantification.

7.2 Corrosion

The primary objective of this work was to alter the MR powder, to produce an increased stability in the acidic (pH 4.0) slurry. A key element to this end was to develop a rigorous corrosion testing procedure. Prior to the execution of the full factorial experiment, a reliable corrosion test was developed to provide a testing environment for all MR powders that were produced. Initial experimental design ideas were adapted from Shen et al. who employed a semi-quantitative test to define the onset of corrosion [4]. Constraints included: minimizing the use of coated powder, quantitatively defining corrosion time, locating and determining an acidic concentration that would increase the duration of the coated particles in acidic slurries to 12 hrs or longer.

7.2.1 Preliminary Corrosion Experiments

The initial corrosion experiments were performed to determine an appropriate acid species and concentration such that oxidation of the coated particles would be observable within ∼8 hrs. Several new batches of MR powder were produced, with some variations to the drying procedure (3.3.1 pg. 22). These samples were intended to be evaluated and compared to OCP MR powders created in 2009 in addition to uncoated CI powder samples. Phosphoric, nitric, hydrochloric, and acetic acids were surveyed. The use of phosphoric and hydrochloric acids was abandoned because of their extremely rapid oxidation and high reactivity with all powder samples.

Nitric and acetic acid-based slurries were examined further for their corrosion resistance at low pH and indication of the onset of corrosion. Coated powder samples dispersed in a pH 2.0 acetic acid solution exhibited a ±0.2 drift in pH over 5 hrs (Fig. 3.11a). Similar dispersions in a pH 2.0 nitric solution showed a rapid increase in pH to ∼8 in under 20 minutes (Fig. 3.11b, pg. 33). In slurries with dilute acetic acid, an increase in pH was accompanied by the production of large amounts of foam (Fig. 3.8 on page 29). There were no qualitative changes in the nitric acid-based dispersions that corresponded with changes to the pH. These findings led to the selection of acetic acid for the remaining corrosion tests (although nitric acid contained in the MRF slurries used in the STM).

Constant slurry agitation was an important addition to the corrosion testing process. The samples in the first three corrosion experiments were only agitated once or twice hourly. Observation of sample corrosion immediately following agitation indicated that

stagnant samples corrode more slowly than samples that are continuously agitated (Subsection 3.3.1.3). This phenomenon may be caused by an accumulation of Fe(ii) and Fe(iii) ions at the anodic sites of oxidation. In a stagnant environment, the iron oxides may partially or completely cover the anode (the exposed surface of the carbonyl iron particle), slowing the rate of corrosion. Once the sample has been agitated and the anodic surface has been exposed, the rate of corrosion would increase. All samples in the proceeding experiments were exposed to steady agitation with magnetic stir-bars, which decreased the corrosion times variance and more accurately simulated the environment of the STM, in which slurries are exposed to constant mixing for up to three weeks [5, 6].

7.2.2 Corrosion Experiments on 16TC-FF Powders

The slurries prepared for this experiment were dispersions of 6g MR powder in 8.3 mL of a 50:50 acetic acid and DI water solution agitated by magnetic stir-bar in 50 mL beakers. Five samples were prepared for each batch and placed in randomized locations on the magnetic stir-plates to minimize the impact of any environmental variations in the fume hood. Samples closer to the front of the fume hood were exposed to a slightly faster air current, which may have slightly increased evaporation during the corrosion testing process. Batch testing order was also randomized to reduce the impact of any potential changes in the laboratory environment.

Slight alterations to the original corrosion testing procedure became necessary during the experiment. The magnetic stir-bars used for testing the first two batches were not uniform. Although this factor did not appear to alter the corrosion time, all following

batches were mixed using a single type of stir-bar. With a standard deviation of ∼25% average corrosion time, it was very important to minimize experimental variation. The variation in angular velocity between locations on the initial stir-plate was noticed after seven batches had already been tested. Although it is possible that the difference in stir-bar RPM had an effect on corrosion time, there is only a 11 min difference between the average standard deviation of batches exposed to a consistent RPM (109 min.) and those that were not (98 min.). The remaining 19 batches were tested at a constant 350 RPM.

The timed camera program employed to photographically document the experiment overnight was set to take pictures at 15 minute intervals. This large photographic interval for visual corrosion onset documentation implies that the corrosion times of some of the five samples per batch could be off by as much as 15 min. Assuming that the corrosion time for each sample in a batch was off by 15 minutes, with an average corrosion time of 4.5 hours (Table 4.4, pg. 44), then a variance of ±15 min only introduces an error of ∼5%. On rare occasion, a sample would not foam at the onset of corrosion, but would instead thicken and harden. For these samples, corrosion was defined as the time at which the stir-bar RPM was visibly slowed; reduction in RPM is also visible in the photographs. These samples were used in the calculation of corrosion time, as the thickening of the slurry occurred within the range of the other samples. The reason why some samples did not foam, prior to thickening, is unknown at this time.

7.2.3 Corrosion testing of NCP MRF powders

The final set of corrosion tests were performed on fourteen NCP MR powders to test for consistency of corrosion resistance between batches. Five samples per batch were tested. The mass-fraction of the powder and solution composition were both maintained at the values used in Subsection 3.3.3. All dispersions were mixed at 350 RPM and the beakers holding the samples were covered with Parafilm to minimize evaporation.

The pH of each sample was measured once per minute with pH probes (Vernier Brand [56]), connected to a laboratory computer through a USB interface. This equipment allowed quantification of the onset of slurry pH instability, whereas previous experiments relied on observation of foam production to indicate slurry failure. A pH of 3.0 was defined as the onset of instability. The four hour range in the failure onset time is not well understood. Slurries with a high concentration of particles with a thinner zirconia coating, as shown in SEM micrographs of particle cross-sections (Fig. 6.31d, pg. 131), are a likely cause for their decreased corrosion resistance. It is not apparent whether this faster oxidation rate was due to a variation in the manufacturing of the batch, an error in the experimental procedure, or a higher concentration of particles with a thinner than average zirconia coating. The latter appears to be the most plausible, as a significant range in the standard deviation of corrosion times has been observed throughout all iterations of corrosion experiments presented in this work.

7.3 4F-16TC-FF Corrosion Experiment

The 16TC-FF experiment was designed to ascertain which steps in the production of OCP MR powder should be altered to increase the MR powder's corrosion resistance. Two-level factors, each possessing two distinct settings to be tested, were chosen for this experiment. These factors were selected to cover distinct portions of the manufacturing process. Pre-milling the CI-HQ powder before the coating process (yes / no) was chosen to investigate the hypothesis that agglomerations existed in the iron powder. It was suspected that coated agglomerations existed in the final product that break up during MRF. The now uncoated CI particles would be exposed to the acidic slurry, rapidly corrode, and induce further oxidation in the slurry. The order of components added to the zirconia sol-gel was also tested, either: nitric acid was added before zirconium butoxide (old method), or zirconium butoxide was added before nitric acid (new method). This factor was selected to investigate the effect that changing the zirconia sol-gel chemistry had on the corrosion resistance of the coating. The volume fraction of the sol-gel in the coating procedure was the factor selected for the coating process, rather than exploring the synthesis of a new sol-gel. The volume fraction of sol-gel in the coating procedure was increased from 40 vol% to 60 vol% to determine if an increase in the sol-gel concentration during the coating process result in a more robust coating. Alteration of the powder drying temperature was chosen for the final factor: increased drying temperature, or maintained at the initial value.

A full factorial 16-TC experiment was selected to provide the capability of identifying

significant factors and factor interactions. The 8-TC design was also considered. With half of the treatment conditions, the 8-TC experiment would have been completed in less than half of the time required for the 16-TC, as there was only room in the fume hood to perform either corrosion testing or manufacture the MR powder at one time (but not both). However, the 8-TC design is limited to three factors to produce a full factorial resolution. While the resolution IV experimental design accommodates four factors, the second level interactions are confounded, and no information can be obtained from them [47].

Results from the ANOM show that sol-gel concentration, sol-gel preparation method, and drying temperature are all significant factors. The most influential factor setting is the increased sol-gel concentration from 40 vol% to 60 vol%, which indicates that higher sol-gel concentration during the coating process yields particles with higher resistance to oxidation than those found in the OCP powder. X-ray fluorescence measurements of these powders exhibit a Zr signal that is approximately twice the intensity of MR powders made with the lower concentration of sol-gel, which verifies that those powders have a much higher concentration of zirconia. Additionally, procedure ZrP1 yielded less than 1% mass of free zirconia. In light of these results, a conclusion can be drawn that the MR powders manufactured with higher concentrations of sol-gel posses a thicker zirconia coating.

In the initial procedure developed by Shen et al [4], nitric acid was added before zirconium butoxide during sol-gel synthesis; no explanation was given for this choice. Alterations to the sol-gel synthesis process were investigated to determine whether or not

altering the chemistry of the sol would increase the corrosion resistance of the coating. The results from ANOM and ANOVA confirm that addition of zirconium butoxide prior to adding nitric acid results in an increased resistance to oxidation. When added to acidic aqueous solutions, the alkoxide becomes protonated and hydrolyzes, resulting in the formation of a Zr-O-Zr bridge between two Zr alkoxide molecules. This process continues between adjacent Zr alkoxide molecules with the formation of a Zr-O-Zr polymer [1]. For zirconium alkoxides in acidic solution, the rate of hydrolysis is much faster than the rate of condensation [67]. If the hydrolysis reaction rate proceeds too quickly, the remaining zirconium alkoxide will stay in solution as hydrolyzed zirconium alkoxide and not condense to form a zirconia layer on the surface of the iron powder. It is possible that the rate of hydrolysis of the zirconium alkoxide is slowed when dispersing the butoxide in DI water before the nitric acid. Most sources from the literature suggest using an alcohol or other complexing agent that will modify the alkoxide and the slow hydrolysis rate [1, 67–69]. The lack of any complexing agent in the sol-gel process is not explained in the zirconia-coated MR powder literature. Further study of sol-gel chemistry is recommended to optimize the coating process.

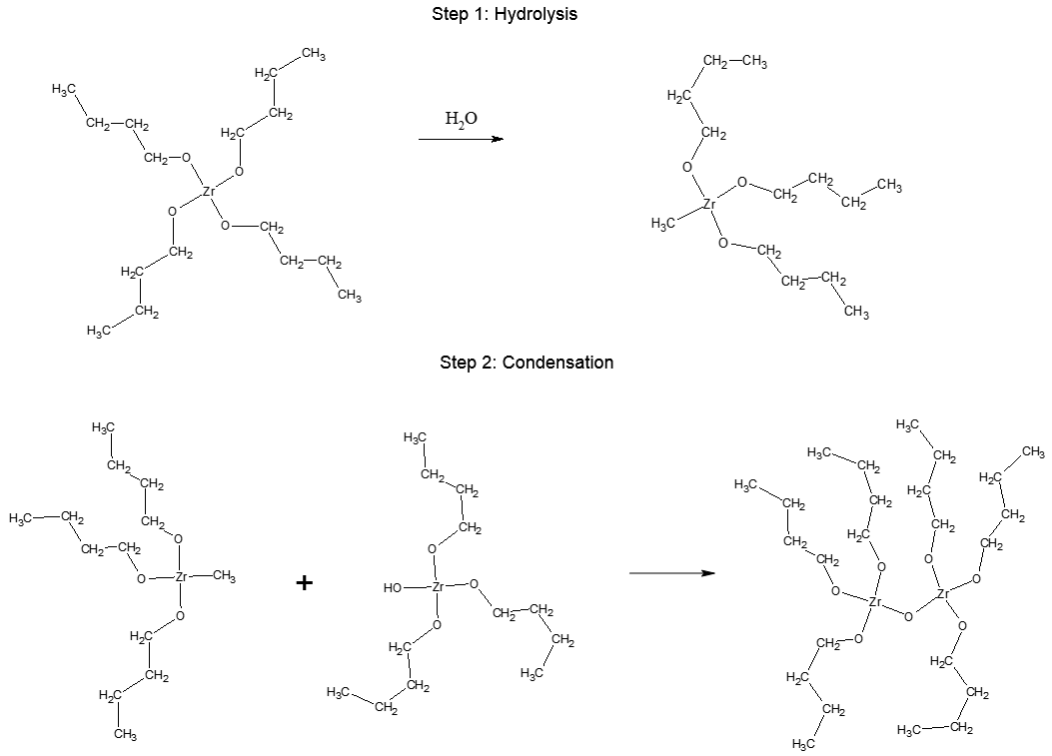

Figure 7.1: Illustration of the sol-gel transition. Information for this figure was obtained from Shane and Mecartney [1].

It was hypothesized that reducing the time that the MR powder was exposed to the acidic sol-gel by increasing the drying temperature, would improve corrosion resistance. However, ANOM and ANOVA data revealed that MR powders dried at 100°C oxidized more rapidly than those dried at 60°C. The lowered corrosion resistance of powders dried at 100°C suggests that the integrity of the coating is damaged by drying at the higher temperature. No explanation for this behavior was found in the literature. One possible explanation is that the increased temperature and rate of drying produced microcracks in the zirconia coating; another is that the evaporation of water produced by drying at 100°C in a vacuum creates micro-pores in the coating.

Milling of the CI powder prior to sol-gel coating had no impact on the corrosion resistance of the MR powder. This finding indicates that either agglomerations are not present in the powder or they do not have an impact on the rate of oxidation, whether or not they broke apart and exposed the CI-HQ.

The results of the four factor 16-TC FF corrosion experiment, ANOM, and ANOVA were used to determine a new MR powder manufacturing procedure. The 'best' factor settings were chosen for the NCP, these factors were: increased sol-gel concentration, altering the sol-gel synthesized by adding zirconium butoxide before nitric acid, a 60°C drying temperature, and pre-milling of the iron powder. Although pre-milling was not considered to be significant step according to ANOM and ANOVA, it was added to the NCP because of the small positive effect it had according to ANOVA.

7.4 Powder Analysis

After the NCP had been determined, a wide variety of MR powders and powder components were analyzed. There were three goals for powder analysis: (1) develop a procedure to quantify powder composition; (2) determine the thickness of the amorphous zirconia coating; and (3) determine the mass-fraction of free zirconia in the NCP MR powder. The pros and cons of various analytical techniques are presented in this section and recommendations for future MR powder are also introduced.

7.5 Analytical X-ray Techniques

Five X-ray techniques were used to analyze MR powders: XRD, XPS, XRF, XRM, and EDS. This survey was performed to identify which methods were suitable for measuring the quantitative mass-fraction of powder components, the powder coating thickness, and oxide concentration. Quantitative analysis of zirconia-coated MR powder presents several intractable difficulties, which include substantial variance in particle size, sample inhomogeneities, free space between particles that attenuates both the photon beam and the detector signal, the interaction volume of the incident X-ray can be larger than the particle, and signal from the coating is increased by attenuation of the iron-core signature by the zirconia coating.

X-ray diffraction has been used to determine both phase and semi-quantitative mass-fraction of components in a variety of powder samples. Short and long duration scans (1.5 and 7.4 hrs respectively) were performed on unaltered and heat-treated samples. Initial short scans of unaltered samples were performed on MR powders to ascertain both the phase of the zirconia coating, and the concentration of pure and oxidized iron. Analysis of results confirmed the amorphous nature of the zirconia. While the traditional approach of measuring the amorphous content in a sample consists of calculating the area under the broad amorphous peak, this process becomes impractical when there are multiple phases within the sample, and when the mass-fraction of the amorphous material is small [70, 71]. Additionally, the semi-quantitative algorithm in X'Pert Highscore [49] software uses the Normalized Reference Intensity Ratio (RIR) method, which is incapable of

computing the mass-fraction of amorphous materials[72]. The low temperature scans of MR powders showed 53-57% Fe and 47-43% Fe_3O_4 concentrations. Identification of iron oxide species was important for the calculations performed in Section 6.5, as there is a significant range in the densities of Fe(ii), Fe(iii), and Fe(ii,iii).

Scans of ZrP1 showed broad amorphous peaks and iron oxide signatures, which suggests that the powder collected from ZrP1 is either composed of coated iron particles with a magnetic potential too small to be attracted by the magnets during the separation process or that iron oxides were dispersed in the colloid. Scans of ZrP3, also produced amorphous peaks with magnetite and maghemite signatures; this result was expected, as some iron powder is lost when the sol-gel is decanted during the wash process. Low temperature scans of ZrP2 were matched with nitrammite ($NH_4[NO_3]$), although it is unclear if this is the actual structure of the powder as all of the species are present in the sol-gel. The powder sample had evaporated from the crucible after the half hour exposure to the 700°C oven, indicating that no zirconia remained in the sol-gel solution during the powder coating. This results suggests that the sol-gel coating process leads to the succesfull adsorption of nearly 100% of the zirconia onto the CI-HQ powder. Further corroboration of this finding can be seen in the low concentration of free zirconia in the bulk powder (Section 6.6).

Work done by Tyagi et al. indicates an amorphous-to-crystalline phase change in the zirconia may be induced by heating the sample to 450-700°C [73]. Scans of samples that had been placed in a 700°C oven for half an hour did display ZrO_2 signatures, enabling the use of HighSchore's Semi-Quantitative Analysis Algorithm [49]. For the

OCP powders, a concentration of 4% ZrO_2 was measured with a 1.5 hour scan, and 7% ZrO_2 was measured with the 7.4 hour scan, almost doubling the measured quantity. The NCP powder's zirconia concentrations measured with the short and long scans were 7% and 9% respectively. Scan duration precluded further investigation of variance in the semi-quantitative results. Tesults from Table 6.8 indicate that the semi-quantitative data provided by XRD is not an accurate depiction of the concentration of species in the coated MR powders.

The attempt to use EDS to obtain quantitative mass-fraction data was not successful. Powder samples were adhered to carbon tape and either sputter coated with gold or exposed to carbon evaporation. Gold coating of the samples was necessary in order to eliminate surface charging from the electron beam. Unfortunately, both the carbon tape and the coating produced strong background signals that greatly reduced the accuracy of results.

The SEM's EDaX detector was used to produce X-ray maps of three powder samples: (1) carbon coated NCP MR powder adhered to carbon tape; (2) cross-sections of gold coated 44 µm NCP powder embedded in a thermosetting epoxy puck; and (3) carbon coated ZrP1 particulate on carbon tape. The X-ray mapping technique produced limited success when applied to the characterization of MRF powder samples, although maps were generated that confirmed the presence of iron, oxygen, and zirconia in the samples (Fig 6.19 – 6.21). The map of ZrP1 demonstrated the success of the separation technique (Fig 6.21). To produce sufficient signal, a voltage of 20.0 KeV was used [58]. With an

acceleration voltage of 20.0 KeV, the lateral resolution of EDS is ~ 1 µm [74], which is too low to capture the sub-micron characteristics of the zirconia coating (Fig 6.20d).

X-ray photelectron spectroscopy has been used to confirm the presence of oxides in the MRF powder samples, and the iron signature in the scan results indicate that a portion of the particles have a coating thickness < 20 nm. This result is supported by SEM micrographs of MR powder cross-sections (Fig. 6.31), which show significant variance in coating thickness. This technique has confirmed the success of ZrP1 in collecting free zirconia from the bulk MRF powder. However, there is a large variability in results when a monolayer of powder is analyzed (Fig. 6.23). The ±10% variability in concentration of carbon and oxygen when measuring similar samples (Table 6.4), combined with the difficulty in removing background noise, indicate that XPS is not ideal for the characterization of MR powders. As XPS is ideally applied to the measurement of thin films [51], it may be useful to deposit a zirconia sol-gel coating on a macroscopic iron sample for analysis by XPS. By measuring the zirconia-coated macroscopic iron sample, film thickness could be calculated using Equation 7.1 [75]:

$$t_{ZrO_2} = cos\,\theta \frac{\lambda_{ZrO_2}(E_1)\lambda_{ZrO_2}(E_2)}{\lambda_{ZrO_2}(E_1) - \lambda_{ZrO_2}(E_2)} ln \frac{I'_{Fe}(E_1)}{I_F e'(E_2)} \tag{7.1}$$

where t_{ZrO_2} is the thickness of the zirconia coating, and $\lambda_{ZrO_2}E_i$ is the attenuation length of Fe photoelectrons, with kinetic energy E_i, in the zirconia coating. The energies E_1 and E_2 are sufficiently different to exhibit a difference in attenuation length (λ). For iron, Fe 2s (640.6 eV) and Fe 2p (776.6 eV) would be good candidates for E_1 and E_2.

The emission angle of the electrons with respect to the surface normal is θ. The corrected substrate intensity [76] $I'_{Fe}(E_i)$ is the measured intensity of Fe photoelectrons at kinetic energy E_i. However, this method makes the assumption that the transition between coating and substrate are abrupt [75]. The presence of iron oxides at the zirconia / iron interface may invalidate this assumption. It is possible that the iron oxide layer is small enough to not significantly impact on the measurement. The location of iron oxides in the MR powder were not identified in SEM micrographs of particle cross-sections.

With regards to ease of data collection, and accuracy of results, XRF was the most successful quantitative analysis technique. Sample measurements were obtained in 180 seconds (approximately 150 times faster than XRD scans, and ~100 times faster than XPS scans). Without placing the samples in a vacuum, it is impossible to obtain a signal from oxygen, due to low energy of oxygen's K_α [77]. Mass-fraction analysis with XRF would be simplified if oxygen signals were obtained, as a fraction of the measured oxygen signal is from ZrO_2 and the remaining fraction originates from the iron oxides. Large concentrations of an undetected element will also alter the calculated results, by lowering the apparent average atomic number of the sample [60]. For this reason, the measured concentration of Zr via XRF is likely overestimated due to its presence on the surface and the lack of oxygen detection.

Scans of eleven NCP powders yielded very consistent results; $< 0.5\%$ deviation in atomic concentration for iron and zirconium was found (Table 6.5). Similar results were obtained from eight measurements of OCP MR powders. This low variance suggests that there is little variation in atomic concentration between batches. No sample preparation was

required, which is another significant advantage of XRF over EDS and XPS. Results of XRF scans appear similar to ΔMC calculations (Table 6.8), although the XRF of the coated MR powders appears to overestimate the concentration of zirconia. Further work would be required to develop a calibration to better account for the decrease of the iron signal due to the zirconia coating. Attempts to make such a calibration curve failed during this experiment. Compositions of the powder samples were disparate, containing high concentrations of either iron or zirconia, with no samples having nearly equal iron and zirconia concentrations.

It may be possible to create a calibration using samples composed of a known concentration of uncoated CI-HQ, magnetite, and ZrO_2 powder. The ratio of CI-HQ to magnetite in the zirconia-coated MR powder has been obtained from XRD measurements [53% iron powder and 47% magnetite for NCP MR powder (Figure 6.5), and 57% iron powder and 43% magnetite for OCP MR powder (Figure 6.2)]. The iron-magnetite ratio and zirconia concentration would be adjusted to produce an XRF spectrum equivalent to an NCP MR powder spectrum. The densities of these two powders would be measured, and a calibration powder produced from the CI-HQ, magnetite, and ZrO_2 with a density matching the NCP MR powder. Measuring the calibration powder by XRF would produce a spectrum representative of the concentrations of species in the powder, correcting for the increased zirconia signal seen in the XRF scans of NCP MR powder. The difference between the XRF spectra of the NCP MR powder and the calibration powder would be used to create a correction factor, which could be used to determine the mass-fraction of other zirconia-coated MR powders.

No distinguishing characteristics were found between SEM micrographs of OCP and NCP MR powders; both materials exhibit a range in surface characteristics (Figs. 6.26 pg. 126, 6.27). Irregular agglomerations of zirconia tend to adhere to the surface of coated particles (Fig. 6.26b) due to the similarity in appearance to SEM micrographs of ZrP1 particles (Fig. 6.29). These agglomerations may break free of the particles during the polishing process, adding to the concentration of free zirconia in the MRF slurry.

The Stycast 1266 epoxy pucks were much more successful in revealing the ZrO_2 layer thickness of coated MR powders than the Buehler thermosetting epoxy. Polishing the Stycast pucks produced a smooth, even surface, while the polished Buehler ProbeMet thermosetting epoxy [78] pucks had an uneven surface profile. The thermosetting epoxy contains Cu, Si, and Al particles ranging in size from $\sim 5-60$ µm. This created separate domains of epoxy and MR powder due to the differences in particle size (Fig. 7.2). Only the particles on the edges of the epoxy particle 'islands' displayed cross-sections. Additionally, the inhomogeneous distribution of the thermosetting epoxy components made locating the cross-sections coated MR powder difficult. The uniform Stycast 1266 epoxy sample made locating and measuring the cross-sections much easier. Cross-sections of NCP MR powder embedded in Stycast 1266 epoxy revealed the zirconia coating, which appears as a darker ring surrounding the iron core. A significant range in coating thickness (58.6 nm ±9.8 nm and 197.7 nm ±19.5 nm) was found in NCP MR powder (Fig. 6.31). By analyzing additional SEM micrographs of particle cross-sections with image processing software such as ImageJ, a mean coating thickness could be determined. The cause of this range in coating thicknesses during sol-gel coating of the CI powder has

not been investigated.

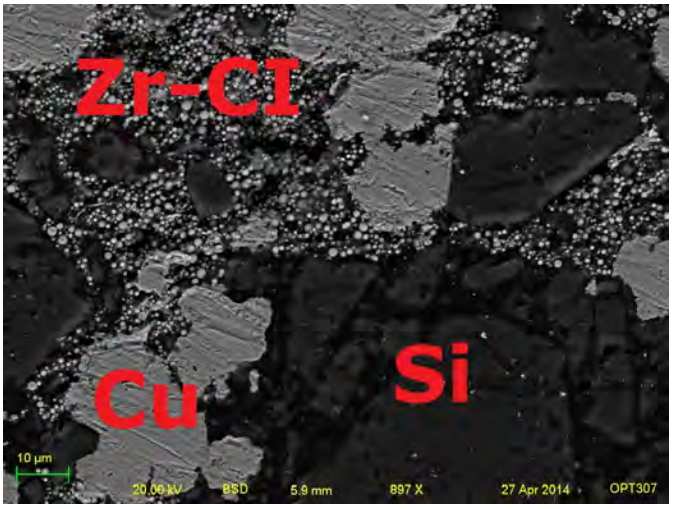

Figure 7.2: A SEM micrograph of zirconia-coated MR powder embedded in a Buehler ProbeMet thermosetting epoxy puck, collected with the BSD at 20.0 kV.

7.6 Physical Measurement Techniques

Several methods were employed to ascertain information about the physical characteristics of OCP and NCP MR powders; these methods included helium gas pycnometry, magnetic separation of free zirconia, particle size distribution, and changes in powder batch mass throughout the coating procedure. Many of these techniques were used to provide a reference point for the results of X-ray mass-fraction analysis.

The ΔMC of the powder compositions was a simple method of determining the zirconia concentration to $\pm 10\%$. In combination with density analysis, this method was used to check the accuracy of quantitative elemental analysis (Section 6.5). Loss of small amounts of powder during the coating process reduces the precision of this calculation.

There are three parts in the coating procedure where powder can be lost; during (1) decanting of the sol-gel supernatant and wash process (Figure 3.3b, pg. 19); (2) transfer of the powder from the ceramic funnel to an aluminum foil covered petri dish (Figure 3.3d); and (3) during transfer from the mortar to the lidded plastic storage cup (Figure 3.3g). Although the amount of powder lost during these three steps is likely < 5 g, it does reduce the precision of the mass-based species concentration (Section 6.3, pg. 117).

One assumption made for this calculation was that the mass of iron is reduced due to ionization and corrosion when exposed to the $\sim$ pH 1.0 sol-gel. Confirmation and quantification of the loss of iron may be possible by performing the coating procedure without the sol-gel. Because there would be no increase in mass from the zirconia, the difference between initial and final powder mass should be exclusively due to the loss of CI-HQ during the process. Some consideration would have to be given to the design of this experiment, since under normal coating conditions zirconia is adsorbed onto the surface of the CI powder once the sol-gel is added to the mixing vessel, which will reduce the rate of corrosion and ionization of the CI powder.

Helium gas pycnometry proved to be a very useful technique for the characterization of the zirconia-coated MR powders. The lower densities seen in measurements of NCP powders confirmed the increased concentration of zirconia relative to the OCP MR powders. The density analysis results were successfully combined with: XRF, ΔMC, XRD, and EDS data to estimate the atomic concentration of the species contained in the coated powder.

Results from iron powder measurements were precise [for seven samples, $\sigma = 0.056 \frac{g}{cm^3}$ (Fig. 6.25a and Table 6.7)]. The precision in these measured results indicates that the procedure described in Section 5.3 does not introduce significant experimental error. The OCP and NCP MRF powders had ranges in density of $0.630 \frac{g}{cm^3}$ and $0.573 \frac{g}{cm^3}$, approximately four times greater than the range in iron powder densities (Fig. 6.25). The range in measured densities of the coated MR powders suggests there is either inhomogeneity in density between samples or variations in the average batch density. The density of the powder decreases with particle size due to the increase of the zirconia-iron volume ratio. A particle size distribution that is not representative of the batch average would alter the measured density of the powder. The lower average density of NCP MR powders as compared to OCP powders implies an increased concentration of zirconia.

Densities of ZrP1 and ZrP3 were not measured, as not enough sample powder was present to perform the measurements. The density of ZrP2 was not measured because the XRD results showed that this sample possessed no zirconia. The measured density of ZrP4, powder obtained from the calcination of zirconia sol-gel at 100°C, was $2.462 \pm 0.001 \frac{g}{cm^3}$. This measurement is much lower than the density of ZrO_2 ($5.76 \frac{g}{cm^3}$)[62], indicating that the calcination temperature was too low to remove the residual organic components from the sample.

An important component of MRF slurries is the presence of the proper proportion and type of nonmagnetic abrasives that can increase material removal rate and reduce the PV and RMS roughness of the finished surface [3, 42]. Nanometer-scale nonmagnetic

abrasives are pushed to the surface of the MRF ribbon and remove material in conjunction with the larger magnetic coated particles. A goal of this work was to determine if the NCP MRF powder contained enough free zirconia particles to alter the amount of added abrasives to the MRF slurry.

Procedure ZrP1 was used twice to collect free zirconia from MRF powder (Subsection 5.2.1, pg. 56). The mass-fraction of the initial sample of free zirconia collected from 15 g of NCP MRF powder was not measured prior to XRD measurements; qualitatively, the resulting mass of free zirconia was a small percentage of the powder. A second separation procedure was executed using 100 g of NCP MRF powder in an attempt to quantitatively define the concentration of free zirconia in the bulk powder (Subsection 5.2.1). The results of this experiment indicate that $\approx 0.28\%$ of the NCP powder is composed of free zirconia particles.

There are several areas of the Zr P1 procedure that could be improved if this technique is to be used in the future. The MRF powder should be placed in an oven to remove any excess moisture before and after the magnetic separation. The mass of the dried powder should be determined before and after the experiment, and compared with the mass of nonmagnetic particles collected during the procedure. A larger number of 100 mL beakers should be used instead of 250 mL beakers to contain the excess colloidal dispersion so that a more precise mass can be obtained by using the analytical balance. The precision of this result could be improved by increasing both the number of samples, and the mass of powder samples tested. The resultant mass-fraction of free zirconia was

low enough to indicate that additional abrasives were necessary, and further testing was not required for the scope of this work.

The Acoustosizer IIs was used to measure particle size distribution of samples from eight NCP powder batches. The measured particle diameters presented in Section 6.8 show good precision for the D15 (0.293 ± 0.088 µm) and D50 (2.462 ± 0.346 µm) particle size categories. The measured diameters in the D80 category show a larger standard deviation (22.659 ± 4.867 µm); this result suggests the presence of agglomerations in the the samples. The precision of the D80 category is somewhat questionable, as settled particle agglomerates were observed at the base of the mixing vessel, which suggests the measured D80 is less than the actual value. Despite the use of the surfactant Darvan *C, maintaining a dispersed slurry was difficult. The stir-rod RPM was limited to ≈ 350; if the stirring rate was increased too much, bubbles were introduced into the slurry, which interfered with the ESA measurements and reduced the accuracy of the results. Notwithstanding these problems, the Acoustosizer IIs was adequate for determining the particle size distribution of MR powders.

7.7 Combined Technique Mass-Fraction Analysis

Results of density measurements were used to check the accuracy of several analytical techniques, including: XRF, ΔMC, XRD, and EDS (Section 6.5, pg. 121). A theoretical density was calculated from the measured sample volume, the mass-fraction results obtained from an analytical technique, and densities of the three MR powder components

(Fe, Fe(ii,iii), and ZrO_2). The density of zirconia was obtained from Holleck [62]. X-ray diffraction revealed that the iron oxide species was magnetite (a density of 5.1 g/cm^3 was obtained from US Research Nanomaterials) [63]. The density of iron was obtained from in-house pycnometry measurements of CI-HQ. The theoretical density was compared to the measured density to determine the accuracy of the analytical technique. The mass-fraction results obtained using XRD and EDS were shown to be inaccurate, while calculations using XRF and ΔMC results were close to the measured values. One surprising result in Table 6.8 was the increased mass-fraction of iron oxide in the NCP powder compared to the OCP powder. It is conceivable that either the sol-gel synthesized using the new procedure, or the increased sol-gel concentration were responsible for the increase in rate of the CI powder oxidation during the coating process.

There was a very high variance in results obtained from XRF, XRD, and EDS. Since the XRF instrument was not able to detect oxygen, it was assumed that the zirconium signal corresponded to ZrO_2. With the concentration of zirconia defined, the remaining mass-fraction was due to iron and iron oxide. The ratio between Fe and Fe(ii,iii) was adjusted to observe the effect on calculated density and volume (Table 6.8). Results from EDS contained an oxygen signature, with a portion ascribed to the zirconium signal and the remainder attributed to iron oxide. X-ray diffraction of unaltered samples provided a ratio of iron to iron oxide, while scans of heat-treated powders yielded a ratio of iron oxide to zirconia. The iron to iron oxide ratio from the unaltered samples were normalized to include the concentration of zirconia. The resultant normalized mass-fraction

distribution was used to calculate the density. Theoretical sample volume was calculated from the product of the powder's mass, the inverse of the density of the species, and semi-quantitative mass-fraction distribution. A porosity term was introduced to account for the error in calculated volume; negative porosity indicates that the calculated volume was larger than the measured volume of the sample. For the ΔMC, zirconia concentration calculated from the difference between the initial 200 g mass of CI, and the ≈230 g mass of the coated MR powder. The ratio between iron and iron oxide was adjusted to produce a calculated density that matched the measured value. Three different elemental ratios were calculated using ΔMC, with increasing concentrations of zirconia, based on assumed loss of iron during the coating process (Section 6.3).

The density and volume data used for the OCP MR powder calculation was taken from one pycnometry measurement as opposed to an average of multiple values; the same is true for the NCP MR powder calculation. It was thought that only using one data point would reduce error in the calculation. The overestimation of sample volume seen in Table 6.8 was likely caused by inaccuracies in the assumed densities of Fe(ii,iii) and ZrO_2. It is possible to measure these densities in-house; magnetite powder could be procured from an online vendor, and the zirconia sol-gel could be calcinated at ≈ 500°C to produce a zirconia powder. These powders would be measured using the Accupyc II 1350 to determine whether the assumed density values were accurate. If the measured density of the magnetite and zirconia powder closely matched values assumed for the calculation, it would indicate that something else is causing the inaccuracy. It is plausible that the XRD results were inaccurate in the indication that magnetite was the only species of

iron oxide present in the MR powders. The presence of multiple iron oxide phases would render this method useless. With three components, any zirconium signal can be attributed to zirconia and the ratio between iron and magnetite can be adjusted to match the measured density. If there were four powder components, there would not be enough information to determine the appropriate ratios.

7.8 Summary

- Iterative improvements to the accelerated corrosion test resulted in placing slurries in a stir-bar agitated, pH 2.0 environment that simulated the the conditions seen by the MR slurries in the STM.
- A 4F-16TC-FF accelerated corrosion experiment was implemented to determine which factors in the manufacturing procedure should be altered to increase the corrosion resistance of the MR powder in acidic environments:
  - The 16TC-FF design was chosen over an 8TC-FF, or resolution IV design for the increased information on factors and factor interactions, despite the requirement of running twice as many tests.
  - No concrete explanation was found for the large variance in corrosion times seen in individual batches, although this was expected to be caused by variations in coating thickness between MR particles.
  - The 15 min. interval between photographs used to quantify the time of slurry corrosion only introduced a maximum error of 5% to the measured corrosion

time, which was not deemed to be significant as NCP MR powders remained stable for ∼1074 min.

  - Further research is required to determine if the synthesis of zirconia sol-gel used for the coating of the CIP is optimal; it is possible that decreasing the rate of zirconia hydrolysis would increase the homogeneity of coating thickness on the CIP.

- There were three goals for powder analysis: (1) develop a procedure to quantify powder composition; (2) determine the thickness of the amorphous zirconia coating; and (3) determine the mass-fraction of free zirconia in the NCP MR powder:
  - Goal (1) was successfully accomplished by combining the results of helium-gas pycnometry, ΔMC, and XRF measurements. This method could be improved by quantifying the concentration of iron oxides in the CIP that develop during the sol-gel coating process, and using a vacuum environment when measuring MR powders with XRF to enable the detection of oxygen.
  - Goal (2) was achieved by embedding MR powder in epoxy, polishing the surface to expose cross-sections of the MR powder, and imaging the particles using SEM InLens and BSD detectors. This approach could be improved through the development of a method to measure a statistically significant number of particles, as the current labor intensive method required taking dozens of line-outs to determine the average coating thickness of one MR particle.

  - (3) was successfully accomplished by using the magnetic isolation process (ZrP1) to measure a free zirconia concentration of 0.28%. This technique could be improved by using a larger mass of coated MR particles in ZrP1, or increasing the number of samples exposed to ZrP1.

- A range of success was found when MR powders were measured with different analytical X-ray techniques:

  - Measurement of MR powders with XRD was marginally successful, the amorphous nature of the zirconia coating was confirmed and the presence of iron oxides in the CIP was confirmed, however, the semiquantitative mass-fraction results were inaccurate when checked against ΔMC calculations.
  - Energy dispersive spectroscopy did not yield any useful results; semiquantitative mass-fraction data was not accurate, and sample preparation was a labor intensive process.
  - Application of XPS to quantify the coating thickness of MR particles was unsuccessful, however; scans indicated the presence of coating thickness < 20 nm in both OCP and NCP MR powders.
  - It may be possible to use XPS measure the zirconia coating thickness that the OCP and NCP produce if macroscopic iron samples were coated.
  - Measurement of MR powders with XRF was highly successful; measurement times were short, sample preparation was not required, and semiquantitative mass-fraction analysis closely agreed with ΔMC and pycnometry measurements.

  - Further improvements to the accuracy of XRF results could be obtained by measuring samples in vacuum, which would allow for the oxygen signature from zirconia and iron oxides to be registered.

- Helium gas pycnometry was successfully used to measure the density of CIP, OCP and NCP MR powders.

- The greater range in density measurements of OCP and NCP MR powders compared to CIP measurements, indicates that there is either inhomogeneity in density between samples or variations in the average batch density.

- The Acoustosizer IIs was used to measure particle size distribution of samples from eight NCP powder batches.

- The measurement of larger D80 particles (∼10x greater than the manufacture's specifications) indicates that agglomerations are formed during the MR powder drying procedure.

Chapter 8

Conclusions and Future Work

8.1 Summary

Pebble like surface decorations are induced when CVD ZnS optics are polished with conventional MRF slurries, which increases the PV and RMS roughness [38]. To address this issue, chemically modified MRF slurries were developed, which combined the effects of chemical etching and mechanical removal [6]. While these modified slurries reduced the PV and RMS roughness of the CVD ZnS parts, the slurries showed limited stability due to the corrosion of the uncoated CI powder in the acidic regime. Using a zirconia sol-gel to coat the CI powder, a MRF slurry was produced that showed improved corrosion resistance. Despite the increase in corrosion resistance that the zirconia-coated MR powders provided, the MRF slurries still destabilized after approximately nine days, which was deemed insufficient for practical application [6]. A primary objective of this

work was to further increase the corrosion resistance of the zirconia-coated CI powder and improve the longevity of the MRF slurry. A stir-bar agitated corrosion test was developed to measure the durability of the OCP MR powder in a pH 2 slurry. The OCP MR powder corroded in 5.5 ± 1.6 hrs.

A 16TC-FF experiment was designed to ascertain which steps in the MR powder manufacturing process should be altered to improve corrosion resistance of the zirconia-coated CI powder. Of the four factors that were tested, three were shown to have a measurable impact on the longevity of powders in acidic environments: (1) altering the synthesis of the zirconia sol-gel; (2) increasing the concentration of zirconia sol-gel during coating of the CI powder; and (3) drying the powder at a temperature of 60°C under moderate vacuum. The fourth factor, pre-milling the CI powder before coating, was not found to be significant according to the ANOM and ANOVA, but was still included in the NCP as a measure to prevent coating particle agglomerations. This new powder corroded after 17.9 ± 2.2 hrs, an $\approx 3.25\times$ improvement over the OCP MR powder.

With a new coating procedure defined, efforts were made to develop a generalizable procedure to characterize the new and old MR powders. The two primary goals were to measure the mass fraction of components in the powders, and determine the mass fraction of free zirconia in the bulk powder. Quantifying powder components was prioritized to determine the extent that the NCP changed MR powder composition, and to have a method of analysis prepared in case of further alterations in the manufacturing process. Free zirconia concentration was investigated to quantify its contribution to the total amount of free-abrasives; MRF slurry composition is very precise and small

changes can significantly alter important physical parameters such as viscosity, which can significantly reduce the surface characteristics of the finished CVD ZnS part.

A survey of four analytical X-Ray techniques and three physical property measurement techniques were used to characterize the MR powders. Of the analysis methods used: XRF, helium-gas pycnometry, ΔMC, ZrP1, and SEM micrographs of MR powder cross sections were the most successful in quantifying powder composition. Results from XRF, pycnometry, and ΔMC indicate that the composition of OCP MR powder is: 58% Fe, 27% Fe(ii,iii), and 15% ZrO_2. Similar measurements of NCP MR powder suggest a composition of: $31.0 - 38.9\%$ Fe, $39.0 - 39.5\%$ Fe(ii,iii), and $21.6 - 30.0\%$ ZrO_2. By increasing the concentration of zirconia sol-gel by 20% during the coating process, a $\approx 150 - 200\%$ increase in zirconia concentration was achieved. The SEM micrographs of NCP MR powder cross sections showed a $58.5 - 198$ nm range in coating thickness between particles; additionally, up to a 75 nm range in coating thickness was measured in one coated particle. Due to factors such as variance of coating thickness, thin coatings, sample geometry, particle size distribution, and double oxide layer, analytical X-ray techniques were unsuccessful in corroborating these results. A mass fraction of 0.283% free zirconia was measured in the NCP MR powder using the magnetic separation process ZrP1; XRD and XRF analysis confirmed that the powder sample was $85 - 99\%$ ZrO_2.

8.2 Conclusions

Modification of zirconia coated carbonyl iron particles for magnetorheological finishing was shown to suppress corrosion in acidic environment. Design of experiments was used to develop a 16 TC-FF experiment that improved MR particle survivability through alterations in the powder manufacturing procedure. Process variables were evaluated using an accelerated corrosion test that simulated the MR slurry environment, with a quantifiable time of corrosion. The optimal coating was obtained by adding zirconium butoxide prior to nitric acid, increasing sol-gel concentration to 60 vol%, and using a 60° C drying temperature . A combination of physical analysis and analytical X-ray techniques were used to measure a ∼175% increase in zirconia concentration in the NCP MR powder. The NCP improves the zirconia coated MR powder's survivability in pH 2.5 MR slurries by ∼3.25x; its time to corrosion was increased from ∼300 min to ∼1074 min.

8.3 Recommendations for Future Work

The following suggests areas of further improvement to the performance and characterization of zirconia-coated MR powder that build on the work conducted in this thesis.

8.3.1 Continued Optimization of the Coating Process

While the NCP increased the corrosion resistance of the MR powder by more than a factor of three, it is not clear that these improvements were optimal. Further improvements could be made to the zirconia sol-gel synthesis procedure by changing concentration of species present in the coating process. The increase of zirconia sol-gel concentration from 40 vol% to 60 vol% was selected in an attempt to produce a significant increase to sol-gel concentration while at the same time maintaining sufficient magnetic potential. If a third concentration of zirconia sol-gel was used to produce a MR powder batch, a calibration curve could be produced to define the relationship between sol-gel concentration and particle coating thickness. With this calibration, the concentration of sol-gel used in the coating process could be optimized to further increase the corrosion resistance of the coated powder while maintaining a specified magnetic potential. It may be prudent to focus future research towards the sol-gel synthesis process, as the sol-gel process used in the OCP and NCP MR powder was implemented in 2009, and may benefit from further refinement. Work done by Miao et al. showed the potential of dual-coated MR powder for MRF slurries [79]. The dual-coated powder exhibited no signs of corrosion after 12 days in a pH 4.4 environment. There was significant difficulty in achieving a low viscosity in slurries using the hydrophilic dual-coated MR powder; however, slurries created with OCP and NCP MR powders exhibit transience in slurry pH [6]. Working with the pH-stable, dual-coated particles may prove to be a better solution for creating a stable pH 4 MRF slurry than using corrosion resistant NCP MR powder.

8.3.2 Continued Improvements to MR Powder Characterization

While XRF was successfully used to obtain semi-quantitative mass fraction distribution of MR powder components, the precision of results could be significantly improved by performing the measurements in vacuum. Elements with a mass smaller than sodium can not be detected in an ambient atmospheric environment. If there is a significant presence of an undetected element, the concentration of recorded elements will be artificially increased [60]. Measurements of MR powders in vacuum would provide the mass fraction of oxygen in addition to the iron and zironium; this would improve the precision of XRF measurements [77].

Continued efforts should be made to develop a method of quantifying the average coating thickenss of zirconia-coated MR powders using XRF. A calibration can be made by scanning monolayers of approximately six powder samples, ranging in composition from 100% ZrO_2 to 100% Fe. Several new batches of zirconia-coated MR powders would need to be created using an increased concentration of zirconia sol-gel during the coating procedure. Once the data has been processed, the results can be analyzed and an average thickness calculation can be performed by using Equation 8.1 [80] to compare the ratios of Fe K_α to Fe K_β:

$$t_{ZrO_2} = \frac{-ln(\frac{I}{I_0})}{(\mu/\rho_{ZrO_2})\rho_{ZrO_2}} \tag{8.1}$$

where: t_{ZrO_2} is the thickness of the zirconia coating, 'I' is the intensity of Fe K_α, 'I_0'

is the intensity of Fe K_β, μ/ρ is the mass attenuation coefficient, and ρ is the density of zirconia that the Fe X-rays are passing through. An alternative to performing these measurements on coated CI powder would be to produce macroscopic iron samples, avoiding the inherent difficulties of measuring the coating thickness of small, thinly coated, spherical particles.

Appendix A

Flow Diagrams for the OCP and NCP

Original Coating Process

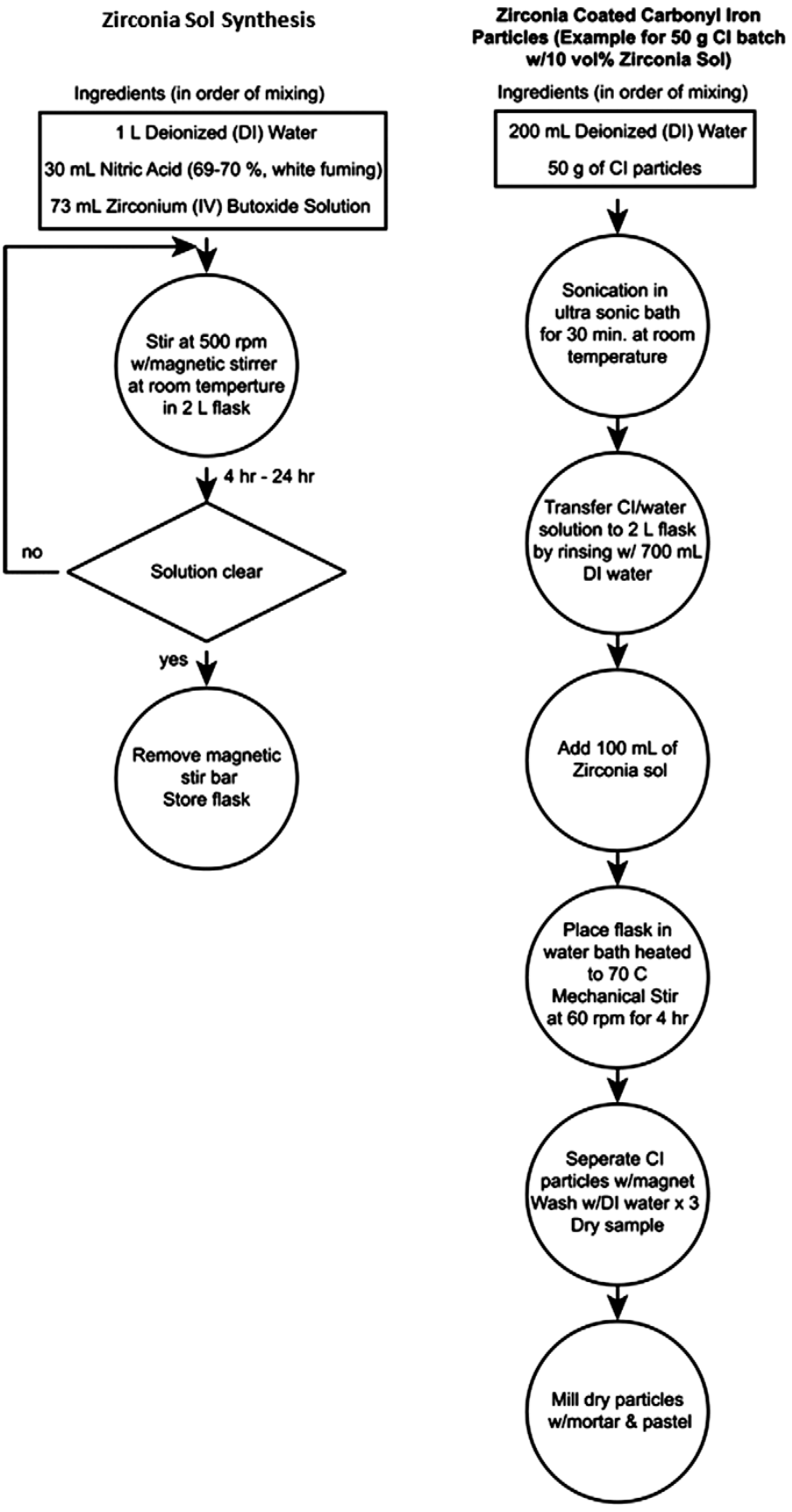

New Coating Process - Modified version 2013

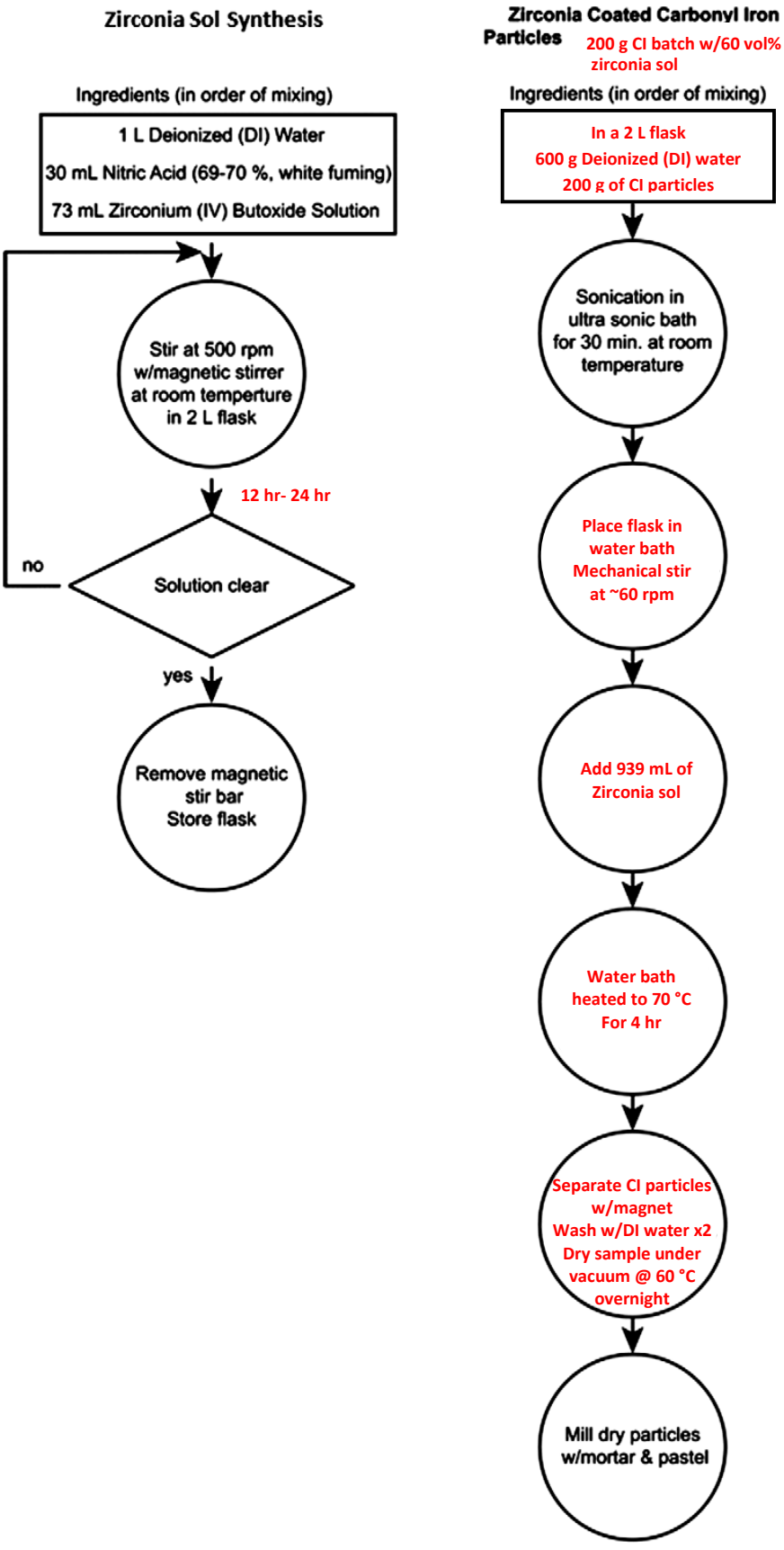

Appendix B

16TC FF Corrosion Testing

Procedure

1. Corrosion testing samples were prepared with 10 vol% of coated particles dispersed in a 50% acetic acid DI water solution:

$$m_{_{MRpowder}} = 6g \tag{B.1a}$$

$$\rho_{_{MRpowder}} = 6.72\frac{g}{cm^3} \tag{B.1b}$$

$$V_{_{MRpowder}} = \frac{6g}{6.72\frac{g}{cm^3}} = 0.8928cm^3 \tag{B.1c}$$

$$V_{_{Total}} = \frac{0.893cm^3}{0.1} = 8.928cm^3 \tag{B.1d}$$

$$V_{_{Acid\ \ Solution}} = 8.928cm^3 - 0.8928cm^3 = 8.03cm^3 \tag{B.1e}$$

$$V_{_{Acid\ \ Component}} = \frac{8.03cm^3}{2} = 4.015cm^3 \tag{B.1f}$$

$$\rho_{_{DI\ \ Water}} = 1.00\frac{g}{cm^3} \tag{B.1g}$$

$$\rho_{_{Acetic\ \ Acid}} = 1.05\frac{g}{cm^3} \tag{B.1h}$$

$$m_{_{DI\ \ Water}} = 1.00\frac{g}{cm^3} \times 4.015cm^3 = 4.015g \tag{B.1i}$$

$$m_{Acetic\ \ Acid} = 1.05\frac{g}{cm^3} \times 4.015cm^3 = 4.216g \tag{B.1j}$$

$$m_{Acid\ \ Solution} = (m_{DI\ \ Water} + m_{Acetic\ \ Acid})n = (4.051g + 4.216g)n \tag{B.1k}$$

   (a) Where 'n' is the number of samples to be tested.

2. A solution of 50 vol% glacial acetic acid solution in DI water was prepared.
3. Ten 200 mL beakers were set on the lab bench.
4. 8.26 g of the acid solution was pipetted into each beaker, using one of the scales located directly to the right of the fume hood.
5. A stir-bar was added to each beaker (that each was the same size and model). For this experiment "Spinbar Polygon with ring: 25 × 6mm" stir-bars were used, model, Catalog #: 371220025.
6. Zirconia-coated powder containers were vigorously shaken for 3 minutes, and let settle for another minute. This created an even distribution of the particle size for sampling.
7. Using a scoopula, $6.0g$ of MR powder were placed into a small disposable sample dish.
8. With a Sharpie, each 200 mL beaker was labeled with the batch number for later identification.
9. A cover was placed on the top of the stir-plate surface, either paper towels or thin foam, as samples had a tendency to overflow the beaker when they corrode.
10. The beakers with the stir-bars and acid were placed onto the stir-plate, their location on the 9-location stir-plate was recorded. The date and time of the test was also recorded in a lab notebook.
11. The 9-location stir-plate was turned on.
12. A timer was started.
13. One charge of coated powder was added to each beaker.
14. After 20 minutes, allowing for stabilization of RPM, an RPM check of the stir-bars was performed.
    (a) If using a stir-plates with RPM indicators, steps b-d were ignored and the RPM was set to 350.
    (b) The Strobotak was plugged into one of the fume hood outlets.
    (c) The Strobotak was set to 700 Hz and turn on.

(d) The Strobotak was held above the beakers, speed dials were adjusted so the stir-bars were rotating at 350 RPM (1/2 of the Strobotak's value). It was easy to tell if the stir-bar was at the desired rotational velocity for two reasons: if it was rotating at 700 RPM there was be significant splashing, if it was at the desired value, the stir-bar appeared to be motionless.

15. The beakers were monitored throughout the day, Figure C.1 displayed the changes that occur during the corrosion test during the day, recording the corrosion time of any beaker in the lab notebook if any samples corrode.

    (a) If a sample did corrode during the day, it may be removed from the stir-plate and washed; this made the cleanup and setup for the next experiment easier. See Appendix C for complete cleaning instructions.

16. Near the end of the day, a camera was set up the with the AC power adapter over the stir-plate in the fume hood.

    (a) The "BatteryMiser2.lua" program was used, this is located on the black memory card

    (b) The program was set to take a picture once every 600 seconds.

        i. See Jackson's Memo "Taking Interval Photos Using the Canon SD1300 IS" (6/28/2013) for more detailed information about the program.

17. Most samples were corroded by early the next morning, if not, wait until all samples are corroded to proceed.

18. The camera was removed and pictures were imported onto the computer.

19. The pictures were loaded, and the corrosion times of all samples were recorded in the lab notebook and or an excel spreadsheet.

    (a) Corrosion time was defined as the first picture where foaming was seen in the beaker.

    (b) Occasionally, samples didn't foam and instead thickened and hardened. Corrosion for these samples was defined as the first image where obvious reduction in speed of the stir-bar was seen.

Appendix C

MRF Corrosion Test Cleaning Procedure

If the corroded iron powder was allowed to dry, it proved quite difficult to properly clean the 200 mL beaker for another use. This happened quite frequently, as batches would often corrode soon after the work day and dry out over night. This lead to the necessity of developing a cleaning procedure, outlined below.

Cleaning: It is recommended to clean a beaker containing a sample as soon as it corrodes. Beakers are much easier to clean if the corroded iron particles aren't allowed to harden.

1. When a sample corrodes, use a scoopula to remove the stir-bar
    (a) Place the stir-bar onto a paper towel

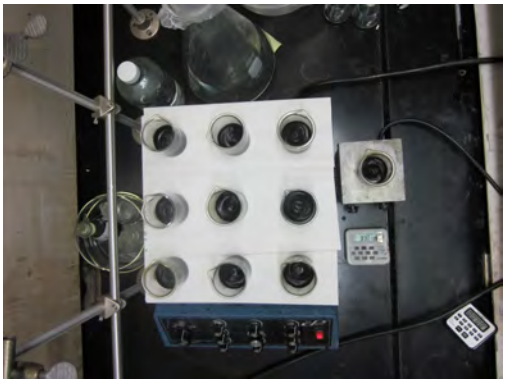

(a) Corrosion test of powder samples HJR 8B and 13B, 3:30 hours into the test with no samples displaying signs of corrosion.

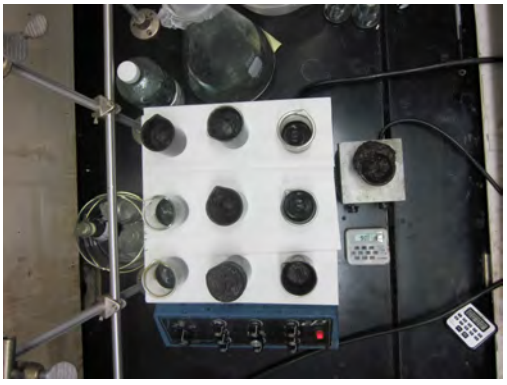

(b) Corrosion test of powder samples HJR 8B and 13B, 9:00 hours into the test. Six of the ten samples have corroded, as evidenced by the foam emitting from the beakers.

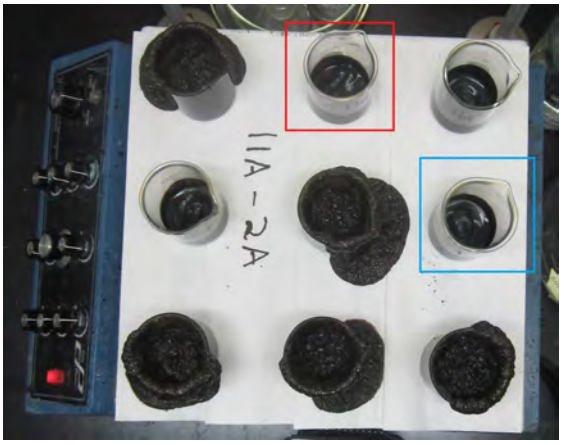

(c) The corrosion test of powder samples 2A and 11A, 15:22 hours into the test. The sample outlined with the red square exhibits the uncommon response of corrosion without foaming, evidenced by the stationary stir-bar. The sample outlined with the blue square displays an non-corroded sample with the stir-bar still rotating.

Figure C.1: Various stages in the corrosion test process showing various corroded and non-corroded samples. The experimental settings used to make the table are shown in Table 3.3.

2. Using the scoopula, remove as much material as possible and deposite it into a plastic container for later disposal. This is preferred to washing everything down the drain, as it causes unnecessary strain on the drainage system

3. Using warm water, rinse out the beaker and stir-bar

4. Do NOT use Scotch-Brite pads OR Gojo, as they will scratch the glass, making the beaker more difficult to clean in the future

5. Apply "Soft-Scrub" to a sponge and continue cleaning the beaker, make sure there are no iron particles remaining in the beaker, it should look clear with no spots on the bottom when finished

6. Scotch-Brite pads are useful for cleaning the stir-bars

7. If the corroded material has hardened to the point that the technique described in '5' isn't working, or if the beaker has a distinct yellow-orange hue, it may be necessary to clean the beaker with SC2. MAKE sure to wear the PROPPER PPE (Lab coat, chemical safety goggles, and extended cuff gloves) and have a buddy

   (a) This cleaning technique uses pH $<<$ 1 acid and should be kept to a minimum, it is recommended to wait until there are over six beakers that require additional cleaning to take this step

   (b) After cleaning beakers and stir-bars as well as possible using step 5, bring them next door to Room: 1430

   (c) Place the beakers and stir bars into a crystalizing dish, fill each beaker 1/3 to 1/2 way up with tap water

   (d) Move the crystalizing dish with beakers into the middle fume hood

   (e) ENSURE that both you and your buddy have the proper PPE

(f) The used SC2 can be found under the middle fume hood, take out a bottle and fill the beakers the rest of the way up with the SC2

(g) Let sit for several hours, ideally overnight

(h) Carefully move the crystallization dish to a sink and overflow rinse

i. Turn on a second sink to increase the water flow in the pipes, further diluting the acid

ii. Every two minutes or so, move the water steam out of the crystallization dish and direct it down the sink, this is another important step in diluting the acid to appropriate levels

iii. Use pH strips to determine when the solution has been neutralized to: 6 $<$ pH $<$ 8

8. Remove beakers and stir-bars from crystallization dish

9. Rinse everything, including crystallization dish, with DI water and air dry

†I'm guessing I should just remove the cleaning portion, as it's pretty insignificant†

Bibliography

[1] M Shane and ML Mecartney. Sol-gel synthesis of zirconia barrier coatings. *Journal of Materials Science*, 25(3):1537–1544, 1990.

[2] Stephen D. Jacobs. Manipulating mechanics and chemistry in precision optics finishing. *Science and Technology of Advanced Materials*, 8(3):153 – 157, 2007. ISSN 1468-6996. doi: http://dx.doi.org/10.1016/j.stam.2006.12.002. URL http://www.sciencedirect.com/science/article/pii/S1468699607000022.

[3] Irina A. Kozhinova, Henry J. Romanofsky, Alexander Maltsev, Stephen D. Jacobs, William I. Kordonski, and Sergei R. Gorodkin. Minimizing artifact formation in magnetorheological finishing of chemical vapor deposition zns flats. *Appl. Opt.*, 44 (22):4671–4677, Aug 2005. doi: 10.1364/AO.44.004671. URL http://ao.osa.org/abstract.cfm?URI=ao-44-22-4671.

[4] Rui Shen, Shai N. Shafrir, Chunlin Miao, Mimi Wang, John C. Lambropoulos, Stephen D. Jacobs, and Hong Yang. Synthesis and corrosion study of zirconia-coated carbonyl iron particles. *Journal of Colloid and Interface Science*, 342(1):49

– 56, 2010. ISSN 0021-9797. doi: http://dx.doi.org/10.1016/j.jcis.2009.09.033. URL http://www.sciencedirect.com/science/article/pii/S0021979709012168.

[5] Shai N. Shafrir, Henry J. Romanofsky, Michael Skarlinski, Mimi Wang, Chunlin Miao, Sivan Salzman, Taylor Chartier, Joni Mici, John C. Lambropoulos, Rui Shen, Hong Yang, and Stephen D. Jacobs. Zirconia-coated carbonyl-iron-particle-based magnetorheological fluid for polishing optical glasses and ceramics. *Appl. Opt.*, 48 (35):6797–6810, Dec 2009. doi: 10.1364/AO.48.006797. URL http://ao.osa.org/abstract.cfm?URI=ao-48-35-6797.

[6] S. Salzman, H. J. Romanofsky, Y. I. Clara, L. J. Giannechini, G. West, J. C. Lambropoulos, and S. D. Jacobs. Magnetorheological finishing with chemically modified fluids for studying material removal of single-crystal zns. *Proc. SPIE*, 8884:1–15, 2013. doi: 10.1117/12.2028941. URL http://dx.doi.org/10.1117/12.2028941.

[7] Samuel R Steele and James Pappis. Chemical vapor deposition of IR materials. Technical report, DTIC Document, 1971.

[8] John McCloy and Randall Tustison. *Chemical Vapor Deposited Zinc Sulfide*. SPIE Press, 2013.

[9] Fang Zhenyi, Chai Yichao, Hao Yongliang, Yang Yaoyuan, Dong Yanping, Yan Zewu, Tian Hongchang, Xiao Hongtao, and Wang Heming. CVD growth of bulk polycrystalline ZnS and its optical properties. *Journal of Crystal Growth*, 237-239, 2002. ISSN 0022-0248. doi: 10.1016/S0022-0248(01)02338-7.

[10] Claude A Klein, Theodore Kohane, et al. Chemically vapor-deposited zinc sulfide infrared windows: Optical properties and physical characteristics. In *23rd Annual Technical Symposium*, pages 85–94. International Society for Optics and Photonics, 1980.

[11] John McCloy. International development of chemical vapor deposited zinc sulfide. page 654503–654503–12, 2007. doi: 10.1117/12.717870.

[12] P Biswas, R Kumar, P Ramavath, V Mahendar, G Rao, U Hareesh, and R Johnson. Effect of post-cvd thermal treatments on crystallographic orientation, microstructure, mechanical and optical properties of zns ceramics. *Journal of Alloys and Compounds*, 496(1-2):273277, 2010. ISSN 0925-8388. doi: 10.1016/j.jallcom.2010.01.120.

[13] John McCloy, Ralph Korenstein, Brian Zelinski, et al. Effects of temperature, pressure, and metal promoter on the recrystallized structure and optical transmission of chemical vapor deposited zinc sulfide. *Journal of the American Ceramic Society*, 92(8):1725–1731, 2009.

[14] D. C. Harris. *Materials for Infrared Windows and Domes*. SPIE Press, Bellingham WA, 1999.

[15] R. N. Donadio, J. F. Connolly, and R. L. Taylor. New advances in chemical vapor deposited (CVD) infrared transmitting materials. In *25th Annual Technical Symposium*, pages 65–69. International Society for Optics and Photonics, 1982.

[16] John McCloy, Brian Riley, and David Pierce. Infrared-transparent glass ceramics: An exploratory study. *Journal of Non-Crystalline Solids*, 410:160173, 2015. ISSN 0022-3093. doi: 10.1016/j.jnoncrysol.2014.11.040.

[17] Daniel C. Harris. Durable 3–5μm transmitting infrared window materials. *Infrared Physics & Technology*, 39(4):185 – 201, 1998. ISSN 1350-4495. doi: http://dx.doi.org/10.1016/S1350-4495(98)00006-1. URL http://www.sciencedirect.com/science/article/pii/S1350449598000061.

[18] John S McCloy, Brian J Riley, David A Pierce, Bradley R Johnson, and Amy Qiao. Infrared-transmitting glass-ceramics: a review. In *SPIE Defense, Security, and Sensing*, pages 87080N–87080N. International Society for Optics and Photonics, 2013.

[19] Daniel C Harris. History of magnetorheological finishing. In *SPIE Defense, Security, and Sensing*, pages 1–22. International Society for Optics and Photonics, 2011.

[20] Stephen D. Jacobs, Donald Golini, Yuling Hsu, Birgit E. Puchebner, D. Strafford, Igor V. Prokhorov, Edward M. Fess, D. Pietrowski, and William I. Kordonski, editors. *Magnetorheological finishing: a deterministic process for optics manufacturing*, volume 63, Apr. 1995. LLE Review.

[21] Ajay Sidpara. Magnetorheological finishing: a perfect solution to nanofinishing requirements. *Optical Engineering*, 53(9):1–7, 2014. doi: 10.1117/1.OE.53.9.092002. URL http://dx.doi.org/10.1117/1.OE.53.9.092002.

[22] Donald Golini. Precision optics manufacturing using magnetorheological finishing (MRF). volume 3739, pages 78–85. Proc. SPIE, 1999. doi: 10.1117/12.360131. URL http://dx.doi.org/10.1117/12.360131.

[23] QED Technologies. Q-flex 300, next generation MRF polishing machine, product specifications. https://www.qedmrf.com/polishing/products/q-flex-300, 2014.

[24] Jean Pierre Lormeau, Chris Supranowitz, Paul Dumas, Tobias Nitzsche, and Rich Jenkins. Field proven technologies for fabrication of high-precision aspheric and freeform optical surfaces. In *Optics and Measurement Conference 2014*, pages 944203–944203. International Society for Optics and Photonics, 2015.

[25] QED Technologies. Q-flex 300 polishing results. https://www.qedmrf.com/polishing/products/q-flex-300, 2014.

[26] Chris Supranowitz, Paul Dumas, Tobias Nitzsche, Jessica Nelson, Brandon Light, Kate Medicus, and Nathan Smith. Fabrication and metrology of high-precision freeform surfaces. In *Society of Photo-Optical Instrumentation Engineers (SPIE) Conference Series*, volume 8884, page 888411–888411–10, Sept. 2013. doi: 10.1117/12.2030144.

[27] Harvey M. Pollicove, Edward M. Fess, and John M. Schoen. Deterministic manufacturing processes for precision optical surfaces. *Proc. SPIE*, 5078:90–96, 2003. doi: 10.1117/12.487105. URL http://dx.doi.org/10.1117/12.487105.

[28] Kate Medicus, Jessica D. Nelson, Timothy Lynch, Matt Brunelle, and Matthew Brophy. Freeform optical manufacturing and testing processes for ir conformal window and domes. *Proc. SPIE*, 9453:94530E–94530E–10, 2015. doi: 10.1117/12.2177279. URL http://dx.doi.org/10.1117/12.2177279.

[29] Jannick Rolland and Kevin Thompson. Freeform optics: Evolution? No, Revolution! *SPIE Newsroom*, 2012. doi: 10.1117/2.1201207.004309.

[30] Harvey M Pollicove. Next-generation optics manufacturing technologies. In *International Topical Symposium on Advanced Optical Manufacturing and Testing Technology*, pages 8–15. International Society for Optics and Photonics, 2000.

[31] Jasbinder Sanghera, Woohong R Kim, and Shyam Bayya. Conference 9453: Window and dome technologies and materials XIV. *SPIE DSS*, 9453:36–41, April 2015.

[32] Charles Klinger. Vibe: A new process for high speed polishing of optical elements. *Optifab: Technical Digest, SPIE Technical Digest TD04*, 2007.

[33] Paul E. Murphy, James T. Mooney, and Thomas P. Courtney. Fabrication of EUV components with MRF. *Proc. SPIE*, 5193:29–38, 2004. doi: 10.1117/12.506274. URL http://dx.doi.org/10.1117/12.506274.

[34] Irina A. Kozhinova, Henry J. Romanofsky, Stephen D. Jacobs, William I. Kordonski, and Sergei R. Gorodkin. Polishing of pre-polished cvd zns flats with altered magnetorheological (MR) fluids. In *Frontiers in Optics 2004/Laser Science XXII/Diffractive Optics and Micro-Optics/Optical Fabrication and Testing*, page

OMD2. Optical Society of America, 2004. doi: 10.1364/OFT.2004.OMD2. URL http://www.osapublishing.org/abstract.cfm?URI=OFT-2004-OMD2.

[35] Stephen D. Jacobs, Fuqian Yang, Edward M. Fess, J. B. Feingold, Birgit E. Gillman, William I. Kordonski, Harold Edwards, and Donald Golini. Magnetorheological finishing of ir materials. *Proc. SPIE*, 3134:258–269, 1997. doi: 10.1117/12.295132. URL http://dx.doi.org/10.1117/12.295132.

[36] Paul Dumas, Don Golini, and Marc Tricard. Improvement of figure and finish of diamond turned surfaces with magneto-rheological finishing (MRF). *Proc. SPIE*, 5786:296–304, 2005. doi: 10.1117/12.603967. URL http://dx.doi.org/10.1117/12.603967.

[37] Christopher Supranowitz, Christopher Hall, Paul Dumas, and Bob Hallock. Improving surface figure and microroughness of ir materials and diamond turned surfaces with magnetorheological finishing (MRF). *Proc. SPIE*, 6545:1–11, 2007. doi: 10.1117/12.719792. URL http://dx.doi.org/10.1117/12.719792.

[38] Stephen D. Jacobs. MRF with adjustable pH. *Proc. SPIE*, 8169:1–9, 2011. doi: 10.1117/12.902235. URL http://dx.doi.org/10.1117/12.902235.

[39] John McCloy, Eric Fest, Ralph Korenstein, and W. Howard Poisl. Anisotropy in structural and optical properties of chemical vapor deposited ZnS. *Proc. SPIE*, 8016:1–11, 2011. doi: 10.1117/12.886138. URL http://dx.doi.org/10.1117/12.886138.

[40] K. L. Lewis, A. M. Pitt, J. A. Savage, J. E. Field, and D Townsend. Mechanical properties of CVD-grow zinc-sulfide and their dependence on the conditions of growth. In *Journal of the Electrochemical Society*, volume 131. Electrochemical soc. inc. 10 south main street, Pennington, NJ 08534, 1984.

[41] Y Drezner, S Berger, and M Hefetz. A correlation between microstructure, composition and optical transparency of CVD-ZnS. *Materials Science and Engineering: B*, 87(1):59 – 65, 2001. ISSN 0921-5107. doi: http://dx.doi.org/10.1016/S0921-5107(01)00701-2. URL http://www.sciencedirect.com/science/article/pii/S0921510701007012.

[42] Dong-Woo Kim, Myeong-Woo Cho, Tae-Il Seo, and Young-Jae Shin. Experimental study on the effects of alumina abrasive particle behavior in mr polishing for mems applications. *Sensors*, 8(1), 2008. doi: 10.3390/s8010222.

[43] Michael D. Skarlinski and Stephen D. Jacobs. Modifying the rheological properties of zirconia coated carbonyl iron suspensions through acid-base titration and the addition of di-ammonium citrate. In *International Optical Design Conference and Optical Fabrication and Testing*, page JMB2. Optical Society of America, 2010. doi: 10.1364/OFT.2010.JMB2. URL http://www.osapublishing.org/abstract.cfm?URI=OFT-2010-JMB2.

[44] J. P. Brunelle. Preparation of catalysts by metallic complex adsorption on mineral oxides. *Pure and Applied Chemistry*, 50(9-10):1211–1229, 1978.

[45] Zhongwu Zhou, Peter J Scales, and David V Boger. Chemical and physical control of the rheology of concentrated metal oxide suspensions. *Chemical Engineering Science*, 56(9):2901 – 2920, 2001. ISSN 0009-2509. doi: http://dx.doi.org/10.1016/S0009-2509(00)00473-5. URL http://www.sciencedirect.com/science/article/pii/S0009250900004735. {NEPTIS} 8.

[46] Chunlin Miao, Shai N. Shafrir, John C. Lambropoulos, Joni Mici, and Stephen D. Jacobs. Shear stress in magnetorheological finishing for glasses. *Appl. Opt.*, 48(13): 2585–2594, May 2009. doi: 10.1364/AO.48.002585. URL http://ao.osa.org/abstract.cfm?URI=ao-48-13-2585.

[47] Paul D. Funkenbusch. *Practical Guide to Designed Experiments*. Marcel Dekker, 2005.

[48] IKA. T10 basic high-shear mixer. 2635 North Chase Pkwy SE, NC 28405-7419, Wilmington USA.

[49] T. Degen, M. Sadki, E. Bron, U. Konig, and G. Nenert. *The HighScore suite*, volume 29. PANanalytical, December 2014. Supplement S2, pp S13-S18.

[50] Aric B Shorey, Kevin M Kwong, Kerry M Johnson, and Stephen D Jacobs. Nanoindentation hardness of particles used in magnetorheological finishing (MRF). *Applied optics*, 39(28):5194–5204, 2000.

[51] John C. Vickerman and Ian S. Gilmore (Eds.). *Surface Analysis the Principal Techniques*. John Wiley & Sons Ltd, 2nd edition, 2009.

[52] *Operation Procedure for Kratos Axis Ultra XPS*. Kratos Analytical, a Shimadzu Group Company, Trafford Wharf Road, Wharfside, Manchester, M17 1GP, U.K., 2013. Used in URnano's XPS facility.

[53] Casa Software Ltd. Casaxps, 2009. URL http://www.casaxps.com/.

[54] Colloidal Dynamics. Acoustosizer iis. Colloidal Dynamics, LLC, 5150 Palm Valley Road, Suite 303 Ponte Vedra Beach, FL 32082 USA.

[55] Jun Wang and Lian Gao. Adsorption of polyethylenimine on nanosized zirconia particles in aqueous suspensions. *Journal of colloid and interface science*, 216(2): 436–439, 1999.

[56] LLC Vernier Software & Technology. Vernier ph sensor, . 13979 SW. Millikan Way, Beaverton, OR 97005-2886 USA.

[57] LLC Vernier Software & Technology. Logger lite software, . 13979 SW. Millikan Way, Beaverton, OR 97005-2886 USA.

[58] Brian McIntyre. *Electron Beam Methods in Microscopy*. University of Rochester, 275 Hutchison Rd. Rochester, NY 14620, 2014. Notes and Slides for Opt 407, SEM Practicum.

[59] Jeffrey B. Kortright and Albert C. Thompson. X-ray data booklet. Lawrence Berkley National Laboratory, University of California, Berkeley, California 94720, February 2005. Section 1.2 X-Ray Emission Energies.

[60] PL Warren and PY Shadforth. Scope and limitation for semi-quantitative XRF analysis. *JCPDS International Centre for Diffraction Data*, 783:787, 1999.

[61] BASF. Product specification, carbonyl iron powder hq, 05 2009. Product number: 30042264.

[62] H Holleck. Material selection for hard coatings. *Journal of Vacuum Science & Technology A*, 4(6):2661–2669, 1986.

[63] US Research Nanomaterials Inc. Iron oxide nanopowder / nanoparticles (Fe_3O_4, high purity, 99.5%, 15-20nm), October 2015. URL http://www.us-nano.com/inc/sdetail/435.

[64] W. S. Rasband. Imagej. U.S. National Institues of Health, Bethesda, Maryland, USA, http://http://imagej.nih.gov/ij/index.html, 1997 – 2015.

[65] *Determining the Particle Size of a Suspension or Emulsion.* Colloidal Dynamics, 5150 Palm Valley Road, Suite 303, Ponte Vedra Beach, FL 32082, 1999. http://www.colloidal-dynamics.com/.

[66] S. Salzman, L. J. Giannechini, H. J. Romanofsky, N. Golini, B. Taylor, S. D. Jacobs, and J. C. Lambropoulos. Advanced zirconia-coated carbonyl-iron particles for acidic magnetorheological finishing of chemical-vapor-deposited zns and other ir materials. In *SPIE Optifab*, pages 963307–963307. International Society for Optics and Photonics, 2015.

[67] R Di Maggio, L Fedrizzi, and S Rossi. Effect of the chemical modification of the precursor of zro2 films on the adhesion of organic coatings. *Journal of adhesion science and technology*, 15(7):793–808, 2001.

[68] ML Zheludkevich, I Miranda Salvado, and MGS Ferreira. Sol–gel coatings for corrosion protection of metals. *Journal of Materials Chemistry*, 15(48):5099–5111, 2005.

[69] J. A. Wang, M. A. Valenzuela, J Salmones, A Vázquez, A Garcıa-Ruiz, and X Bokhimi. Comparative study of nanocrystalline zirconia prepared by precipitation and sol–gel methods. *Catalysis today*, 68(1):21–30, 2001.

[70] Michael J. Rowe, Ronal L. Cappelletti, and Linda K. Clutter. Quantification of phase fraction and amorphous content. Print, 2001. NIST Center for Neutron Research Accomplishments and Opportunities.

[71] James Clin, Robert von Dreele, Ryan Windburn, Peter Stephens, and James Filliben. Quantification of phase fraction and amorphous content. PDF, 2011. The Certification of NIST Standard Reference Material 676a.

[72] Connolly James. Introduction to Quantitative X-Ray Diffraction Methods. PDF, 2012.

[73] Beena Tyagi, Kalpesh Sidhpuria, Basha Shaik, and Raksh Vir Jasra. Synthesis of nanocrystalline zirconia using sol-gel and precipitation techniques. *Industrial & engineering chemistry research*, 45(25):8643–8650, 2006.

[74] John J. Friel and Charles E. Lyman. Tutorial review: X-ray mapping in electron-beam instruments. *Microscopy and Microanalysis*, 12(01):2–25, 2006.

[75] P. Streubel, R. Hesse, L. Makhova, J. Schindelka, and R. Denecke. A practicable method for thickness estimation of ultrathin layers from xps data with unifit 2011. 2011.

[76] R. Hesse, P. Streubel, and R. Szargan. Improved accuracy of quantitative xps analysis using predetermined spectrometer transmission functions with unifit 2004. *Surface and interface analysis*, 37(7):589–607, 2005.

[77] Burkhard Beckhoff, Birgit Kanngießer, Norbert Langhoff, Reiner Wedell, and Helmut Wolff. *Handbook of practical X-ray fluorescence analysis*. Springer Science & Business Media, 2007.

[78] Buehler Inc. Probemet® conductive thermosetting molding compound, 2015. URL https://shop.buehler.com/consumables/sectioning/compression-mounting/probemet.

[79] Chunlin Miao, Rui Shen, Mimi Wang, Shai N Shafrir, Hong Yang, and Stephen D Jacobs. Rheology of aqueous magnetorheological fluid using dual oxide-coated carbonyl iron particles. *Journal of the American Ceramic Society*, 94(8):2386–2392, 2011.

[80] John H Hubbell and Stephen M Seltzer. Tables of x-ray mass attenuation coefficients and mass energy-absorption coefficients 1 kev to 20 mev for elements z= 1 to 92 and 48 additional substances of dosimetric interest. Technical report, National

Inst. of Standards and Technology-PL, Gaithersburg, MD (United States). Ionizing Radiation Div., 1995.